Investigation of Nanoscale Thermal Radiation: Theory and Experiments

by

Arvind Narayanaswamy

Submitted to the Department of Mechanical Engineering
in partial fulfillment of the requirements for the degree of

Doctor of Philosophy in Mechanical Engineering

at the

MASSACHUSETTS INSTITUTE OF TECHNOLOGY

May 2007
[June 2007]

Author .....
Department of Mechanical Engineering
May 10, 2007

Certified by .....
Gang Chen
Warren and Townley Rohsenow Professor of Mechanical Engineering
Thesis Supervisor

Accepted by .....
Lallit Anand
Chairman, Department Committee on Graduate Students

Investigation of Nanoscale Thermal Radiation: Theory and Experiments

by

Arvind Narayanaswamy

Submitted to the Department of Mechanical Engineering
on May 10, 2007, in partial fulfillment of the
requirements for the degree of
Doctor of Philosophy in Mechanical Engineering

Abstract

The ability to control the radiative properties of objects is of prime importance in diverse areas like solar and thermophotovoltaic energy conversion, narrowband thermal emitters, and camouflage in military applications. Thermal radiation at the nanometer scale is significantly different from classical or macroscopic radiative energy transport - wave effects, such as interference and diffraction, and near-field effects play a significant role. By modeling thermal radiation as governed by Maxwell's equations and relating the source of thermal radiation to temperature induced fluctuations of electric currents, it becomes possible to capture the nanaoscale effects that differrentiate it from classical blackbody radiation.

This work is focused on two aspects of nanoscale thermal radiation - the ability to tailor the emissive properties using 1D photonic crystals and the enhancement of radiative heat transfer due to electromagnetic surface waves. Theoretical investigation of thermal radiation in 1D photonic crystals led to the proposal of new type of selective emitters using 1D metallo-dielectric photonic crystals that rival the more intricate 2D and 3D counterparts. In addition to far-field spectral control, near-field enhancement due to surface phonon polaritons is shown to be useful for enhancing the power density of thermophotovoltaic energy conversion.

The difficulties of experimental investigation of near-field phenomena between macroscopic parallel surfaces led to the theoretical investigation of near-field effects betwene two spheres and experimental investigation between a sphere and a flat plate. A new technique for measuring the radiative transfer between a sphere and a substrate using a bi-material atomic force microscope cantilever as the sensor was developed. By measuring "heat transfer-distance" curves, just as one measures "force-distance" curves in atomic force microscopy, the experimental results are shown to be in agreement with a theory.

Thesis Supervisor: Gang Chen
Title: Warren and Townley Rohsenow Professor of Mechanical Engineering

Acknowledgments

Since we had already decided on an academic career, I used to tell my friend and colleague, Chris Dames, that we would be ready for that only when we have paid our dues by making a reasonable scientific contribution. I never imagined that it would take me almost six years to do that!

When I started off my doctoral work with Prof. Gang Chen in UCLA, I did not for a moment envisage what lay ahead of me. Since my undergraduate academic record was everything but good, I did not entertain any dreams of studying at MIT even though Prof. Chen mentioned a possible move from UCLA to MIT. Without the confidence Prof. Chen showed in me, I would never have been admitted to MIT. Graduate research can sometimes be a bitter experience and it is to Prof. Chen's credit that I never for once lapsed into that thought. He encouraged me to get out of my comfort zone of theoretical and mathematical research and become proficient in experimental techniques too.

I have known Prof. Lienhard and Prof. Mikic as my thesis committee members as well a teachers I respect immensely. Both of them have been extraordinary educators and I have benefited greatly as a teaching assistant to them. My renewed interest in macroscale heat transfer and fluid mechanics would not have been possible without my interactions with Prof. Lienhard, Prof. Mikic, and Prof. C. C. Mei. My thesis advisor at University of Delaware, Prof. John Lambros, and my teachers at IIT-Madras – Prof. Vijay R. Raghavan, Prof. M. S. Sivakumar, Prof. T. Sundararajan, and Prof. A. Venkatesh – have all played important roles my academic development.

While they may not have realized it, Satyan Subbiah and Chris Dames have had huge influence on me as a person as well as a scientist. They are two individuals who have been extraordinarily helpful to anyone who seeks their help. I hope I can be a little like them. My labmates at the Chen group have been been a great resource. I will treasure my interactions with Diana Borca-Tasciuc, Xiaoyuan Chen, Zony Chen, Jim Cybulski, Tom Harris, Lu Hu, Hohyun Lee, Koji Miyazaki, Gregg Radtke, David Song, Aaron Schmidt, Ashish Shah, Erik Skow, and Ronggui Yang.

None of this would have been possible without the help of my family and friends. The love and encouragement of Amma and Appa, Pati and Thatha, Pattu perima, Saras perima, Bhuvna chithi, Aswini, Nagini, and my parents-in-law have made everything easier than it seems. To Kripa – thanks for everything.

Contents

List of Figures

List of Tables

Chapter 1

Introduction

Thermal radiation is composed of electromagnetic waves of different wavelengths. Every student who has studied thermal radiation knows this. This was not the case just a century and a half ago when Maxwell and his contemporaries were trying to understand the fundamental nature of thermal radiation. The realization that light is in fact an electromagnetic phenomena and is the result of the path-breaking works of, in part, Ampere[1], Faraday, Maxwell [2], Kirchoff [3], and Weber [4, 5]. The similarities between the behavior of light and heat radiation (reflection by mirrors, refraction by lenses, and most importantly interference phenomena) and Maxwell's theory of electricity and magnetism led to the conclusion that thermal radiation was indeed an electromagnetic phenomena. Subsequently, Stefan proposed the T^4 dependence of the intensity of radiation based on the experimental data of Dulong and Petit, Tyndall, and others [6]. Boltzmann derived theoretically, using thermodynamics and the concept of Maxwell radiation pressure, the T^4 relation between the energy density and intensity of radiation from a black body at temperature T. Wien's work resulted in the so-called "displacement law" that showed that if the spectral energy density is known at a given temperature, it can then be deduced for all temperatures. All these works (and others I surely have omitted) laid the foundation for Planck to propose his famous hypothesis of the quanta. This paragraph is in no way meant to be a review of the history of the science of thermal radiation. However, I do wish to instill in the reader a sense of awe at the immensity of work that is behind the idea that

thermal radiation is composed of electromagnetic waves of different wavelengths.

1.1 Thermal radiation and classical electromagnetism

Though the study of thermal radiation was intimately linked to that of electromagnetism, subsequent development of the classical theory of radiative transfer relied more on Kirchoff's law, Stefan-Boltzmann law, and Planck's theory of the spectrum of black body radiation. Crucially, the propagation of thermal radiation was treated by the principles of geometric optics or ray tracing. Thermal radiation from an object is treated as originating at the surface with the emissivity of the object taking into account that it is not a black body. While such an approach is sufficient to understand thermal radiation from objects much larger than the wavelength of the thermal radiation, it does not take into account diffraction or intereference phenomena which are important when the emitters have dimensions comparable to the wavelength. That this is the case was recognized by Planck [7]. To take these effects into account the wave nature of thermal radiation has to be taken into account.

To describe thermal radiation using Maxwell's equations a relation between the temperature of an emitter and the electric current density that is the cause of thermal radiation is necessary. This was achieved with the development of the fluctuation-dissipation (FD) theorem. In 1928, Johnson discovered the noise due to thermal agitation in electrical conductors and Nyquist theoretically showed the relation between the noise and temperature. In doing so, Nyquist developed the classical form of the FD theorem. A quantum mechanical derivation of the FD theorem relating the generalized resistance and the fluctuations of the generalized forces in linear dissipative systems was provided by Callen and Welton in 1951 [8]. In 1953, Rytov published his seminal work on the theory of electrical fluctuations and thermal radiation, where he treated thermal radiation as a volumetric phenomena for the first time. [9, This is the English translation. The Russian version was published in 1953] Rytov's formalism clearly made it possible to include the effects of diffraction and interference.

The concept of dyadic Green's function (DGF) was introduced into literature by Levine and Schwinger in 1951. [10] Since then the DGF has been used very widely by the electromagnetic community to solve various types of scattering problems. [11–15]. The DGF is similar to the idea of Green's functions that appear in heat conduction, electrostatics, or scalar wave propagation. The key difference is that the DGF describes the vector field (electric and magnetic fields) produced by a vector sources (electric current density). The DGF is then a tensor that transforms the current density vector into the electric or magnetic field vectors. Though it is not necessary to determine the DGF to find the solution to a given electromagnetic scattering problem, it provides for very elegant formalism and is especially useful in the analysis of radiative transfer. To determine the DGF for any given configuration of scatterers is not always easy and most often numerical schemes run into computational difficulties. For multilayered structures, though, the DGF is well known and used widely in recent literature in near-field radiative transfer.

Work on near-field thermal radiation in the US began in the 1960s in Prof. Chang-lin Tien's group. The enhancement of thermal radiation transfer between closely spaced bodies was investigated theoretically by Cravalho et al. [16], Domoto and Tien [17], and Boehm and Tien [18] and experimentally by Domoto et al. [19]. Polder and Van Hove analyzed radiative energy transfer between closely spaced bodies for the first time based on the FD theorem [20]. Around the same time, Hargreaves measured the enhancement in radiative flux between metallic films of chromium (approximate thickness 100 nm) deposited on optical flats (approximate area 4.8 cm^2). [21]. Xu et al. [22] measured radiative transfer between a deformed indium surface and a gold surface of area 0.0256 mm^2. With the emergence of scanning probe microscopies, Hirsch et al. [23] and Kittel et al. [24] measured proximity effects in near-field radiative transfer between a scanning tunneling microscope tip and a substrate. DiMatteo et al. [25] observed an enhanced coupling between a heated surface and a photovoltaic cell due to proximity effects. Around this time fundamentally new insight into the nature of electromagnetic fields of thermal origin was gained with the works from Greffet and collaborators [26–32]. The role played by electromagnetic surface waves and the

effect they have on near-field thermal fields and radiative transfer is the main focus of most of these articles. Almost all the theoretical works in near-field enhancement can be divided into one of two groups - (1) analyzing enhancement between parallel surfaces (2) between two dipoles or between a dipole and a flat surface. The main reason for this is the difficulty of determining the DGF in other configurations. One work that attempted this but did not complete the analysis owing to numerical difficulties is the work of Volokitin and Persson [33]. In this work, the authors tried to analyze radiative transfer between two nanostructures. In particular they tried to investigate the enhancement in radiative transfer when two spheres are extremely closely spaced. They did not complete the analysis due to numerical difficulties. In comparison to the theoretical analysis of near-field enhancement, experimental investigation is limited to only a few cases [19, 21–24].

1.2 Purpose and outline of thesis

The aim of my work is to futher the understanding of thermal radiation when nanoscale effects become important. One area of energy conversion that can greatly benefit from this understanding is thermophotovoltaic (TPV) energy conversion [25, 34–37]. The study of near-field effects is also important from a fundamental point of view. The study of near-field forces between objects, like Van der Waals or Casimir forces, has contributions from the zero point energy as well as a temperature dependent part, which is much smaller that the zero point contributions at room temperatures. The measurement of the temperature dependent part of the forces can be great facilitated by studying the near-field heat transfer, thereby gaining information about the forces, since both radiative transfer and the temperature dependent forces have the same origin in the fluctuation of charges due to the finite temperature [38]. My intention was also to investigate near-field effects in configurations other than that between two flat surfaces or between a flat surface and a nanoparticle. In particular, I wish to investigate near-field effects in configurations that can be tested experimentally more easily than between two parallel surfaces. To do so, I have investigated theoretically

the near-field radiative transfer between two spheres and experimentally the radiative transfer between a sphere and a substrate.

The outline of my thesis is as follows: Chapter 2 deals with the electrodynamic origin of thermal radiation. The FD theorem, used to relate the current density to the local temperature, and the DGF to analyze the emission from such sources is described. Using this, the expressions for the Poynting vector and radiative transfer between two objects is derived. In Chapter 3 the electromagnetic formulation is applied to the 1D multilayer structures. The near-field interaction between a half-space of polar material and a thin film of photovoltaic (PV) material is investigated to illustrate the effectiveness of near-field enhancement for TPV applications. The nature of thermal radiation inside a 1D photonic crystal (PC) is studied by determining the DGF of a periodic infinite structure using a technique known as the phased array technique. The results of this analysis are used to propose a novel metallo-dielectric structure with selective emission properties. Chapter 4 is an in-depth analysis of the two-sphere problem. Since this problem has not been analyzed using the techniques mentioned above, I present a detailed account of the method. Based on the numerical results, I propose a new convergence criterion for the number of vector eigenfunctions required. Chapter 5 deals with the experimental investigation of the near-field radiative transfer between a sphere and a flat surface. The numerical results from Chapter 4 are used to identify the right type of sensor and experimental apparatus required for such an investigation. Following a discussion of the apparatus and its similarities and differences with an atomic force microscope (AFM), I show how we can obtain "heat transfer - distance " curves and present results for conductive transfer and radiative transfer between a sphere and a flat substrate. I details the pros and cons of the present experimental setup and discuss improvements.

We know that the same electromagnetic formulation that describes thermal radiative transfer also describes forces like Van der Waals and Casimir forces. However, both theoretical and experimental work in investigation of forces span a wider range of configurations (sphere-plate, sphere-sphere, cylinder-plate, cylinder-cylinder) than that for near-field heat transfer (flat plate–flat plate or dipole–flat plate). I hope the

latter part of my work involving radiative transfer between a spherical surfaces and the experimental technique of the same will help in bridging the gap between the two fields which are two sides of the same coin.

Chapter 2

Fundamentals

2.1 Introduction and outline

In this chapter the basic theoretical framework necessary for predicting nanoscale thermal effects is described. Section 2.2 deals with the relationship between thermal radiation and Maxwell's equations. Starting from the microscopic Maxwell's equations, the macroscopic Maxwell's equations which are useful for describing thermal radiation from emitters are "derived". In that process, the electrical and magnetic susceptibilities, and the dielectric function are introduced. In Sec. 2.3, the stochastic nature of the current sources is treated using the fluctuation-dissipation (FD) theorem [8, 39–42]. Using the FD theorem, a relation between the fluctuations of the current density and the local temperature is established. The vector Helmholtz equations for the electric and magnetic fields are derived. To solve this equation, the dyadic Green's function (DGF) is introduced. The Poynting vector, and hence the radiative flux, is expressed in terms of the the components of the DGF.

2.2 Maxwell's equations

Any kind of electromagnetic field oscillating at a frequency ω, be it thermal radiation or radio waves, is governed by Maxwell's equations:

$$\nabla \times \boldsymbol{e}(\boldsymbol{r},\omega) - i\omega \boldsymbol{b}(\boldsymbol{r},\omega) = 0 \tag{2.1a}$$

$$\nabla \times \boldsymbol{b}(\boldsymbol{r},\omega) + i\omega\mu_o\epsilon_o \boldsymbol{e}(\boldsymbol{r},\omega) = \mu_o \boldsymbol{j}(\boldsymbol{r},\omega) \tag{2.1b}$$

$$\nabla \cdot \boldsymbol{e}(\boldsymbol{r},\omega) = \frac{\rho}{\epsilon_o} \tag{2.1c}$$

$$\nabla \cdot \boldsymbol{b}(\boldsymbol{r},\omega) = 0 \tag{2.1d}$$

Equation 2.1 is sometimes referred to as the microscopic Maxwell's equations and is valid everywhere. The quantities $\boldsymbol{j}(\boldsymbol{r},\omega)$ and ρ represent the total current and total charge. It is important to note that the field quantities in Eq. 2.1 are in the frequency domain. Hence, even though I refer to them as electric fields, the units are not simply Vm^{-1}. The units are in fact $\mathrm{Vm}^{-1}(\mathrm{rad\ s}^{-1})^{-1}$. Similarly, the units of the quatities must be modified too. While it is easily applicable to the case of wave propagation in vacuum, it becomes unwieldy for wave propagation in other media. One way to overcome this difficulty is to modify the equation to represent a relation between the field quantities and the free charge and free current. $\boldsymbol{j}(\boldsymbol{r},\omega)$ can be split into a free current, a polarization current, and a bound current due to magnetization. ρ can be split into a free charge and a polarization charge. [43]

$$\begin{aligned} \boldsymbol{j}(\boldsymbol{r},\omega) &= \boldsymbol{J}_f(\boldsymbol{r},\omega) + \boldsymbol{J}_p(\boldsymbol{r},\omega) + \boldsymbol{J}_m(\boldsymbol{r},\omega) \\ &= \boldsymbol{J}_f(\boldsymbol{r},\omega) - i\omega \boldsymbol{P}(\boldsymbol{r},\omega) + \nabla \times \boldsymbol{M}(\boldsymbol{r}) \end{aligned} \tag{2.2a}$$

$$\begin{aligned} \rho &= \rho_f + \rho_p \\ &= \rho_f - \nabla \cdot \boldsymbol{P}(\boldsymbol{r},\omega) \end{aligned} \tag{2.2b}$$

where $\boldsymbol{J}_f$ is the free current, $\boldsymbol{J}_p$ is the current due to polarization, and $\boldsymbol{J}_m$ is that due to magnetization. $\boldsymbol{P}$ is the polarization and $\boldsymbol{M}$ is the magnetization. Using Eq. 2.2,

Eq. 2.1 can be modified to

$$\nabla \times \boldsymbol{E}(\boldsymbol{r},\omega) - i\omega \boldsymbol{H}(\boldsymbol{r},\omega) = 0 \tag{2.3a}$$

$$\nabla \times \boldsymbol{H}(\boldsymbol{r},\omega) + i\omega\epsilon(\boldsymbol{r})\boldsymbol{E}(\boldsymbol{r},\omega) = \boldsymbol{J}_f(\boldsymbol{r},\omega) \tag{2.3b}$$

$$\nabla \cdot \boldsymbol{D}(\boldsymbol{r},\omega) = \rho_f \tag{2.3c}$$

$$\nabla \cdot \boldsymbol{H}(\boldsymbol{r},\omega) = 0 \tag{2.3d}$$

where $\boldsymbol{D}(\boldsymbol{r},\omega) = \epsilon_o \boldsymbol{E}(\boldsymbol{r},\omega) + \boldsymbol{P}(\boldsymbol{r},\omega)$, $\boldsymbol{H}(\boldsymbol{r},\omega) = \boldsymbol{B}(\boldsymbol{r},\omega)/\mu_o - \boldsymbol{M}(\boldsymbol{r},\omega)$. $\boldsymbol{D}$ is the electric displacement vector, and $\boldsymbol{H}$ is the magnetic field vector. Vectors $\boldsymbol{E}(\boldsymbol{r},\omega)$ and $\boldsymbol{H}(\boldsymbol{r},\omega)$ are spatially averaged values of $\boldsymbol{e}(\boldsymbol{r},\omega)$ and $\boldsymbol{h}(\boldsymbol{r},\omega)$ [43]. From this point onwards, the subscript f will be dropped since all the currents will refer only to the free currents.

2.2.1 Electric susceptibility and dielectric function

For the values of the magnitudes of electric and magnetic field vector encountered in thermal radiation (including near-field effects), non-linear effects are negligible and hence the polarization and magnetization are linearly related to the electric and magnetic field vector. Cross-effects of electric fields resulting in a magnetization (or magnetic fields resulting in a polarization) are not considered in this work. Since $\boldsymbol{E}$ ($\boldsymbol{H}$) and $\boldsymbol{P}$ ($\boldsymbol{M}$) are vectors, the most general linear relation between them is given by:

$$\boldsymbol{P}(\boldsymbol{r},\omega) = \epsilon_o \overline{\overline{\chi}}_e(\boldsymbol{r},\omega) \cdot \boldsymbol{E}(\boldsymbol{r},\omega) \tag{2.4a}$$

$$\boldsymbol{M}(\boldsymbol{r},\omega) = \overline{\overline{\chi}}_m(\boldsymbol{r},\omega) \cdot \boldsymbol{H}(\boldsymbol{r},\omega) \tag{2.4b}$$

where $\overline{\overline{\chi}}_e$ and $\overline{\overline{\chi}}_m$, the electric and magnetic susceptibilities, are tensors. In general, the susceptibilities are complex frequency dependent quantities. In this work, all materials are assumed to be isotropic and hence $\overline{\overline{\chi}}_e$ and $\overline{\overline{\chi}}_m$ reduce to scalar quantities.

Equation 2.4 reduces to

$$\boldsymbol{P}(\boldsymbol{r},\omega) = \epsilon_o \chi_e(\boldsymbol{r},\omega)\boldsymbol{E}(\boldsymbol{r},\omega) \tag{2.5a}$$

$$\boldsymbol{M}(\boldsymbol{r},\omega) = \chi_m(\boldsymbol{r},\omega)\boldsymbol{H}(\boldsymbol{r},\omega) \tag{2.5b}$$

where $\chi_e(\boldsymbol{r},\omega)$ and $\chi_m(\boldsymbol{r},\omega)$ are scalar functions of frequency. An important point to make about Eq. 2.4 and Eq. 2.5 is the "local" nature of the formulation. The polarization and magnetization at $\boldsymbol{r}$ depend only on the electric and magnetic field respectively at $\boldsymbol{r}$. Most materials, in the mid-IR to UV frequencies, are non-magnetic and hence $\chi_m \approx 0$. In this work, the materials are assumed to be non-magnetic. The dielectric function $\epsilon(\boldsymbol{r},\omega)$ is related to $\chi_e(\boldsymbol{r},\omega)$ as:

$$\epsilon(\boldsymbol{r},\omega) = 1 + \chi_e(\boldsymbol{r},\omega) \tag{2.6}$$

The real and imaginary part of the susceptibilities (and hence the dielectric function) are related to each other through the Kramers-Kronig relations and are not independent of each other. [43–45]. The dielectric function of polar materials, which exhibit enormous near-field enhancement, is of the form:

$$\epsilon(\omega) = \epsilon_\infty\left(\frac{\omega^2 - \omega_{LO}^2 + i\gamma\omega}{\omega^2 - \omega_{TO}^2 + i\gamma\omega}\right) \tag{2.7}$$

where ω_{LO} and ω_{TO} are the longitudinal and transverse optical phonon frequencies, γ is a damping factor, and ϵ_∞ is the dielectric function at high frequencies or short wavelength. The real part of the dielectric function for SiC, a polar material, is shown in Fig. 2-1. Between the two frequencies, ω_{LO} and ω_{TO}, the real part of the dielectric function turns out to be negative. For metals, the dielectric function is obtained by letting $\omega_{TO} \to 0$. Below a frequency known as the plasmon frequency, the real part of the dielectric function of metals is negative. In those parts of the spectrum where the dielectric function of a material is negative, electromagnetic modes known as surface waves can exist at the interface between the material and vacuum. These surface waves can lead to resonant heat transfer around the region where $\epsilon(\omega) \approx -1$. The

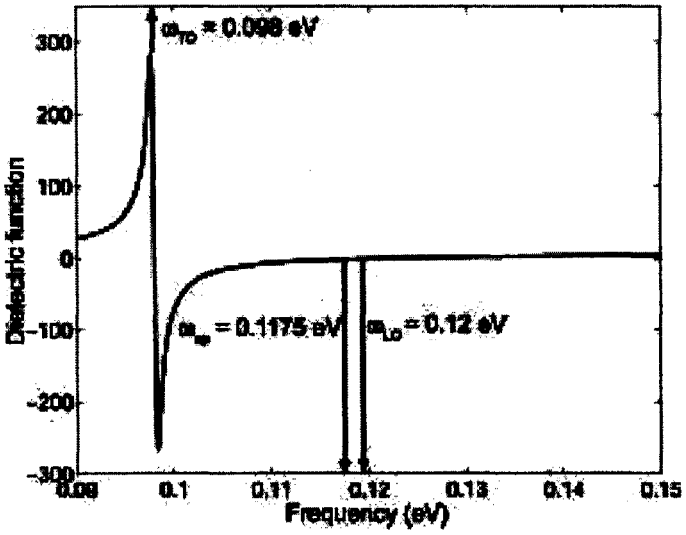

Figure 2-1: Real part of dielectric function of SiC

plasmon frequency of metals is generally in the visible to UV part of the spectrum. On the other hand, the ω_{LO} and ω_{TO} frequencies for polar materials lie in the mid-IR to far-IR range. This has important consequences for radiative heat transfer. More on this topic will be discussed in Chapter 3.

2.3 Electromagnetic formulation of thermal radiative transfer

In this work, all the materials are assumed to be non-magnetic and defined by a complex, frequency dependent dielectric function, $\varepsilon(\omega)$. To compute the radiative transfer we follow the method pioneered by Rytov [9, 46] in which the source for radiation is the thermal fluctuations of charges. The first step in this formulation is to obtain the electric field in the regions of interest given the location of a source. To do this we should know the DGF for the vector Helmholtz equation which governs the electric and magnetic fields. The DGF is very similar to the scalar Green's function used commonly in the solution of boundary value problems in electrostatics and heat conduction [43, 47, 48]. The main difference is that it gives the vectorial response (electric field vector) of a vectorial source (electric current density) and hence itself is

a dyad or a tensor of second rank. All the DGFs used in this work can be expressed as a sum (generally infinite number of terms) of terms of the form $\boldsymbol{ab}$, where $\boldsymbol{a}$ and $\boldsymbol{b}$ are vectors. Further details regarding the properties of dyads are given in [11, 49]. Once this DGF is known, the one remaining step to compute radiative transfer between objects is to relate the current density vector to temperature. This is achieved by using the fluctuation-dissipation theorem.

2.3.1 Dyadic Green's function

The Fourier component of the fluctuating electric field, $\boldsymbol{E}(\boldsymbol{r}_1, \omega)$, and magnetic field, $\boldsymbol{H}(\boldsymbol{r}_1, \omega)$, at any point, $\boldsymbol{r}_1$, outside a volume containing the sources is given by [15, 45]:

$$\boldsymbol{E}(\boldsymbol{r}_1, \omega) = i\omega\mu_o \int_V d^3r \overline{\overline{\boldsymbol{G}}}_e(\boldsymbol{r}_1, \boldsymbol{r}, \omega) \cdot \boldsymbol{J}(\boldsymbol{r}, \omega) \tag{2.8}$$

$$\boldsymbol{H}(\boldsymbol{r}_1, \omega) = \int_V d^3r \overline{\overline{\boldsymbol{G}}}_h(\boldsymbol{r}_1, \boldsymbol{r}, \omega) \cdot \boldsymbol{J}(\boldsymbol{r}, \omega), \tag{2.9}$$

where $\overline{\overline{\boldsymbol{G}}}_e(\boldsymbol{r}_1, \boldsymbol{r}, \omega)$ and $\overline{\overline{\boldsymbol{G}}}_h(\boldsymbol{r}_1, \boldsymbol{r}, \omega)$, the dyadic Green's functions due to a point source at $\boldsymbol{r}$, are related by $\overline{\overline{\boldsymbol{G}}}_h(\boldsymbol{r}_1, \boldsymbol{r}, \omega) = \boldsymbol{\nabla_1} \times \overline{\overline{\boldsymbol{G}}}_e(\boldsymbol{r}_1, \boldsymbol{r}, \omega)$; $\boldsymbol{J}(\boldsymbol{r}, \omega)$ is the Fourier component of the current due to thermal fluctuations (The relation between $\boldsymbol{J}(\boldsymbol{r}, \omega)$ and the temperature is discussed in Sec. 2.3.2); and μ_o is the permeability of vacuum. The integration is performed over the entire volume V containing the source. The dyadic Green's functions themselves obey the following equations [15, 45]:

$$\boldsymbol{\nabla} \times \boldsymbol{\nabla} \times \overline{\overline{\boldsymbol{G}}}_e(\boldsymbol{r}, \boldsymbol{r}') - \left(\frac{\omega}{c}\right)^2 \varepsilon(\boldsymbol{r}) \overline{\overline{\boldsymbol{G}}}_e(\boldsymbol{r}, \boldsymbol{r}') = \overline{\overline{\boldsymbol{I}}} \delta(\boldsymbol{r} - \boldsymbol{r}') \tag{2.10}$$

where $\overline{\overline{\boldsymbol{I}}}$ is the identity dyad and $\delta(\boldsymbol{r} - \boldsymbol{r}')$ is the Dirac-delta function. At the boundary between two dielectric materials, the DGF satisfies the following boundary conditions to ensure continuity of tangential electric and magnetic fields:

$$\hat{\boldsymbol{n}} \times \overline{\overline{\boldsymbol{G}}}_e(\boldsymbol{r}_1, \boldsymbol{r}') = \hat{\boldsymbol{n}} \times \overline{\overline{\boldsymbol{G}}}_e(\boldsymbol{r}_2, \boldsymbol{r}') \tag{2.11}$$

$$\hat{\boldsymbol{n}} \times \boldsymbol{\nabla} \times \overline{\overline{\boldsymbol{G}}}_e(\boldsymbol{r}_1, \boldsymbol{r}') = \hat{\boldsymbol{n}} \times \boldsymbol{\nabla} \times \overline{\overline{\boldsymbol{G}}}_e(\boldsymbol{r}_2, \boldsymbol{r}') \tag{2.12}$$

where $\boldsymbol{r}_1$ and $\boldsymbol{r}_2$ are points on either side of the boundary and $\hat{\boldsymbol{n}}$ is a unit normal to the boundary surface at $\boldsymbol{r}_1$ (or $\boldsymbol{r}_2$). We see from Eq. 2.10 that the units of the DGF is L^{-1} or the inverse of length. Though we have obtained expression for the fields in terms of the DGF, determining radiative transfer requires know of the spectral Poynting vector, which is given by $\boldsymbol{S} = \boldsymbol{E} \times \boldsymbol{H}^*$. In order to compute the spectral Poynting vector at $\boldsymbol{r}_1$, we must compute terms of the form $\langle E_{i\omega} H^*_{j\omega} \rangle$, where the $*$ denotes the complex conjugate, the brackets denote a statistical ensemble average, and i and j refer to the three Cartesian components ($i \neq j$). From Eq. 2.8, we can write an expression for $\langle E_{i\omega} H^*_{j\omega} \rangle$ as:

$$\langle E_i(\boldsymbol{r}_1,\omega) H^*_j(\boldsymbol{r}_1,\omega) \rangle = i\omega\mu_o \int_V d^3r \int_V d^3r' \{ G_{e_{il}}(\boldsymbol{r}_1,\boldsymbol{r},\omega) G^*_{h_{jm}}(\boldsymbol{r}_1,\boldsymbol{r}',\omega) \langle J_l(\boldsymbol{r},\omega) J^*_m(\boldsymbol{r}',\omega) \rangle \} \tag{2.13}$$

2.3.2 Fluctuation-dissipation theorem

The stochastic nature of the current density vector results in the average electric and magnetic fields becoming zero. However, as seen from Eq. 2.13, the quantity of interest is not the average value of the current density vector but the average value of the products of current density vector components. The fluctuation-dissipation theorem states that the cross spectral density of different components of a fluctuating current source in equilibrium at a temperature T is given by [8, 42, 50]:

$$\langle J_l(\boldsymbol{r},\omega) J^*_m(\boldsymbol{r}',\omega) \rangle = \frac{\epsilon_o \epsilon''(\omega) \omega \Theta(\omega,T)}{\pi} \delta_{lm} \delta(\boldsymbol{r}-\boldsymbol{r}'), \tag{2.14}$$

where $\epsilon''(\omega)$ is the imaginary part of the dielectric function of the source, ϵ_o is the permittivity of vacuum, and

$$\Theta(\omega,T) = \hbar\omega \Big[\frac{1}{2} + \frac{1}{(exp(\hbar\omega/k_B T) - 1)} \Big], \tag{2.15}$$

where $2\pi\hbar$ is Planck's constant and k_B is Boltzmann's constant. The $\hbar\omega/2$ part is the zero point energy which contributes to van der Waals and Casimir forces between

objects but not to radiative transfer. Equation 2.14 relates the cross-correlation of current density components to the optical properties of the material and temperature. Importantly, it relates the cross-correlation to only the imaginary or absorptive part of the dielectric function. The δ_{lm} that appears in Eq. 2.14 is because of the fact that we have assumed all materials to be isotropic and hence no coupling between fluctuations in orthogonal directions. The Dirac delta function, $\delta(\boldsymbol{r}-\boldsymbol{r}')$ that appears in Eq. 2.14 is an approximation, known as a local approximation, and is valid at all but the smallest of length scales comparable to the mean free path of electrons in metals or atomic spacing in case of dielectrics. The presence of $\delta(\boldsymbol{r}-\boldsymbol{r}')$ leads to a singularity in the radiative heat transfer between objects as the gap between them decreases to zero. This unphysical result is because of the assumption that the dielectric function depends only on the temporal frequency (ω). Irrespective of the spatial frequency or wavevector of the wave, the dielectric function remains the same. This results in overestimating the contribution of the waves with high spatial frequency. In fact, the dielectric function can be generalized to be a function of temporal frequency as well as spatial frequency or wavevector [39, 40, 51, 52]. By doing so the Dirac delta function in Eq. 2.14 is replaced by a "smoother" function which eliminates the singularity in the near-field radiative transfer [9, 40]. The finite correlation that exists between fluctuations at $\boldsymbol{r}$ and $\boldsymbol{r}'$ is known as a non-local effect. In this work, we shall use only the local formulation and assume the validity of Eq. 2.14

2.3.3 Thermal radiative transfer

Using Eq. 2.13 and Eq. 2.14, we have

$$\langle E_i(\boldsymbol{r}_1,\omega)H_j^*(\boldsymbol{r}_1,\omega)\rangle = \frac{i\epsilon_o\epsilon''(\omega)\mu_o\omega^2\Theta(\omega,T)}{\pi}\int_V d^3r\{(\boldsymbol{G}_e(\boldsymbol{r}_1,\boldsymbol{r},\omega).\boldsymbol{G}_h^{T*}(\boldsymbol{r}_1,\boldsymbol{r},\omega))_{ij}\} \tag{2.16}$$

where the superscript T stands for the transpose of the dyad. Once the Green's function for the given configuration is determined, the above integral is computed numerically. To determine spectral radiative transfer itself between two objects at T_1

and T_2, we use the following equation:

$$\Re\langle E_i(\boldsymbol{r}_1,\omega)H_j^*(\boldsymbol{r}_1,\omega)\rangle = \frac{\epsilon_o\epsilon''(\omega)\mu_o\omega^2}{\pi}[\Theta(\omega,T_1)-\Theta(\omega,T_2)]\Im\Big[\int_V d^3r\{(\boldsymbol{G}_e(\boldsymbol{r}_1,\boldsymbol{r},\omega).\boldsymbol{G}_h^{T*}(\boldsymbol{r}_1,\boldsymbol{r},\omega))_{ij}\}\Big] \tag{2.17}$$

where $\Re$ and $\Im$ stand for the real and imaginary parts. The net result of using the FD theorem and the DGF formalism is to reduce a problem of thermal radiative transfer to a problem of determining the DGF for a given configuration of objects. Chapter 3 involves determining the DGF for planar multilayer media and Chapter 4 deals with the DGF in a two-sphere configuration.

Chapter 3

Thermal radiative transfer in planar configurations

3.1 Introduction and outline

In this chapter the radiative transfer in 1D configurations is discussed using the formalism developed in Chap. 2. The DGF for multilayer configurations is a topic of numerous publications, some of which are cited here [14, 15, 37, 44, 45, 53]. Section 3.4 deals with the enhancement in thermal radiative transfer with decrease in gap. In particular, the problem of near-field transfer between a polar material and a photovoltaic material is investigated to establish the relevance of nanoscale thermal radiation to thermophotovoltaic (TPV) energy conversion. Spectral control of far-field radiation is dealt with in Sec. 3.5. The problem of the nature of thermal radiation inside a 1D photonic crystal (PC) is investigated using the phased array technique (PAT). The results of this problem provide the basis for proposing a novel type of 1D metallodielectric PC thermal emitter that could be potential interest as a selective emitter for TPV conversion.

3.2 Dyadic Green's function for multilayered media

Dyadic Green's function have been used extensively for the solution of wave propagation problems in layered media. A schematic of the stratified media that is representative of most of the structures to be investigated in this chapter is shown in Fig. 3-1. The layers are homogeneous in the x-y plane. The dielectric properties of the materials change only along the z-axis, as shown in Fig. 3-1. Because of the symmetry in the x-y plane, the specific directions of the x and y axes are of no consequence. Starting from the DGF for an infinite, isotropic, homogeneous medium it is possible to find an expression for the DGF of the multilayered medium. Unknown coefficients in the expressions for the DGF can be solved for by using the boundary conditions in Eq. 2.11 and Eq. 2.12. For a homogeneous, isotropic, infinite media, the dyadic Green's function is given by [15, 45]:

$$\overline{\overline{\boldsymbol{G}}}_e(\boldsymbol{r},\boldsymbol{r}') = \frac{i}{8\pi^2}\times \int_{-\infty}^{-\infty}\int_{-\infty}^{-\infty} \frac{dk_x dk_y}{k_{zs}} \begin{cases} \left(\hat{\boldsymbol{e}}(+k_{zs})\,\hat{\boldsymbol{e}}(+k_{zs}) + \hat{\boldsymbol{h}}(+k_{zs})\,\hat{\boldsymbol{h}}(+k_{zs})\right) e^{i(\boldsymbol{k}_s\cdot\boldsymbol{r}-\boldsymbol{k}_s\boldsymbol{r}')} & z > z' \\ \left(\hat{\boldsymbol{e}}(-k_{zs})\,\hat{\boldsymbol{e}}(-k_{zs}) + \hat{\boldsymbol{h}}(-k_{zs})\,\hat{\boldsymbol{h}}(-k_{zs})\right) e^{i(\boldsymbol{K}_s\cdot\boldsymbol{r}-\boldsymbol{K}_s\boldsymbol{r}')} & z < z' \end{cases} \tag{3.1}$$

where the unit vectors $\hat{\boldsymbol{e}}(\pm k_z) = (k_y\hat{\boldsymbol{x}} - k_x\hat{\boldsymbol{y}})/k_\rho$ and $\hat{\boldsymbol{h}}(\pm k_z) = \mp(k_z/k)(k_x\hat{\boldsymbol{x}} + k_y\hat{\boldsymbol{y}})/k_\rho + (k_\rho/k)\hat{\boldsymbol{z}}$. $k_z = \sqrt{k^2 - k_\rho^2}$, $k_\rho^2 = k_x^2 + k_y^2$. $\boldsymbol{k} = k_x\hat{\boldsymbol{x}} + k_y\hat{\boldsymbol{y}} + k_z\hat{\boldsymbol{z}}$ and $\boldsymbol{K} = k_x\hat{\boldsymbol{x}} + k_y\hat{\boldsymbol{y}} - k_z\hat{\boldsymbol{z}}$. k_x, k_y, and k_z are wavevectors in the x, y, and z directions respectively. The subscript s is used to indicate that the layer in consideration contains the source. The sign of the square root for k_z is very important. It should be chosen such that $\Im(k_z) > 0$ to ensure that fields decay as $z \to \infty$ in any unbounded region. By the same logic, $\Im(K_z) < 0$ to ensure that fields decay in any unbounded region where $z \to -\infty$. The wavevectors k_x and k_y are referred to as in-plane wavevectors and k_z as out-of-plane wavevector. Equation 3.1 is a representation of the DGF in terms of

plane waves propagating with wavevectors $(k_x, k_y, \pm k_z)$. It is important to note that these plane waves are vector plane waves. The electromagnetic fields in layered media can be divided into two types of polarization transverse electric (TE) and transverse magnetic (TM). For TE(TM) waves, the electric(magnetic) field lies entirely in the plane tangential to the interfaces. Expansion of a DGF in terms of vector waves appropriate to the configuration of objects will be used in Chapter 4 too. Except for the fact that we are dealing with vectorial quantities, this is no different from expansion of a function in terms of orthogonal functions. The integration over k_x and k_y extends from $-\infty$ to $+\infty$ because of the continuous and infinite extent of the multilayer system in the x-y plane. As mentioned in Section 2.3, the DGF in Eq. 3.1 is of the form $\boldsymbol{ab}$. We can learn a lot more from the form of the DGF. The second vector ($\boldsymbol{b}$ in $\boldsymbol{ab}$) refers to the layer which contains $\boldsymbol{r'}$ or the source point. The first vector ($\boldsymbol{a}$ in $\boldsymbol{ab}$) refers to the location in which the observation point $\boldsymbol{r}$ is located. Since the medium is homogeneous and infinite, a wave from a source will not undergo any reflections and hence we have the form of the DGF in Eq. 3.1. The discontinuity in the DGF at the source point, $z = z'$ is to take into account the presence of the source. However, in a multilayered medium, a wave from a source region is reflected (and transmitted) at each interface. Consider a particular "parent" wave from the source region. Because of multiple reflections, this wave produces multiple "children" waves in each of the layers. All these waves in each layer can be divided into two groups - waves traveling along $\hat{\boldsymbol{z}}$ direction or those traveling along $-\hat{\boldsymbol{z}}$ direction.

The Green's function for a particular polarization in layers that do not contain the δ source, which we shall call the homogeneous part, is given by:

$$\overline{\overline{G}}^{H}_{e_{lp}}(\boldsymbol{r},\boldsymbol{r'}) = \frac{i}{8\pi^2}\int_{-\infty}^{\infty}\int_{-\infty}^{\infty}\frac{dk_x dk_y}{k_{zs}}\left\{\begin{array}{l} A_l e^{-ik_{z/z_l}} e^{i(\boldsymbol{k}_l.\boldsymbol{r}-\boldsymbol{k}_s\boldsymbol{r'})}\hat{\boldsymbol{x}}\,(k_{zl})\,\hat{\boldsymbol{x}}\,(k_{zs}) + \\ B_l e^{ik_{z/z_l}} e^{i(\boldsymbol{K}_l.\boldsymbol{r}-\boldsymbol{k}_s.\boldsymbol{r'})}\hat{\boldsymbol{x}}\,(-k_{zl})\,\hat{\boldsymbol{x}}\,(k_{zs}) + \\ C_l e^{-ik_{z/z_l}} e^{i(\boldsymbol{k}_l.\boldsymbol{r}-\boldsymbol{K}_s\boldsymbol{r'})}\hat{\boldsymbol{x}}\,(k_{zl})\,\hat{\boldsymbol{x}}\,(-k_{zs}) + \\ D_l e^{ik_{z/z_l}} e^{i(\boldsymbol{K}_l.\boldsymbol{r}-\boldsymbol{K}_s.\boldsymbol{r'})}\hat{\boldsymbol{x}}\,(-k_{zl})\,\hat{\boldsymbol{x}}\,(-k_{zs}) \end{array}\right\} \tag{3.2}$$

In Eq. 3.2, $\hat{\boldsymbol{x}} = \hat{\boldsymbol{e}}$ for a TE wave and $\hat{\boldsymbol{x}} = \hat{\boldsymbol{h}}$ for a TM wave. The DGF itself

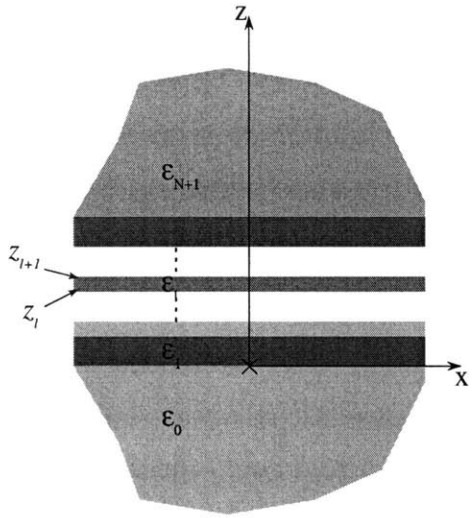

Figure 3-1: Schematic of stratified media for Green's function analysis. Layers of different properties are sandwiched between two semi-infinite half-spaces. The properties are assumed to vary only along the z-axis. The coordinate system is such that layer l is between z_l and z_{l+1}

is a sum of both contributions. The subscript l is to indicate that the DGF is for $\boldsymbol{r}$ belonging to the l^{th} layer and subscript p is to indicate that the DGF is for a particular polarization. We see that each type of plane wave from the source region (say $e^{-i\boldsymbol{k}_s\boldsymbol{r}'}\hat{\boldsymbol{x}}\,(k_{zs})$) produces two types of waves ($e^{i\boldsymbol{k}_l\cdot\boldsymbol{r}}\hat{\boldsymbol{x}}\,(k_{zl})$ and $e^{i\boldsymbol{K}_l\cdot\boldsymbol{r}}\hat{\boldsymbol{x}}\,(K_{zl})$). The DGF in the source layer needs to be augmented to take care of the discontinuity when $z = z'$. This is achieved by the addition of the DGF in Eq. 3.1 to yield:

$$\begin{aligned}\overline{\overline{\boldsymbol{G}}}_{esp}(\boldsymbol{r},\boldsymbol{r}') =& \overline{\overline{\boldsymbol{G}}}^{H}_{esp}(\boldsymbol{r},\boldsymbol{r}') + \\ & \frac{i}{8\pi^2}\int_{-\infty}^{-\infty}\int_{-\infty}^{-\infty}\frac{dk_x dk_y}{k_{zs}}\begin{cases}\hat{\boldsymbol{x}}\,(+k_{zs})\,\hat{\boldsymbol{x}}\,(+k_{zs})\,e^{i(\boldsymbol{k}_s.\boldsymbol{r}-\boldsymbol{k}_s\boldsymbol{r}')}z > z' \\ \hat{\boldsymbol{x}}\,(-k_{zs})\,\hat{\boldsymbol{x}}\,(-k_{zs})\,e^{i(\boldsymbol{K}_s.\boldsymbol{r}-\boldsymbol{K}_s\boldsymbol{r}')}z < z'\end{cases}\end{aligned} \tag{3.3}$$

With the expression for the DGF known the expression for Poynting vector in the z

direction can be determined by computing:

$$\left\langle E_x H_y^* - E_y H_x^* \right\rangle = \pm \frac{\omega^2 \mu_o \varepsilon_o \varepsilon''(\omega)\,\theta(\omega,T)}{8\pi^3} \times \int_{z_{s-1}}^{z_s} dz' \int_{-\infty}^{-\infty}\int_{-\infty}^{-\infty} \frac{\omega}{c}\frac{dk_x dk_y}{|k_{zs}|^2} \left\{ \begin{array}{l} P_l^* Q_l \hat{\boldsymbol{x}}(k_{zs}) \cdot \hat{\boldsymbol{x}}(k_{zs})\, e^{-i(k_{zs}-k_{zs}^*)z'} + \\ R_l^* Q_l \hat{\boldsymbol{x}}(-k_{zs}) \cdot \hat{\boldsymbol{x}}(k_{zs})\, e^{-i(k_{zs}+k_{zs}^*)z'} + \\ P_l^* Q_l \hat{\boldsymbol{x}}(k_{zs}) \cdot \hat{\boldsymbol{x}}(-k_{zs})\, e^{i(k_{zs}+k_{zs}^*)z'} + \\ R_l^* S_l \hat{\boldsymbol{x}}(-k_{zs}) \cdot \hat{\boldsymbol{x}}(-k_{zs})\, e^{i(k_{zs}-k_{zs}^*)z'} \end{array} \right\} \tag{3.4}$$

where

$$\left. \begin{array}{l} P_l = \sqrt{\varepsilon_l}\,(A_l + B_l)\,; Q_l = \frac{k_{zl}}{(\omega/c)\sqrt{\varepsilon_l}}\,(A_l - B_l)\,; \\ R_l = \sqrt{\varepsilon_l}\,(C_l + D_l)\,; S_l = \frac{k_{zl}}{(\omega/c)\sqrt{\varepsilon_l}}\,(C_l - D_l)\,; \end{array} \right\} \quad \text{for TM polarization}$$

$$\left. \begin{array}{l} P_l = (A_l + B_l)\,; Q_l = \frac{k_{zl}}{(\omega/c)}\,(A_l - B_l)\,; \\ R_l = (C_l + D_l)\,; S_l = \frac{k_{zl}}{(\omega/c)}\,(C_l - D_l)\,; \end{array} \right\} \quad \text{for TE polarization}$$

The quantities A_l, B_l, C_l, and D_l are determined by using the boundary conditions (Eq. 2.11 and Eq. 2.12). It should be noted that A_l, B_l and C_l, D_l separate into two independent streams. Effectively, each multilayer system of N thin films and 2 bounding regions, as shown in Fig. 3-1, has $2N + 2$ unknowns (2 for each thin film and 1 for each bounding semi-infinite region) for every source "parent" wave. Each interface furnishes 2 equations and the multilayer system with N thin films has $N + 1$ interfaces. Thus, each of the unknown coefficients can be determined. The most popular method of solving for the unknown coefficients may be the transfer matrix method [54]. The details of the method are given in [55]. With the DGF for the multilayer system known, the radiative transfer in two types of 1D system will be discussed in the next three sections.

3.3 Enhancement in thermal radiation due to near-field effects

To talk about enhancement in heat transfer, generally across vacuum, the value of N in the system shown in Fig. 3-1 is set to 1, i.e, we have one thin film sandwiched between two semi-infinite media. If the intervening medium is vacuum (or any material with no losses), it is possible to make a clear distinction between "far-field" effects and "near-field" effects. In the case of vacuum, all waves with $k_\rho < \omega/c$ lead to "far-field" radiation which can be modelled using classical radiative transfer theory [56–58]. When the gap becomes comparable to the wavelength, interference effects become important. However, it is the effect of those waves with $k_\rho > \omega/c$ that leads near-field enhancement effects. Enhancement due to near-field effects happens because the gaps between objects become small enough that evanescent waves that normally decay in vacuum begin to contribute. Before going into the application of near-field effects for thermophotovoltaic energy conversion, I will discuss evanescent waves and surface waves and see how they affect thermal radiation.

3.3.1 Non-resonant evanescent waves

An introduction to evanescent waves generally begins with the description of the phenomenon of total internal reflection. Beyond a critical angle of incidence, electromagnetic waves incident at an interface of a material with lower refractive index are completely reflected. The waves in the medium with lower index decay rapidly giving rise to evanescent waves. With air or vacuum as the material of lower refractive index, this criteria includes all waves with $k_\rho > \omega/c$. The effect of tunneling of evanescent waves in enhancing the radiative energy transfer becomes appreciable only when the spacing between the participating bodies is less than the characteristic wavelength of the thermal radiation, as given by Wien's law. The nature of enhancement in radiative transfer due to evanescent waves of the type that give rise to total internal reflection phenomena is shown in Fig. 3-2. The two objects are assumed to have the

dielectric function 12 + 0.00001i for all frequencies. The temperature of one of the objects is 1000 K and the other object is at 300 K. Under such conditions, we notice a broadband enhancement because evanescent wave enhancement occurs at all wavelength. Naturally, the deviation from classical Stefan-Boltzmann law becomes more apparent at cryogenic temperatures, where the characteristic wavelength is of the order of 75 μm (4 K) to 60 μm (50 K). The effect of small spacing on radiative transfer between two non-lossy, semi-infinite dielectrics separated by a layer of vacuum was investigated as early as 1967 [16]. It was found that the radiation tunneling contribution decays rapidly with increase in spacing and is no longer important beyond a characteristic thermal wavelength. However, the source of thermal radiation was not specified, since the dielectrics were assumed to be non-absorptive. Polder and Van Hove analyzed radiative energy transfer between closely spaced bodies for the first time based on the FD theorem [20]. Caren [59] investigated the thermal radiation between closely spaced metal surfaces at low temperature using the concept of surface impedance. (At low temperatures, and hence long wavelengths (50 μm 100 μm), the mean free path of electrons exceed the skin depth and the dielectric function can be replaced by a surface impedance [60]. This condition is knows as the extreme anomalous skin effect (EASE). This, however, is valid only when the absolute magnitude of the dielectric function at that frequency is very high and is not valid at optical frequencies.) In the case of low temperature (cryogenic) energy transfer between two good conductors, the radiative energy transfer follows a d^{-4} behavior, whereas at room temperatures or higher it is d^{-2}. This difference in behavior can be easily seen by appropriate approximations. In the case of near-field energy transfer, the evanescent waves dominate in energy transfer. Hence $k_z = \sqrt{(\omega/c)^2 - k_\rho^2} \approx ik_\rho$. In the metal this approximation is valid only when the refractive index or dielectric function is not too large in magnitude. This happens to coincide with the short wavelength regions, which are encountered in radiative energy transfer at room temperatures or higher. On the other hand for wavelength which are important at cryogenic temperatures $k_z = (\omega/c)\sqrt{\epsilon}$. With these approximations, it can be shown easily that the radiative transfer exhibits d^{-2} behavior at short wavelength and d^{-4} behavior at long

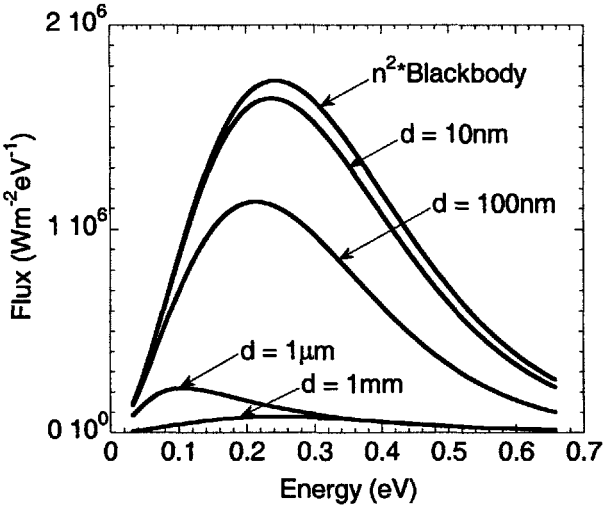

Figure 3-2: Radiative enhancement due to evanescent waves between two semi-infinite objects with a vacuum gap. The value of the gap is indicated adjacent to each curve. The two objects are assumed to have the dielectric function 12 + 0.00001i for all frequencies. The temperature of one of the objects is 1000 K and the other object is at 300 K. Under such conditions, we notice a broadband enhancement because evanescent wave enhancement occurs at all wavelength.

wavelengths. Various theories and regimes involved in near-field energy transfer are discussed in greater depth in Whale [34].

3.3.2 Electromagnetic surface waves - resonant effects

With improvements in microfabrication technology, the idea for utilizing the close gap enhancement for TPV applications has been studied theoretically as well as experimentally. As seen from Fig. 3-2, the enhancement due to evanescent waves is broadband, favoring the long wavelength photons. An enhancement which is narrow-band, favoring short wavelength photons, would be ideal for TPV applications. Until a few years back, metals and lossy dielectrics were the main candidate materials for investigating effects of near-field energy transfer. Developments in near-field optics [61, 62], surface-enhanced Raman scattering [63], extraordinary transmission of light through sub-wavelength holes [64], etc have led to a greater scrutiny of the role played by electromagnetic surface waves in these phenomena. It has been found that enhance-

ment of radiative energy transfer is especially pronounced when the participating materials can support surface waves. Surface waves are defined to be "waves that propagate along an interface between two different media without radiation" [65]. Of course, such waves are achievable only on perfectly smooth interfaces. Any surface roughness, however minute, will in general lead to radiation. If the two materials at the interface are such that $\epsilon_1\epsilon_2 < 0$, they can support surface waves known as surface polaritons (SP) [65]. We have seen earlier that metals and polar materials exhibit negative dielectric regions in cetain parts of the spectrum. Surface polaritons occurring at the interface between a metal and a lossy dielectric are known as surface plasmon polaritons, whereas those occurring at the interface between a polar material and a lossy dielectric are known as surface phonon polaritons. Figure 3-3 shows the dispersion relation of a surface phonon polaritons at the interface of a half-space of SiC with vacuum. Notice that in the regions between the ω_{LO} and ω_{TO} frequencies the surface polariton dispersion curve lies outside the light cone, indicating that it is a non-radiative mode. The dispersion relation is almost flat at the frequency marked ω_{sp} or the surface polariton frequency. Though these modes cannot contribute to energy transfer in the far-field, they enhance the energy transfer considerably around ω_{sp} in the near-field. The enhanced radiative transfer is discussed in the next section.

3.4 Surface phonon polaritons and thermophotovoltaic conversion

Polar materials such as SiC, cubic boron nitride (cBN), hexagonal boron nitride (hBN), and boron carbide (BC) have the ability to support surface phonon polaritons. In the frequency range of interest, the dielectric function can be expressed by the relation $\epsilon(\omega) = \epsilon_\infty(\omega^2 - \omega_{LO}^2 + i\gamma\omega)/(\omega^2 - \omega_{TO}^2 + i\gamma\omega)$, where ω_{TO} and ω_{LO} are the transverse and logitudinal optical phonon frequencies, γ is the damping factor, and ϵ_∞ is the high frequency dielectric constant [66]. The values of ω_{LO} and ω_{TO} for SiC [67], BN [68, 69], and BC [70] are listed in Table 3.1. For the case of energy transfer

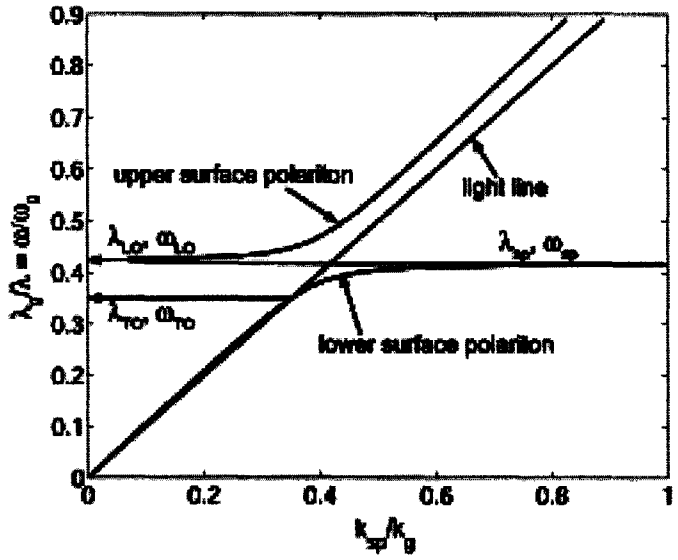

Figure 3-3: The dispersion relation of a surface phonon polariton at the interface between a half-space of SiC and vacuum.

Table 3.1: Values of ω_{LO}, ω_{TO}, γ(in eV) and ϵ_∞ for SiC [67], BN [68,69], and BC [70].

	ω_{LO}	ω_{TO}	γ	ϵ_∞
SiC	0.12	0.098	$\approx 5.88 \times 10^{-4}$	6.7
cBN	0.1616	0.1309	$\approx 6.55 \times 10^{-4}$	4.46
hBN [a]	0.1996	0.1695	$\approx 6.59 \times 10^{-4}$	4.88
hBN [b]	0.1978	0.1872	$\approx 9.92 \times 10^{-3}$	3.9
BC	0.1959	0.1352	[c]	[c]

[a] $\boldsymbol{E} \perp c$, Electric field is perpendicular to optical axis.
[b] $\boldsymbol{E} \parallel c$, Electric field is parallel to optical axis.
[c] Not available.

between two half planes of cBN, one of them ($z < 0$) is at temperature T (1000 K) and the other ($z >$ d) is at room temperature (300 K), separated by a layer of vacuum of thickness d. The results of the analysis are plotted in Fig. 3-4. When the distance between the half planes is much larger than the characteristic wavelength (3 μm - 10 μm), the spectral energy transfer between the two plates reaches a constant value. Notice that there is very little energy transfer between ω_{TO} and ω_{LO} at d = 1 mm. As the distance between the two half planes is decreased, the shape of the spectral energy transfer curve begins to change drastically, the region between ω_{TO} and ω_{LO}

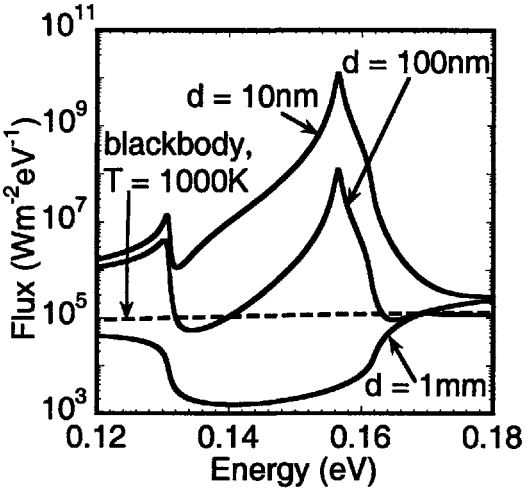

Figure 3-4: Results of analysis of energy transfer between two half planes of cBN.

becoming more and more prominent. At a spacing of 100 nm, the peak spectral energy transfer, at 0.1565 eV, is close to three orders of magnitude larger than the energy transfer between two plane black surfaces at the same temperatures. This increase in energy transfer is because of the tunneling of fields due to the surface phonon polariton modes. The smaller peak that is observed at 0.1307 eV is due to the tunneling of evanescent waves since the dielectric function near ω_{TO} takes on very large values. As the gap decreases, the near-field radiative heat transfer between the two half planes increases as $1/d^2$, similar to the trend described in Section 3.3.1

This narrowband energy transfer phenomenon can be exploited for a TPV application by introducing a thin layer of absorbing PV material as shown in Fig. 3-5. The emitter, cBN, is modeled as a half plane at a temperature T (1000 K). Layer A is a layer of vacuum, B is a layer of PV absorber at room temperature, and C is vacuum. The imaginary and real parts of the dielectric function of the PV material

are assumed to be of the form :

$$\epsilon_i(\omega) = \begin{cases} Ax^{-2}\sqrt{x-1} & , x > 1 \\ 0 & , x < 1 \end{cases} \tag{3.5}$$

$$\epsilon_r(\omega) = \begin{cases} B + Ax^{-2}(2 - \sqrt{1+x}) & , x > 1 \\ B + Ax^{-2}(2 - \sqrt{1+x} - \sqrt{1-x}) & , x < 1, \end{cases}$$

where $x = \hbar\omega/E_g$ and A and B are constants dependent on material properties[66]. This form of the dielectric function is appropriate for direct bandgap semiconductors. For the purpose of our calculation, we have chosen $(A, B, E_g) = (6, 10, 0.13 \text{ eV})$.

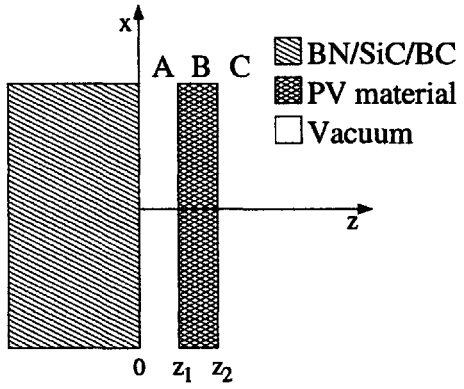

Figure 3-5: Potential structure for TPV application.

The energy absorbed by the PV layer is calculated by computing the difference in the component of Poynting vector normal to the interfaces at $z = z_1$ and $z = z_2$. We have chosen the thickness of the PV layer, $z_2 - z_1$, to be 100 nm. For the assumed dielectric function, most of the flux above the bandgap of the PV layer is absorbed. The results for varying thickness of the vacuum layer (layer A) are shown in Fig. 3-6. We see that as z_1 decreases, the flux absorbed by layer B increases in addition to becoming more narrowband in nature.

The total flux absorbed by the PV layer between 0.14 eV and 0.15 eV is plotted in Fig. 3-7 as a function of the vacuum gap thickness. It is seen that the power absorbed at a vacuum gap of 20 nm is 117 Wcm^{-2}, almost three orders of magnitude higher than the solar insolation. At a vacuum gap of 100 nm, the power absorbed

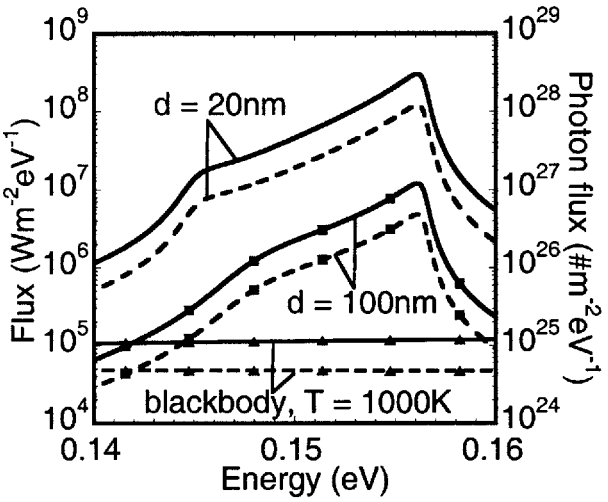

Figure 3-6: Spectral flux absorbed by PV layer for $A = 6$, $B = 10$, $E_g = 0.13$ eV, and 100nm of PV layer. Solid (dashed) lines refer to flux (photon flux). z_1 is the vacuum gap.

is 4.86 Wcm^{-2}. While less than the power emitted by a blackbody source at 1000 K (5.67 Wcm^{-2}), the advantage is that the energy absorbed by the PV layer is in a much narrower bandwidth (Full width half maximum (FWHM) is $\approx 2.5 \times 10^{-3}$ eV as compared to ≈ 0.345 eV for blackbody radiation at 1000 K). While the detailed efficiency analysis for the present TPV cell will be presented elsewhere, a plot of the photon overexcitation efficiency (F_0) [71] is shown in Fig. 3-7. F_0 is defined as the fraction of the energy absorbed by the PV layer that is usable. The value of F_0 is roughly 0.86 for this near monochromatic energy transfer while it is only 0.445 for a blackbody source at 1000 K and similar cell. This is an indication that in addition to improvements in power density, there could be improvements in efficiency as well. With hBN as the radiative layer, materials like InSb or $Hg_{1-x}Cd_xTe$ can be potential materials for the PV layer. In the interest of brevity the results for hBN as emitter, which are similar to the results for cBN, are not presented here.

In summary, we have implemented a general scheme based on a Green's function method and the fluctuation-dissipation theorem to compute radiative energy transfer between layered media. We have used the above method to compute the spectral energy transfer between two half planes. In particular, we have seen that in materials

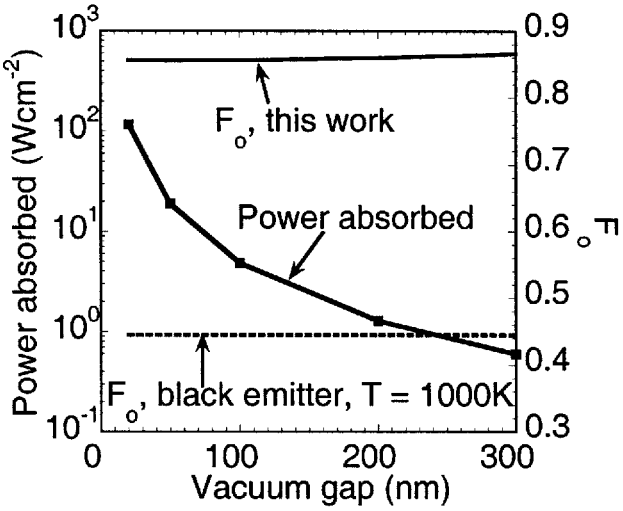

Figure 3-7: Total flux absorbed by PV layer within the range 0.14 eV to 0.16 eV and photon overexcitation efficiency (F_0).

that support electromagnetic surface waves, it is possible to see not only an enhancement but also a narrowband characteristic to the thermal energy transfer between the surfaces. While we have analyzed only materials supporting surface phonon polaritons, plasmon polaritons could also be used to produce a similar effect, generally at higher frequencues. To utilize surface plasmons, we should find the right materials which can support low loss surface plasmon polaritons in the frequency range around 0.3 eV to 0.8 eV to match current TPV materials. We have analyzed the spectral energy transfer between a source material which can support surface waves and an absorbing PV layer. The energy transfer retains a part of the enhancement and narrowband characteristics that we have noticed between the two half planes. This effect can be used to improve the power density and efficiency of low temperature TPV generators. Since this material was published [37], works related to near-field radiative enhancement and thermophotovoltaics have appeared in literature [36, 72, 73]. The efficiency of near-field TPV energy conversion using tungsten emitters and quasi-monochromatic emitters is shown to increase with decrease of gap between emitter and PV cell in [72]. The enhancement of thermal radiation between two half-spaces of doped Si is investigated in [73]. A review of work related to micron-gap TPV

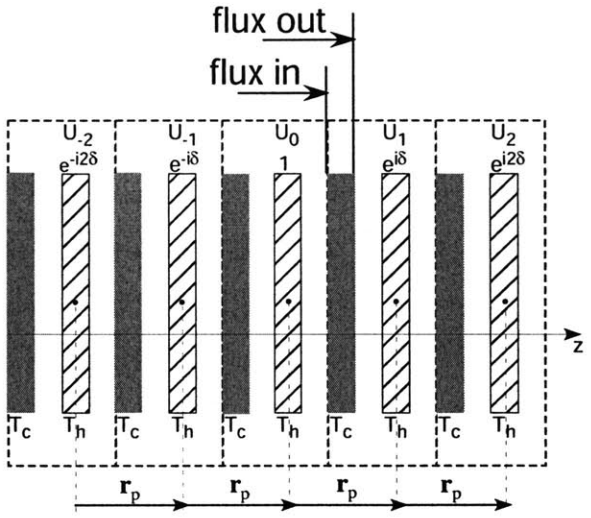

Figure 3-8: 1D periodic system being investigated. Each unit cell consists of 2 layers - an emitter and vacuum in between. $\boldsymbol{r_p}$ is the primitive lattice vector of the 1D periodic structure. The unit cells extend to $-\infty$ and ∞ in the z direction. Each planar layer extends to $-\infty$ and ∞ in the x and y directions, which are in the plane of the layers. .

conversion is available in [36].

3.5 Far-field control of thermal radiation

3.5.1 Thermal radiation in a 1D photonic crystal - Phased array technique

As seen in Chapter 2, the problem of understanding thermal radiation inside a periodic structure entails the determination of the DGF for a 1D photonic crystal that is infinite in extent. The one complication that comes up with infinite periodic media is the lack of sufficient boundary conditions to solve the problem. The two semi-infinite media that bound the thin films in Fig. 3-1 are lacking for the 1D infinite PC shown in Fig. 3-8. This means that we will never have the same number of equations as the number of unknowns. We have to use the symmetry or the repetetive nature of the structure to make up for the lack of sufficient boundary conditions.

Normally, for periodic media, Bloch's theorem is used to determine the band

structure, transmissivity, reflectivity, and other such properties. In this case Bloch's theorem cannot be used because of the presence of the delta source, which disrupts the periodicity. Instead, the problem is circumvented by making use of the phased array method [74]. In this method, a whole array of δ-sources is introduced in addition to the original one, as shown in Fig. 3-8. The dyadic GF of this modified problem, termed the periodic GF, is determined initially. The important thing is that the δ-source in the Nth unit cell to the right (left) of the unit cell in consideration is phase shifted by Nθ (-Nθ) and all of them have the same arbitrary orientation, $\boldsymbol{a}$. It can be shown that the field due to this array of δ-sources is given in terms of the periodic GF by the equation:

$$\boldsymbol{E}(\boldsymbol{r}) = i\omega\mu_o \int_{U_0} \overline{\overline{\boldsymbol{G}}}_{eP}(\boldsymbol{r}, \boldsymbol{r}'; \omega, \theta) \cdot \boldsymbol{a}\delta(\boldsymbol{r} - \boldsymbol{r}')\, d^3r' \tag{3.6}$$

where the integration domain is restricted to the primary unit cell, U_0; and subscript P indicates that the DGF is a periodic DGF. U_0 refers to that unit cell where the δ- source is at zero phase. By appealing to superposition, the periodic DGF can be expressed in terms of the actual GF as:

$$\overline{\overline{\boldsymbol{G}}}_{eP}(\boldsymbol{r}, \boldsymbol{r}'; \omega, \theta) = \sum_{n=-\infty}^{\infty} \overline{\overline{\boldsymbol{G}}}_{e}(\boldsymbol{r}, \boldsymbol{r}' + n\boldsymbol{r}_P; \omega) e^{in\theta} \tag{3.7}$$

$$\Rightarrow \overline{\overline{\mathbf{G}}}_{e}(\mathbf{r}, \mathbf{r}' + n\mathbf{r}_P; \omega) = \frac{1}{2\pi} \int_0^{2\pi} \overline{\overline{\mathbf{G}}}_{eP}(\mathbf{r}, \mathbf{r}'; \omega, \theta)\, e^{-in\theta} d\theta \tag{3.8}$$

where $\boldsymbol{r}_P$ is the primitive lattice vector of the 1D periodic lattice as shown in Fig. 3-8. From Eq. 3.7, it can be shown that:

$$\overline{\overline{\boldsymbol{G}}}_{eP}(\boldsymbol{r}, \boldsymbol{r}' + \boldsymbol{r}_P; \omega, \theta) = \overline{\overline{\boldsymbol{G}}}_{eP}(\boldsymbol{r}, \boldsymbol{r}'; \omega, \theta)\, e^{i\theta} \tag{3.9}$$

The above relation can be used to augment the boundary conditions at the interfaces and the problem is now restricted to only a single unit cell as opposed to an infinite structure. Further details of this problem have been published in [75]. However, the

analysis of this periodic structure proved to be useful in proposing a new type of 1D periodic structure that can mimic the behavior of much more complicated selective emitters - emitters that emit preferentially in parts of the electromagnetic spectrum that are useful to us.

3.5.2 Thermal emission from a 1D metallo-dielectric photonic crystal

Metals are used as emitters for TPV applications because of their inherently low emissivity in the mid- and far-IR. As seen from their usage in incandescent bulbs, tungsten has a relatively good emissivity in the optical (light) as well as near IR (heat) regimes compared to far-IR. While the high emissivity in the near IR is a disadvantage for lighting applications, it is very good for TPV applications with low band gap semiconductors like GaSb (band gap 0.72 eV or 1.72 μm). In fact, the emissivity of tungsten-based emitters is increased by the appropriate use of anti-reflective coatings [76], 1D and 2D surface-relief gratings [77, 78], and 3D PCs [79]. The 1D PC structure itself consists of 10 unit cells, each unit cell composed of a 10 nm film of tungsten (emitter) and a 60 nm film of alumina. We have used measured values of optical constants for tungsten from literature [80]. We have used a damped oscillator model for the dielectric function of alumina with values taken from literature [81]. In order to simulate more closely a practical situation, this PC structure is assumed to be on a dielectric substrate with the metal touching the substrate. The substrate is assumed to have a constant relative electrical permeability of 12. Although alumina could also act as an emitter, the emission from the alumina layers is negligible ($<$ 1%) compared to the emission from tungsten. Hence we have plotted only the emission from the tungsten layers. The spectral hemispherical emissivity of the 1D PC described above is plotted in Fig. 3-9 along with that for a bare tungsten half plane and experimental data from the 3D PC [79]. Compared to the emissivity of bare tungsten, the 1D PC shows increased emissivity at all wavelengths in the range considered. In particular, the emissivity in the near IR and optical regimes is around 0.85

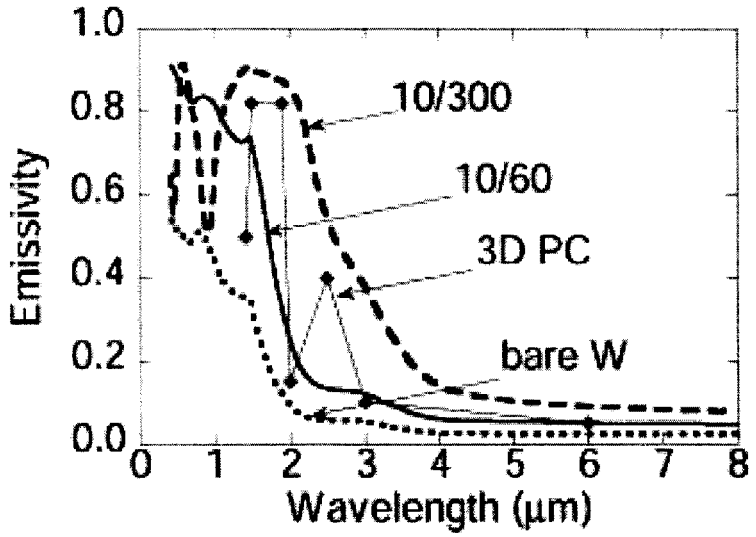

Figure 3-9: Emissivity of tungsten/alumina PC. Curves marked 10/60 and 10/300 refer to 1D PCs with 10 nm of tungsten and 60 nm or 300 nm of alumina. In both cases, the PCs have 10 unit cells with the metal layer deposited on the substrate. The dots refer to experimental data from a 3D PC [79]. The lines connecting the dots are only representative of the experimental curve.

while it remains comparatively lower in the far IR regime. By varying the dielectric thickness, the frequency around which the transition from low emissivity ($\approx$0.1) to high emissivity ($\approx$0.7) occurs can be controlled. Unfortunately the dielectric function of tungsten, unlike that of silver, is such that with a simple 1D PC it seems unlikely that the transition frequency can be decreased below 2.0 μm. Nonetheless, the 1D PC compares very well with the 3D PC and could be a more practical alternative as an emitter technology for TPV applications.

In summary, the following can be said about thermal emission from 1D MDPCs: (1) Metallic films with thickness of the order of the skin depth, when arranged as a 1D PC, exhibit photonic effects which can be used to tailor the spectral emissivity of the PC structure. Generally, this results in an increase in emissivity in the frequency spectrum in consideration. With the right material, the 1D PC offers a simple structure that could have great implications for incandescent bulb technology. (2) One reason the emissivity increases over a broad spectrum could be the effect of the top-most film. Making structural changes to the top-most film could result in

the desired reduction of emissivity. (3) A 1D PC structure made of tungsten thin films exhibits enhancements in emissivity remarkably similar to a more complicated 3D PC. The advantage of the 1D PC is that it can be fabricated much more easily compared to the 3D PC.

3.5.3 Far-field control, quo vadis?

From the results shown in this chapter as well as other publications [79, 82], we see that it is possible by texturing emitters to increase the emissivity. The large increase in emissivity in a part of the electromagnetic spectrum (generally visible or near-IR) is accompanied by an increase in the longer wavelength parts (mid-IR and beyond). This behavior can be explained by considering the emitter to be a medium with an effective dielectric function. The difference between the dielectric function of the emitter and the surrounding medium (generally vacuum) is a measure of how poor the emitter is. The dielectric function performs the role of an impedance and a large difference in the dielectric function results in a large impedance mismatch which leads to low emissivity. Now consider an emitter with a large mismatch in dielectric function with the surrounding medium, assumed to be vacuum. Any texturing of the emitter involved removal of the emitter material, which is replaced by vacuum. In the long wavelength limit, this results in an effective medium with dielectric function inbetween that of the original emitter and vacuum. As long as the emitter does not become transparent, this results in an increase of emissivity. What will be truly interesting is to see whether it is possible by using texturing (surface or volumetric) to decrease the emissivity over a broad band of the electromagnetic spectrum, comparable in extent to thermal radiation (as opposed to decreases over a narrow band, as seen in thin film filters).

Chapter 4

Near-field transfer between spherical surfaces

4.1 Introduction and outline

In Chapter 3, the electromagnetic formulation discussed in Chapter 2 was applied to planar multilayer structures. In particular, the near-field radiative transfer between polar materials is shown to exhibit a hundred-fold enhancement compared to far-field thermal radiation. However, experimental investigation of near-field transfer between parallel plates is no trivial task - a topic that will be discussed further in Chapter 5. In order to overcome some of these challenges, we can replace one or both of the surfaces by a sphere, thereby eliminating the necessity for alignment to achieve parallel surfaces. This idea of using spheres as opposed to planes has been used successfully in measurement of Casimir forces [83–85]. To date, theoretical analysis of heat transfer between a sphere and a plane or between two spheres are limited to the sphere being approximated by a point dipole [86]. It is possible to derive an asymptotic expression for radiative transfer between two large spheres separated by a very small gap (gap is very small compared to the radius of either of the spheres) from the results of radiative transfer between two semi-infinite objects. This idea is used extensively in the Casimir force literature and is known as the proximity force theorem (PFT) [83, 87]. Generally, the diameter of the sphere involved in the

experiments range from a few microns to a few tens of microns, which is no longer in the point dipole approximation. Hence a complete Mie scattering solution to the problem is necessary to verify with experiments as well as to gauge the validity of simpler models. In this chapter, I shall discuss the near-field radiative heat transfer between two spheres using the dyadic Green's function (DGF) of the vector Helmholtz equation [14, 15, 45] and the fluctuation-dissipation theorem [9, 46, 50].

Electromagnetic scattering by a sphere has been very well studied since the seminal work of Mie, almost a century ago. The two sphere scalar and vector scattering problems have also been investigated for almost the same amount of time by many authors [88–90]. The two sphere problem involves expansion of the field in terms of the vector spherical waves (VSW) of each of the spheres and re-expansion of the VSW of one sphere in terms of the VSW of the second sphere in order to satisfy the boundary conditions. The two sphere problem, and multiple sphere scattering in general, is especially tougher due to the computational demands of determining translation coefficients for the (vector) spherical wave functions [88, 91–93]. Recurrence relations for the scalar [94] and vector spherical waves [95] have reduced the computational complexity considerably. In this work, the DGF for the two sphere configuration is determined by satisfying the boundary conditions for fields on the surface of the two spheres. The translation coefficients are determined using the recurrence relations in [94, 95].

The chapter is arranged as follows. In Section 4.2, a simplified, asymptotic result for the radiative heat transfer between two spheres of equal radii, based on the PFT is presented. In Section 4.3 the two sphere problem is described and the DGF for this configuration is determined in terms of the VSW of the two spheres. In Section 4.4, the expression for radiative flux, and thus the spectral conductance, from one sphere to another is determined. Details regarding the convergence of the series solution and numerical solutions for sphere sizes up to 25 μm in diameter is presented in Section 4.5.

4.2 Asymptotic result for near-field thermal radiation

The purpose of this section is to present an asymptotic formula for the radiative heat transfer between two spheres from the results of the radiative heat transfer between two half-spaces [20, 29, 37, 96]. It is possible to define a radiative conductance between the two spheres at temperatures T_A and T_B as:

$$G = \lim_{T_A \to T_B} \frac{P(T_A, T_B)}{|T_A - T_B|} \tag{4.1}$$

where G (units WK^{-1})is the radiative conductance, $P(T_A, T_B)$ is the rate of heat transfer between the two spheres at T_A and T_B. It should be noted that G is a function of temperature. A similar quantity for flat plates is the radiative heat transfer coefficient, h (units $\mathrm{Wm}^{-2}\mathrm{K}^{-1}$). The heat transfer coefficient $h(z)$ in the near-field, especially when dominated by surface polaritons, is known to vary as $1/z^2$, where z is the gap between the half-spaces. The spheres are separated by a minimum gap z. We will assume in this section that the spheres are of equal radii, R. The conductance between two spheres is computed by approximating the spheres to be flat surfaces of varying gap. By doing so we get a relation between G and h given by

$$G(z; R) = \pi z R h(z) \tag{4.2}$$

Since $h(z)$ varies as $1/z^2$, it is expected that $G(z; R)$ varies as $1/z$. The PFT is shown to be valid for the case of dispersion forces between curved surfaces. Despite their origin in fluctuations of the electromagnetic field, a significant difference between force and flux is that forces decay to a negligible quantity in the far-field whereas thermal flux attains a finite value in the far-field. This implies that larger gaps between the spheres contribute very little to forces whereas they could contribute significanly to flux because of the larger areas involved. Hence a PFT type approximation would be valid only when the heat transfer is dominated by contributions from the near-field

region. Hence we expect the result of Eq. 4.2 to be valid only when R is small enough that near-field radiation dominates and $z/R \to 0$. The discussion in Section 4.5 shows that this is indeed true.

4.3 Two sphere problem

The configuration of the two spheres is shown in Fig. 4-1. At the center of each sphere is a coordinate system. Without loss of generality, the two spheres are arranged such that the z-axes of both coordinate systems pass through the line joining the centers. The x axis (and y axis) of both systems are parallel to each other so that a given point in space has the same ϕ coordinate value in both systems. The two spheres are at temperatures T_A and T_B. In order to determine the radiative transfer, we have to determine the DGF when the source point is in the interior of one of the spheres. We shall take the Dirac-delta source point to be in the interior of sphere A. The most convenient way of dealing with DGF in spherical coordinates is to expand the DGF in terms of vector spherical waves [45], which are solutions of

$$\boldsymbol{\nabla} \times \boldsymbol{\nabla} \times \boldsymbol{P}(\boldsymbol{r}) - k^2 \boldsymbol{P}(\boldsymbol{r}) = 0 \tag{4.3}$$

The vector spherical waves we will need are given by:

$$\boldsymbol{M}_{lm}^{(p)}(k\boldsymbol{r}) = z_l^{(p)}(kr)\boldsymbol{V}_{lm}^{(2)}(\theta,\phi) \tag{4.4}$$

$$\boldsymbol{N}_{lm}^{(p)}(k\boldsymbol{r}) = \zeta_l^{(p)}(kr)\boldsymbol{V}_{lm}^{(3)}(\theta,\phi) + \frac{z_l^{(p)}(kr)}{kr}\sqrt{l(l+1)}\boldsymbol{V}_{lm}^{(1)}(\theta,\phi)$$

where $\boldsymbol{M}_{lm}^{(p)}(k\boldsymbol{r})$ and $\boldsymbol{N}_{lm}^{(p)}(k\boldsymbol{r})$ are VSW of order (l,m). l can take integer values from 0 to ∞. For each l, $|m| \leq l$. The superscript p refers to the radial behavior of the waves. For $p = 1$, the $\boldsymbol{M}$ and $\boldsymbol{N}$ waves are regular waves and remain finite at the origin and $z_l^{(1)}(kr)$ is the spherical bessel function of order l. For $p = 3$, the $\boldsymbol{M}$ and $\boldsymbol{N}$ waves are outgoing spherical waves that are singular at the origin and $z_l^{(3)}(kr)$ is the spherical hankel function of the first kind of order l. The radial function

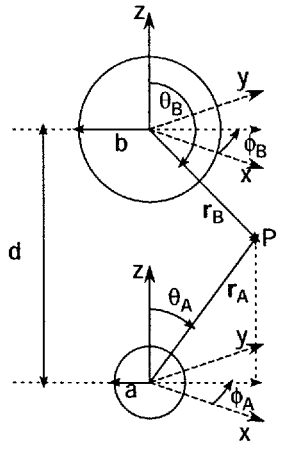

Figure 4-1: Two sphere configuration. Two non-overlapping spheres of radii a and b are separated by a distance d. At the center of each sphere is a spherical coordinate system oriented such that the two spheres lie along the common z axis. The x and y axes are also oriented such that for a given location in space, the ϕ coordinate is the same in both coordinate systems. In this figure, the point P has coordinates (r_A, θ_A, ϕ_A) and (r_B, θ_B, ϕ_B) such that $\phi_A = \phi_B$. Region A(B) refers to the interior of sphere A(B). Region C is the exterior of both spheres and is taken to be vacuum.

$\zeta_l^{(p)}(x) = \frac{1}{x}\frac{d}{dx}\left(xz_l^{(p)}(x)\right)$. $\boldsymbol{V}_{lm}^{(1)}(\theta,\phi)$, $\boldsymbol{V}_{lm}^{(2)}(\theta,\phi)$, and $\boldsymbol{V}_{lm}^{(3)}(\theta,\phi)$ are vector spherical harmonics of order (l,m). The three vector spherical harmonics can be expressed in terms of the spherical harmonics, $Y_{lm}(\theta,\phi)$ as:

$$\boldsymbol{V}_{lm}^{(1)}(\theta,\phi) = \hat{\boldsymbol{r}} Y_{lm} \tag{4.5a}$$

$$\boldsymbol{V}_{lm}^{(2)}(\theta,\phi) = \frac{1}{\sqrt{l(l+1)}}\left(-\hat{\boldsymbol{\phi}}\frac{\partial Y_{lm}}{\partial\theta} + \hat{\boldsymbol{\theta}}\frac{im}{sin\theta}Y_{lm}\right) \tag{4.5b}$$

$$\boldsymbol{V}_{lm}^{(3)}(\theta,\phi) = \frac{1}{\sqrt{l(l+1)}}\left(\hat{\boldsymbol{\theta}}\frac{\partial Y_{lm}}{\partial\theta} + \hat{\boldsymbol{\phi}}\frac{im}{sin\theta}Y_{lm}\right) \tag{4.5c}$$

The vector spherical harmonics are orthonormal to each other and satisfy the following relation:

$$\oint_\Omega \boldsymbol{V}_{lm}^{(r)}(\theta,\phi)\cdot\boldsymbol{V}_{pq}^{(s)*}(\theta,\phi)d\Omega = \delta_{rs}\delta_{lp}\delta_{mq} \tag{4.6}$$

where the integration domain Ω refers to the surface of a sphere of unit radius and $d\Omega$ is a differential area element on such a sphere. The VSW $\boldsymbol{M}_{lm}^{(p)}(k\boldsymbol{r})$ and $\boldsymbol{N}_{lm}^{(p)}(k\boldsymbol{r})$ are related by $\boldsymbol{N}_{lm}^{(p)}(k\boldsymbol{r}) = \frac{1}{k}\boldsymbol{\nabla}\times\boldsymbol{M}_{lm}^{(p)}(k\boldsymbol{r})$ and $\boldsymbol{M}_{lm}^{(p)}(k\boldsymbol{r}) = \frac{1}{k}\boldsymbol{\nabla}\times\boldsymbol{N}_{lm}^{(p)}(k\boldsymbol{r})$. Any solution

to Eq. 4.3 can be expressed as a linear combination of the vector spherical waves. Further properties of spherical harmonics and vector spherical harmonics useful for this analysis is included in Appendix A. In this particular case, the field is a linear combination of VSW of the two coordinate systems as shown in Fig. 4-1. To satisfy the boundary conditions on the surface of each sphere the VSW of one coordinate system should be expressed in terms of the VSW of the other coordinate system. This is what is achieved by means of translation addition theorems for VSW.

4.3.1 Coefficients for translation addition theorems

The vector translation addition theorem [45, 95, 97]states that:

$$\boldsymbol{M}_{lm}^{(p)}(k\boldsymbol{r}_b) = \sum_{\substack{\mu=-\nu \\ \nu=1}}^{\substack{\nu=\infty \\ \mu=\nu}} \left[A_{\nu\mu}^{lm}(+kd)\boldsymbol{M}_{\nu\mu}^{(q)}(k\boldsymbol{r}_a) + B_{\nu\mu}^{lm}(+kd)\boldsymbol{N}_{\nu\mu}^{(q)}(k\boldsymbol{r}_a)\right] \tag{4.7a}$$

$$\boldsymbol{N}_{lm}^{(p)}(k\boldsymbol{r}_b) = \sum_{\substack{\mu=-\nu \\ \nu=1}}^{\substack{\nu=\infty \\ \mu=\nu}} \left[B_{\nu\mu}^{lm}(+kd)\boldsymbol{M}_{\nu\mu}^{(q)}(k\boldsymbol{r}_a) + A_{\nu\mu}^{lm}(+kd)\boldsymbol{N}_{\nu\mu}^{(q)}(k\boldsymbol{r}_a)\right] \tag{4.7b}$$

The position vectors $\boldsymbol{r}_a$ and $\boldsymbol{r}_b$ refer to the same location in space in coordinate systems A and B respectively. Computing the coefficients $A_{\nu\mu}^{lm}(+kd)$ and $B_{\nu\mu}^{lm}(+kd)$ has been the topic of many publications [91–93, 95]. Generally, the expressions for the coefficients require calculations of Wigner 3j symbols which involve calculations of large number of factorials making it computationally expensive. Recurrence relations for computing the coefficients efficiently have been proposed by Chew [95]. In the case of the two sphere problem, with translation along the z-axis alone, Eq. 4.7 simplifies so that the coefficients are non-zero for $\mu = m$ alone.

In the region C (exterior to both spheres), the electric and magnetic fields should be expanded in terms of outgoing VSW of both coordinate systems so that waves decay as $1/r$ as $r \to \infty$. Hence $\boldsymbol{M}_{lm}^{(3)}(k\boldsymbol{r}_b)$ and $\boldsymbol{N}_{lm}^{(3)}(k\boldsymbol{r}_b)$ need to be expressed in terms of $\boldsymbol{M}_{\nu m}^{(p)}(k\boldsymbol{r}_a)$ and $\boldsymbol{N}_{\nu m}^{(p)}(k\boldsymbol{r}_a)$ on the surface of sphere A and vice versa. Since $|\boldsymbol{r}_a| = a < d$ for all points on the surface of sphere A, only the regular VSW or $\boldsymbol{M}_{\nu m}^{(1)}(k\boldsymbol{r}_a)$

and $\boldsymbol{N}_{\nu m}^{(1)}(k\boldsymbol{r}_a)$ should be used. In addition to $A_{\nu m}^{lm}(+kd)$ and $B_{\nu m}^{lm}(+kd)$, we will also need $A_{\nu m}^{lm}(-kd)$ and $B_{\nu m}^{lm}(-kd)$, which can be obtained through symmetry relations [98]. For further details regarding the computation of the recurrence relations, the reader is referred to [94, 95].

4.3.2 DGF - vector spherical wave expansion

The DGF for any configuration can be split into two parts - one that corresponds to a Dirac-delta source in an infinite medium, $\overline{\overline{\boldsymbol{G}}}_o$ and one that takes into account the scattering, $\overline{\overline{\boldsymbol{G}}}_{sc}$. In this case, the source point is confined to the interior of sphere A. The DGF for source point in sphere A, assuming the whole space to of the same material, is given by:

$$\overline{\overline{\boldsymbol{G}}}_o(\boldsymbol{r}_a, \boldsymbol{r}'_a) = \frac{\hat{\boldsymbol{r}}\hat{\boldsymbol{r}}}{k_a^2}\delta(\boldsymbol{r}_a - \boldsymbol{r}'_a) + ik_a \sum_{\substack{m=-l \\ l=1}}^{\substack{l=\infty \\ m=l}} \begin{cases} \boldsymbol{M}_{lm}^{(1)}(k_a\boldsymbol{r}_a)\boldsymbol{M}_{l,-m}^{(3)}(k_a\boldsymbol{r}'_a) + \boldsymbol{N}_{lm}^{(1)}(k_a\boldsymbol{r}_a)\boldsymbol{N}_{l,-m}^{(3)}(k_a\boldsymbol{r}'_a) & \text{if } r_a < r'_a \\ \boldsymbol{M}_{lm}^{(3)}(k_a\boldsymbol{r}_a)\boldsymbol{M}_{l,-m}^{(1)}(k_a\boldsymbol{r}'_a) + \boldsymbol{N}_{lm}^{(3)}(k_a\boldsymbol{r}_a)\boldsymbol{N}_{l,-m}^{(1)}(k_a\boldsymbol{r}'_a) & \text{if } r_a > r'_a \end{cases} \tag{4.8}$$

In particular, we are interested in the case where $r_a > r'_a$ since the source is inside the sphere A whereas the boundary of interest is the surface of the sphere. The part of the DGF that depends on the boundaries takes different forms in the three regions, A, B, and C. Inside A, the DGF is a combination of $\overline{\overline{\boldsymbol{G}}}_o$ and $\overline{\overline{\boldsymbol{G}}}_{sc}$, whereas outside A the DGF is entirely $\overline{\overline{\boldsymbol{G}}}_{sc}$. Each term, $\boldsymbol{M}_{lm}^{(3)}(k_a\boldsymbol{r}_a)$ or $\boldsymbol{N}_{lm}^{(3)}(k_a\boldsymbol{r}_a)$, in Eq. 4.8 can be thought of as an independent VSW that produces scattered waves, i.e. coefficients of scattered waves due to $\boldsymbol{M}_{lm}^{(3)}(k_a\boldsymbol{r}_a)$ (or $\boldsymbol{N}_{lm}^{(3)}(k_a\boldsymbol{r}_a)$) are completely decoupled from VSW of other orders. Let us consider the scattered field due to $\boldsymbol{M}_{lm}^{(3)}(k_a\boldsymbol{r}_a)$. The

scattered field in the three regions is given by:

$$\sum_{\nu=(m,1)}^{\infty} \begin{cases} ik_a\left[\left(A_{\nu m}^{lM}\boldsymbol{M}_{\nu m}^{(1)}(k_a\boldsymbol{r}_a)+A_{\nu m}^{lN}\boldsymbol{N}_{\nu m}^{(1)}(k_a\boldsymbol{r}_a)\right)+\left(B_{\nu m}^{lM}\boldsymbol{M}_{\nu m}^{(3)}(k_a\boldsymbol{r}_b)+B_{\nu m}^{lN}\boldsymbol{N}_{\nu m}^{(3)}(k_a\boldsymbol{r}_b)\right)\right] & \text{, in A} \\ ik_f\left[\left(C_{\nu m}^{lM}\boldsymbol{M}_{\nu m}^{(3)}(k_f\boldsymbol{r}_a)+C_{\nu m}^{lN}\boldsymbol{N}_{\nu m}^{(3)}(k_f\boldsymbol{r}_a)\right)+\left(D_{\nu m}^{lM}\boldsymbol{M}_{\nu m}^{(3)}(k_f\boldsymbol{r}_b)+D_{\nu m}^{lN}\boldsymbol{N}_{\nu m}^{(3)}(k_f\boldsymbol{r}_b)\right)\right] & \text{, in C} \\ ik_b\left[\left(E_{\nu m}^{lM}\boldsymbol{M}_{\nu m}^{(3)}(k_b\boldsymbol{r}_a)+E_{\nu m}^{lN}\boldsymbol{N}_{\nu m}^{(3)}(k_b\boldsymbol{r}_a)\right)+\left(F_{\nu m}^{lM}\boldsymbol{M}_{\nu m}^{(1)}(k_b\boldsymbol{r}_b)+F_{\nu m}^{lN}\boldsymbol{N}_{\nu m}^{(1)}(k_b\boldsymbol{r}_b)\right)\right] & \text{, in B} \end{cases} \tag{4.9}$$

where the symbol $(m,1)$ refers to the greater of m and 1. $A_{\nu m}^{lM}$ is a coefficient of a VSW of order (ν,m) that it is produced by a VSW of order (l,m) . The superscript M (N) is to indicate that it is a coefficient of a $\boldsymbol{M}$ $(\boldsymbol{N})$ wave. In practice, the upper limit for the summation is resticted to a value N_m which depends on k_fd. The appropriate value of N_m will be discussed in Section 4.5. Using Eq. 4.9, Eq. 2.11, and Eq. 2.12, the following set of coupled linear equations can be obtained for the coefficients of the VSW in the scattered field in region C:

$$C_{\eta m}^{lM}+u_\eta(a)\sum_{\nu=(m,1)}^{N_{max}}\left[D_{\nu m}^{lM}A_{\eta m}^{\nu m}(-k_fd)+D_{\nu m}^{lN}B_{\eta m}^{\nu m}(-k_fd)\right]=p_\eta^M\delta_{\eta l} \tag{4.10a}$$

$$C_{\eta m}^{lN}+v_\eta(a)\sum_{\nu=(m,1)}^{N_{max}}\left[D_{\nu m}^{lM}B_{\eta m}^{\nu m}(-k_fd)+D_{\nu m}^{lN}A_{\eta m}^{\nu m}(-k_fd)\right]=0 \tag{4.10b}$$

$$D_{\eta m}^{lM}+u_\eta(b)\sum_{\nu=(m,1)}^{N_{max}}\left[C_{\nu m}^{lM}A_{\eta m}^{\nu m}(+k_fd)+C_{\nu m}^{lN}B_{\eta m}^{\nu m}(+k_fd)\right]=0 \tag{4.10c}$$

$$D_{\eta m}^{lN}+v_\eta(b)\sum_{\nu=(m,1)}^{N_{max}}\left[C_{\nu m}^{lM}B_{\eta m}^{\nu m}(+k_fd)+C_{\nu m}^{lN}A_{\eta m}^{\nu m}(+k_fd)\right]=0 \tag{4.10d}$$

where η ranges from $(m,1)$ to N_m. $u_\eta(a)$ and $v_\eta(a)$ are Mie coefficients that one encounters in the scattering of a spherical wave by a single sphere and are given by

$$u_\eta(a)=\frac{k_a\zeta_\eta^{(1)}(k_aa)z_\eta^{(1)}(k_fa)-k_f\zeta_\eta^{(1)}(k_fa)z_\eta^{(1)}(k_aa)}{k_a\zeta_\eta^{(1)}(k_aa)z_\eta^{(3)}(k_fa)-k_f\zeta_\eta^{(3)}(k_fa)z_\eta^{(1)}(k_aa)} \tag{4.11a}$$

$$v_\eta(a)=\frac{k_a\zeta_\eta^{(1)}(k_fa)z_\eta^{(1)}(k_aa)-k_f\zeta_\eta^{(1)}(k_aa)z_\eta^{(1)}(k_fa)}{k_a\zeta_\eta^{(3)}(k_fa)z_\eta^{(1)}(k_aa)-k_f\zeta_\eta^{(1)}(k_aa)z_\eta^{(3)}(k_fa)} \tag{4.11b}$$

Expressions for $u_\eta(b)$ and $v_\eta(b)$ are obtained by replacing k_a and a by k_b and b respectively. If the original wave is $\boldsymbol{N}^{(3)}_{lm}(k_a\boldsymbol{r}_a)$ instead of $\boldsymbol{M}^{(3)}_{lm}(k_a\boldsymbol{r}_a)$, the only difference is that the right hand side (RHS) of Eq. 4.10a becomes 0 and the RHS of Eq. 4.10b becomes $p^N_\eta \delta_{\eta l}$. p^M_η and p^N_η are given by

$$p^M_\eta = \frac{-i/(k_f a)}{k_a a \zeta^{(1)}_\eta(k_a a) z^{(3)}_\eta(k_f a) - k_f a \zeta^{(3)}_\eta(k_f a) z^{(1)}_\eta(k_a a)} \tag{4.12a}$$

$$p^N_\eta = \frac{i/(k_f a)}{k_a a \zeta^{(3)}_\eta(k_f a) z^{(1)}_\eta(k_a a) - k_f a \zeta^{(1)}_\eta(k_a a) z^{(3)}_\eta(k_f a)} \tag{4.12b}$$

For a given m, we have $(N_m - (m,1) + 1)$ $\boldsymbol{M}$ waves and $(N_m - (m,1) + 1)$ $\boldsymbol{N}$ waves. We see that the left hand side (LHS) for a given value of m remains the same while the only difference is in the RHS (p^M_η and p^N_η). Once all the coefficients in Eq. 4.10 are obtained, the DGF due to scattering, $\overline{\overline{\boldsymbol{G}}}_{sc}$, and its curl, $\boldsymbol{\nabla} \times \overline{\overline{\boldsymbol{G}}}_{sc}$, can be written as:

$$\overline{\overline{\boldsymbol{G}}}_{sc}(\boldsymbol{r}_a, \boldsymbol{r}'_a) = ik_f \sum_{\substack{l,\nu=(1,m) \\ m=-N_m}}^{\substack{m=N_m \\ l,\nu=N_m}} (-1)^m \left[\begin{bmatrix} \left(C^{lM}_{\nu m} \boldsymbol{M}^{(3)}_{\nu m}(k_f \boldsymbol{r}_a) + C^{lN}_{\nu m} \boldsymbol{N}^{(3)}_{\nu m}(k_f \boldsymbol{r}_a)\right) + \\ \left(D^{lM}_{\nu m} \boldsymbol{M}^{(3)}_{\nu m}(k_f \boldsymbol{r}_b) + D^{lN}_{\nu m} \boldsymbol{N}^{(3)}_{\nu m}(k_f \boldsymbol{r}_b)\right) \end{bmatrix} \boldsymbol{M}^{(1)}_{l,-m}(k_a \boldsymbol{r}'_a) + \right.$$
$$\left. \begin{bmatrix} \left(C'^{lM}_{\nu m} \boldsymbol{M}^{(3)}_{\nu m}(k_f \boldsymbol{r}_a) + C'^{lN}_{\nu m} \boldsymbol{N}^{(3)}_{\nu m}(k_f \boldsymbol{r}_a)\right) + \\ \left(D'^{lM}_{\nu m} \boldsymbol{M}^{(3)}_{\nu m}(k_f \boldsymbol{r}_b) + D'^{lN}_{\nu m} \boldsymbol{N}^{(3)}_{\nu m}(k_f \boldsymbol{r}_b)\right) \end{bmatrix} \boldsymbol{N}^{(1)}_{l,-m}(k_a \boldsymbol{r}'_a) \right] \tag{4.13}$$

$$\boldsymbol{\nabla} \times \overline{\overline{\boldsymbol{G}}}_{sc}(\boldsymbol{r}_a, \boldsymbol{r}'_a) = ik_f^2 \sum_{\substack{l,\nu=(1,m) \\ m=-N_m}}^{\substack{m=N_m \\ l,\nu=N_m}} (-1)^m \left[\begin{bmatrix} \left(C^{lM}_{\nu m} \boldsymbol{N}^{(3)}_{\nu m}(k_f \boldsymbol{r}_a) + C^{lN}_{\nu m} \boldsymbol{M}^{(3)}_{\nu m}(k_f \boldsymbol{r}_a)\right) + \\ \left(D^{lM}_{\nu m} \boldsymbol{N}^{(3)}_{\nu m}(k_f \boldsymbol{r}_b) + D^{lN}_{\nu m} \boldsymbol{M}^{(3)}_{\nu m}(k_f \boldsymbol{r}_b)\right) \end{bmatrix} \boldsymbol{M}^{(1)}_{l,-m}(k_a \boldsymbol{r}'_a) + \right.$$
$$\left. \begin{bmatrix} \left(C'^{lM}_{\nu m} \boldsymbol{N}^{(3)}_{\nu m}(k_f \boldsymbol{r}_a) + C'^{lN}_{\nu m} \boldsymbol{M}^{(3)}_{\nu m}(k_f \boldsymbol{r}_a)\right) + \\ \left(D'^{lM}_{\nu m} \boldsymbol{N}^{(3)}_{\nu m}(k_f \boldsymbol{r}_b) + D'^{lN}_{\nu m} \boldsymbol{M}^{(3)}_{\nu m}(k_f \boldsymbol{r}_b)\right) \end{bmatrix} \boldsymbol{N}^{(1)}_{l,-m}(k_a \boldsymbol{r}'_a) \right] \tag{4.14}$$

4.4 Radiative flux

The radiative heat transfer between the two spheres is calculated from the Poynting vector normal to the surface of sphere B, which in turn depends on the tangential fields on the surface of sphere B. The expression for the DGF can be modified to reflect tangential and normal fields on the surface of sphere B by using Eq. 4.10c and Eq. 4.10d in Eq. 4.13 and Eq. 4.14 and eliminating $\boldsymbol{M}^{(3)}_{\nu m}(k_f \boldsymbol{r}_a)$ and $\boldsymbol{N}^{(3)}_{\nu m}(k_f \boldsymbol{r}_a)$ to result in the following equations:

$$\overline{\overline{\boldsymbol{G}}}_{sc}(\boldsymbol{r}_a, \boldsymbol{r}'_a) =$$

$$= \frac{1}{b} \sum_{\substack{l,\nu=(1,m)\\ m=-N_m}}^{\substack{m=N_m\\ l,\nu=N_m}} (-1)^m \left[\left[\begin{array}{ll} \left(-\dfrac{D^{lM}_{\nu m} z^{(1)}_l(k_b r_b)}{k_b b \zeta^{(1)}_\nu(k_b b) z^{(1)}_\nu(k_f b) - k_f b \zeta^{(1)}_\nu(k_f b) z^{(1)}_\nu(k_b b)} \right) \boldsymbol{V}^{(2)}_{\nu m}(\theta_b, \phi_b) & + \\ \left(+\dfrac{D^{lN}_{\nu m} \zeta^{(1)}_l(k_b r_b)}{k_b b \zeta^{(1)}_\nu(k_f b) z^{(1)}_\nu(k_b b) - k_f b \zeta^{(1)}_\nu(k_b b) z^{(1)}_\nu(k_f b)} \right) \boldsymbol{V}^{(3)}_{\nu m}(\theta_b, \phi_b) & + \\ \left(+\dfrac{(k_b/k_f) D^{lN}_{\nu m} z^{(1)}_l(k_b r_b)(\sqrt{\nu(\nu+1)}/k_b b)}{k_b b \zeta^{(1)}_\nu(k_f b) z^{(1)}_\nu(k_b b) - k_f b \zeta^{(1)}_\nu(k_b b) z^{(1)}_\nu(k_f b)} \right) \boldsymbol{V}^{(1)}_{\nu m}(\theta_b, \phi_b) & \end{array} \right] \boldsymbol{M}^{(1)}_{l,-m}(k_a \boldsymbol{r}'_a) \right.$$

$$\left. + \left[\text{similar terms with primed coefficients}\right] \boldsymbol{N}^{(1)}_{l,-m}(k_a \boldsymbol{r}'_a) \right] \tag{4.15}$$

$$\boldsymbol{\nabla} \times \overline{\overline{\boldsymbol{G}}}_{sc}(\boldsymbol{r}_a, \boldsymbol{r}'_a) =$$

$$\frac{k_f}{b} \sum_{\substack{l,\nu=(1,m)\\ m=-N_m}}^{\substack{m=N_m\\ l,\nu=N_m}} (-1)^m \left[\left[\begin{array}{ll} \left(-\dfrac{(k_b/k_f) D^{lM}_{\nu m} \zeta^{(1)}_l(k_b r_b)}{k_b b \zeta^{(1)}_\nu(k_b b) z^{(1)}_\nu(k_f b) - k_f b \zeta^{(1)}_\nu(k_f b) z^{(1)}_\nu(k_b b)} \right) \boldsymbol{V}^{(3)}_{\nu m}(\theta_b, \phi_b) & + \\ \left(+\dfrac{(k_b/k_f) D^{lN}_{\nu m} z^{(1)}_l(k_b r_b)}{k_b b \zeta^{(1)}_\nu(k_f b) z^{(1)}_\nu(k_b b) - k_f b \zeta^{(1)}_\nu(k_b b) z^{(1)}_\nu(k_f b)} \right) \boldsymbol{V}^{(2)}_{\nu m}(\theta_b, \phi_b) & - \\ \left(+\dfrac{D^{lN}_{\nu m} z^{(1)}_l(k_b r_b)(\sqrt{\nu(\nu+1)}/k_b b)}{k_b b \zeta^{(1)}_\nu(k_f b) z^{(1)}_\nu(k_b b) - k_f b \zeta^{(1)}_\nu(k_b b) z^{(1)}_\nu(k_f b)} \right) \boldsymbol{V}^{(1)}_{\nu m}(\theta_b, \phi_b) & \end{array} \right] \boldsymbol{M}^{(1)}_{l,-m}(k_a \boldsymbol{r}'_a) \right.$$

$$\left. + \left[\text{similar terms with primed coefficients}\right] \boldsymbol{N}^{(1)}_{l,-m}(k_a \boldsymbol{r}'_a) \right] \tag{4.16}$$

Using Eq. 2.16, Eq. 4.15, Eq. 4.16, Eq. A.47, Eq. A.48, Eq. A.49, Eq. A.50, and some algebraic manipulation to yield this expression for the spectral radiative

transfer between the two spheres, one at temperature T_A and the other at T_B:

$$P(\omega;T_A,T_B) = (\Theta(\omega,T_A)-\Theta(\omega,T_B))\frac{a}{b}\times$$
$$\times\sum_{m,l,\beta}\left[\begin{array}{l}\left[\Im\left(\frac{1}{x_\beta(b)}\right)\left|\frac{z_l^{(1)}(k_a a)D_{\beta m}^{lM}}{z_\beta^{(1)}(k_f b)}\right|^2-\Im\left(\frac{1}{y_\beta(b)}\right)\left|\frac{z_l^{(1)}(k_a a)D_{\beta m}^{lN}}{r_\beta^{(1)}(k_f b)}\right|^2\right]\Im\left(\frac{1}{x_l(a)}\right)|x_l(b)|^2\\ \left[\Im\left(\frac{1}{x_\beta(b)}\right)\left|\frac{r_l^{(1)}(k_a a)D_{\beta m}^{\prime lM}}{z_\beta^{(1)}(k_f b)}\right|^2-\Im\left(\frac{1}{y_\beta(b)}\right)\left|\frac{r_l^{(1)}(k_f a)D_{\beta m}^{\prime lN}}{r_\beta^{(1)}(k_f b)}\right|^2\right]\Im\left(\frac{1}{y_l(a)}\right)|y_l(b)|^2\end{array}\right] \tag{4.17}$$

where $x_l(a) = k_a a\zeta_\eta^{(1)}(k_a a)z_\eta^{(1)}(k_f a) - k_f a\zeta_\eta^{(1)}(k_f a)z_\eta^{(1)}(k_a a)$ and $y_l(a) = k_a a\zeta_\eta^{(1)}(k_f a)z_\eta^{(1)}(k_a a) - k_f a\zeta_\eta^{(1)}(k_a a)z_\eta^{(1)}(k_f a)$. Just as in Eq. 4.1, it is possible to define a spectral radiative conductance between the two spheres at a temperature T ($T_A \to T, T_B \to T$) as:

$$G(\omega;T) = \lim_{T_A\to T_B}\frac{P(\omega;T_A,T_B)}{|T_A-T_B|} = k_B\frac{X^2e^X}{(e^X-1)^2}\frac{a}{b}\times$$
$$\sum_{m,l,\beta}\left[\begin{array}{l}\left[\Im\left(\frac{1}{x_\beta(b)}\right)\left|\frac{z_l^{(1)}(k_a a)D_{\beta m}^{lM}}{z_\beta^{(1)}(k_f b)}\right|^2-\Im\left(\frac{1}{y_\beta(b)}\right)\left|\frac{z_l^{(1)}(k_a a)D_{\beta m}^{lN}}{r_\beta^{(1)}(k_f b)}\right|^2\right]\Im\left(\frac{1}{x_l(a)}\right)|x_l(b)|^2\\ \left[\Im\left(\frac{1}{x_\beta(b)}\right)\left|\frac{r_l^{(1)}(k_a a)D_{\beta m}^{\prime lM}}{z_\beta^{(1)}(k_f b)}\right|^2-\Im\left(\frac{1}{y_\beta(b)}\right)\left|\frac{r_l^{(1)}(k_f a)D_{\beta m}^{\prime lN}}{r_\beta^{(1)}(k_f b)}\right|^2\right]\Im\left(\frac{1}{y_l(a)}\right)|y_l(b)|^2\end{array}\right] \tag{4.18}$$

where $X = \hbar\omega/k_BT$. It can be seen from Eq. 4.18 that the spectral conductance has units of $k_B(JK^{-1})$ and can split into two parts, one that depends on temperature and the other that is obtained from the DGF of the two sphere problem. The radiative conductance between the two particles that one would measure in an experiment is the integral of $G(\omega;T)$.

$$G_t(T) = \int_0^\infty G(\omega;T)\,d\omega \tag{4.19}$$

4.5 Numerical results

To ensure that the program written to determine the near-field radiative transfer heat transfer is not misbehaving, a few tests can be performed. One of them is

agreement between the numerical results and the analytic expression for conductance in the point dipole limit. For spherical particles in the 1 nm to 50 nm radius, the numerical results agree well with the expression for conductivity in the point dipole limit [28, 32]. In addition to this another test to ensure the correctness of the method is based on the principle of detailed balance. The radiative conductance between two spheres of arbitrary radii must be independent of the numbering scheme for naming the particles, i.e $G_{12} = G_{21}$, where the subscripts 1 and 2 refer to the two spheres. This is necessary to ensure that when the two spheres are at the same temperature the net heat transfer between the two spheres is zero. It is indeed seen from results shown in Table 4.5 that by switching the position if the spheres, keeping the gap the same, results in the same value of conductance (the relative errors are generally of the order 10^{-14})

Gap (μm)	a (μm)	b (μm)	Conductance (WK^{-1})
0.5	1	2	1.63816×10^{-11}
0.5	2	1	1.63816×10^{-11}
0.8	2	3	3.34409×10^{-11}
0.8	3	2	3.34409×10^{-11}

Table 4.1: Conductance obtained for spheres of unequal radii. By swapping the radii of the spheres, it is seen that the value of conductance remains the same.

4.5.1 Convergence analysis

Though the two-sphere scattering problem has been discussed in literature, the near-field interaction between the two spheres has not been analyzed in detail. In particular, the number of terms required for convergence for the near-field problem has not been mentioned at all. For Mie scattering by a single sphere of radius a and wavevector magnitude k the number of terms for convergence, N_{conv}, is given by [88]:

$$N_{conv} = 1 + ka + 3(ka)^{1/3} \tag{4.20}$$

For the two sphere problem a slightly different criterion based on the center to center distance between the two spheres is proposed and given by [99]:

$$N_{conv} = \frac{1}{2}ekd \tag{4.21}$$

where e is the base of the natural logarithm. Both Eq. 4.20 and Eq. 4.21 are valid criteria for computing far-field quatities, like the scattering coefficient. For the near-field problem, we expect the gap between the two spheres to be of great importance. To determine the number of terms required for convergence of near-field quantities we seek parallels to the much simpler and often investigated problem of near-field transfer between two half-spaces. In the near-field two half-space problem, the equivalent of the number of terms for convergence is the truncation for the in-plane wave vector. For a gap z between the two half-planes, the predominant contribution to radiative flux in those frequency regions where evanescent waves are important is from in-plane wave vectors up to the order of $k_{in} \approx 1/z$. If we can draw an analogy between the in-plane wave vectors in the two half-space problem and the two sphere problem, we can propose a criterion for convergence. In the case of the two-sphere problem, the in-plane wave vector equivalent is given by the wavelength of periodic variations on the surface of the sphere. A given vector spherical harmonic, $\boldsymbol{V}_{lm}^{(p)}(\theta,\phi)$, $(p = 1, 2, \text{or } 3)$ corresponds to a variation $\exp(im\phi)$ along the equator of the sphere. The period of this particular vector spherical harmonic (along the equator) is $2\pi a/m$ and the corresponding wave vector is m/a, where a is the radius of the sphere. For a given gap z between two spheres of radii a (equal for now), the number of terms N_{conv} for convergence should be chosen such that $(N_{conv}/a)z \approx 1$. Hence the convergence criterion for near-field effects is given by:

$$N_{conv} \approx \frac{a}{z} \tag{4.22}$$

For spheres of unequal radii the number of terms depends on the greater of the two radii. The convergence criterion proposed here is an upper limit and depending on the optical properties of the spheres, it could be considerably lesser. For spheres which

exhibit surface wave resonances, Eq. 4.22 is a valid convergence criterion as shown by our numerical investigations. Depending on the configuration of the spheres, the criterion for convergence is given by $max(\frac{1}{2}ekd, \frac{a}{z})$.

Since silica spheres are easily available for experimental investigation, we will present our numerical results of radiative transfer between two silica spheres of equal radii at 300 K. In addition, silica is a polar material and hence supports surface phonon polaritons in certain frequency ranges. The dielectric function of silica is taken from [80]. The real part of the dielectric function is negative for silica in two frequency ranges in the IR – from 0.055 to 0.07 eV and 0.14 to 0.16 eV. It is expected that (and shown later) that surface phonon polariton resonances occur in the these frequency ranges. To confirm the prediction of Eq. 4.22, the contribution to the spectral conductance from each (l, m) mode is plotted as a function of l for different values of m in Fig. 4-2. The spectral conductance is plotted at two frequencies – 0.061 eV and 0.045 eV. The surface polariton mode exists at 0.061 eV but not at 0.045 eV.

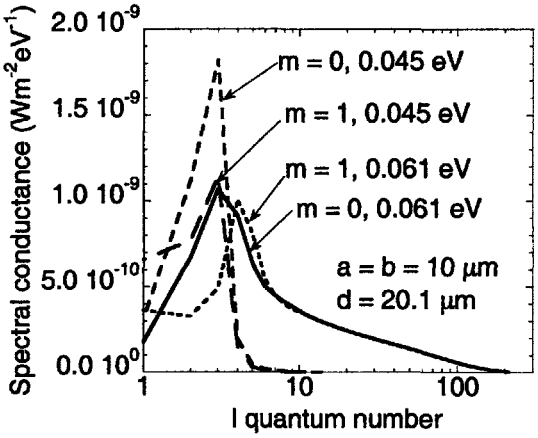

Figure 4-2: Plotted in this figure is the contribution to spectral conductance as a function of l for $m = 0, 1$ at 0.061 eV and 0.045 eV for two spheres of equal radii $a = b = 10\mu m$ at a gap of 100 nm ($d = 20.1\mu m$). Surface phonon polaritons contribute significantly to the radiative transfer at 0.061 eV and not at 0.045 eV. Hence the number of terms required for convergence is significantly lesser than that prescribed by Eq. 4.22

In Fig. 4-3 the spectral conductance at 0.061 eV for $m = 0$ between two spheres

of radius 10 μm is plotted as a function of l for two different gaps - 100 nm and 200 nm. As the gap doubles, the number of terms required for convergence approximately reduces by half, confirming Eq. 4.22. For instance, the spectral conductance is $1.02 \times 10^{-11}\mathrm{WK}^{-1}\mathrm{eV}^{-1}$ at $l = 181$ for 100 nm gap and $l = 99$ for 200 nm gap. The contribution to spectral conductance from smaller values of l ($l \lesssim 15$), corresponding to propagating waves, does not change much with variation in gap. It is the contribution from larger values of l, corresponding to surface waves, that changes appreciably with gap. Based on these results we use at least $N_{max} = 2a/(d-2a)$ terms in our computations. Because of the computation difficulties in solving Eq. 4.10, we present results for a maximum radius to gap ratio of 100 for computations at one frequency and 25 for computations over the spectrum from 0.04 eV to 0.16 eV. Equation 4.10 is solved using the software package Mathematica.

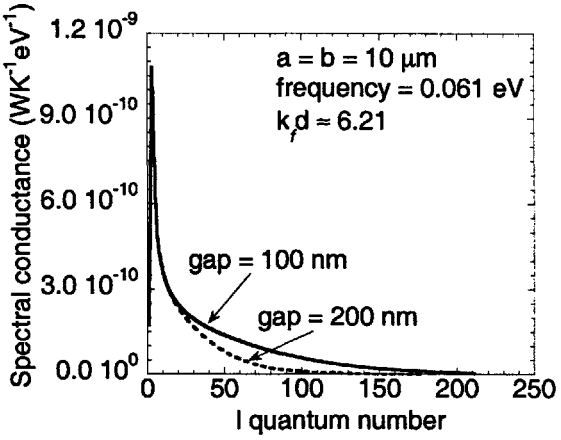

Figure 4-3: Plot of spectral conductance at 0.061 eV between two spheres with equal radii of 10 μm at gaps of 100 nm and 200 nm. The curves plotted are for m = 0.

As mentioned earlier, the symmetry associated with the two-sphere problem allows for solving for the contribution from each value of the m independently, starting from $m = 0$ and proceeding with increasing values of m. As m increases, the contribution to conductance decreases as shown in Fig. 4-4. The computation is stopped when a vacule of m is reached such that the contribution to conductance is less than 5×10^{-3} times the contribution from $m = 0$. Even though the contribution to conductance is significant for terms with $l \approx N_{max}$, the contributions from m drops much faster.

This is fortunate - the time taken to compute the conductance is proportional to the number of values of m required.

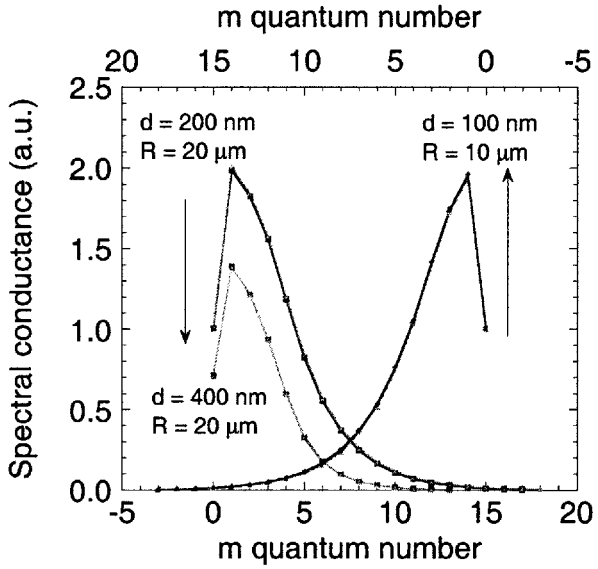

Figure 4-4: Contribution to spectral conductance from each value of m at 0.061 eV. The curves shown are for different values of radius of the spheres and gap between them. The x-axis on the top of figure is reversed and is the abcissa for the spectral conductance of the 10 μm sphere.

4.5.2 Spectral conductance

Unlike the case of near-field radiative transfer between two half-spaces, where the conductance is a function of only the gap between the half-spaces (and the optical properties of the half-spaces and interveing medium), the conductance in the case of sphere-to-sphere radiative transfer varies as a function of the gap as well as the size of the sphere. A gradual transition occurs from a region of near-field dominated radiation to that of far-field dominated radiation. In Fig. 4-5 the spectral conductance between two silica spheres of 1 μm radius is plotted as a function of frequency. We see from the two peaks that the conductance is dominated by the surface phonon polariton regions.

The spectral conductance between the two spheres for larger radii, shown in Fig. 4-6, displays several features of interest. The ratio of radius to gap is maintained

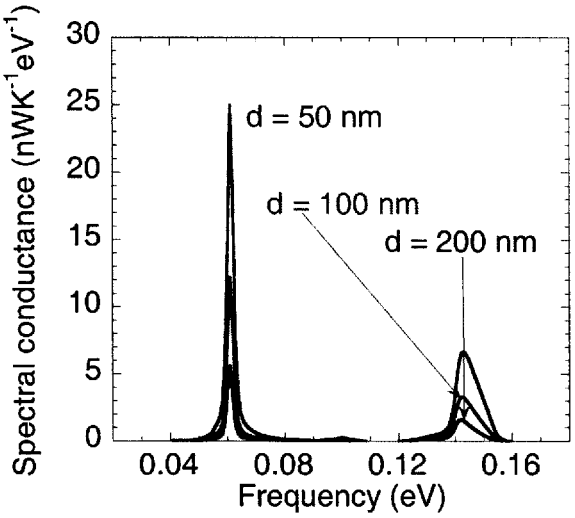

Figure 4-5: Plot of spectral conductance between two silica spheres of 1 μm radii at gaps of 50 nm, 100 nm, and 200 nm from 0.04 eV to 0.16 eV. Surface phonon polaritons in the 0.055 to 0.07 eV range and in the 0.14 to 0.16 eV range contribute to the two peaks seen in the figure.

the same as in Fig. 4-5. Though the height of the peaks remain approximately the same this figure as well as Fig. 4-5, the significant difference is from the contribution from those frequency regions that do not support surface polaritons (0.04-0.055 eV, 0.07-0.14 eV). The contribution to the conductance from these ranges do not vary significantly with gap (as long as gap $\ll$ radius). The relation between the ratio of gap to radius and the contribution to spectral conductance is also illustrated in Fig. 4-7. In Fig. 4-7, the spectral conductance of spheres of radii 1 μm, 2 μm, and 5 μm at gaps of 100 nm, 200 nm, and 500 nm respectively are shown. Since the ratio of gap to radius is a constant (0.1), we expect from the asymptotic theory that value of spectral conductance should also be the same in all three cases. We see from the data that this is approximately the case in the regions where electromagnetic surface waves dominate the heat transfer. In the rest of the region, where near-field radiative transfer is non-resonant, increasing radius leads to increased contribution from propagating waves. The spectral conductance as the radius of the spheres is increased to 20 μm is shown in Fig. 4-8. The increased contribution from the non-resonant parts of the spectrum is evident from the graph. This has an important implication from an experimental

point of view. We should be careful not to increase the size of the sphere to such an extent that the resonant radiative transfer is swamped by the non-resonant radiative transfer. For a 20 μm sphere, we can see that the increase in conductance as the gap decreases is still predominantly due to electromagnetic surface waves as shown in Fig. 4-9. In Fig. 4-9, the increase in spectral conductance as the gap is decreased from 2000 nm is plotted. Compared to Fig. 4-8, the signature of electromagnetic surface waves is clearer from this plot.

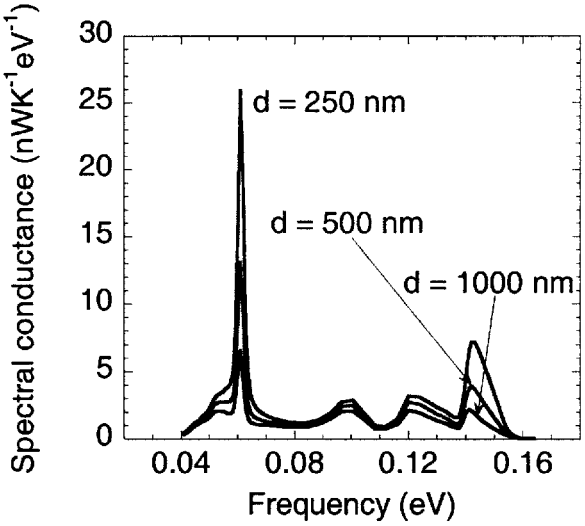

Figure 4-6: Plot of spectral conductance between two silica spheres of 5 μm radii at gaps of 250 nm, 500 nm, and 1000 nm from 0.04 eV to 0.16 eV. The gaps have been chosen so as to maintain the same ratio of gap to radius as for the curves shown in Fig. 4-5.

In Fig. 4-10 the spectral conductance at 0.061 eV (corresponding to the first peak in Fig. 4-5) between two spheres is plotted as a function of gap for different values of the radii. The exponent of a power law fit (of the form $y = Ax^B$) to the data points in Fig. 4-10 is -1.001, -0.984, -0.9024, -0.7781,-0.6119 for radius 1 μm, 4 μm, 10 μm, 20 μm, and 40 μm respectively. As the radius increases from 1 μm to 40 μm, the slope of the curve decreases, indicating an increased contribution from propagating waves. The behavior at smaller radii can be predicted from the variation of conductance with gap between two planes and the PFT, as discussed in Section 4.2. For larger diameters, the PFT type approximation is seen to fail as a result of

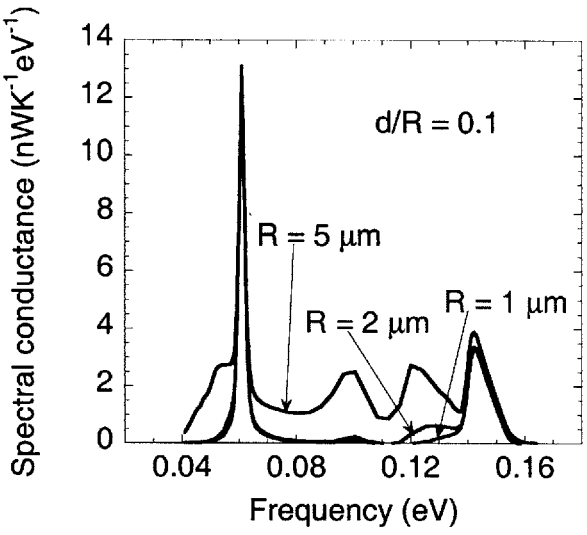

Figure 4-7: Spectral conductance of spheres of radii 1 μm, 2 μm, and 5 μm at gaps of 100 nm, 200 nm, and 500 nm respectively. The value of gap to radius for all the curves is 0.1.

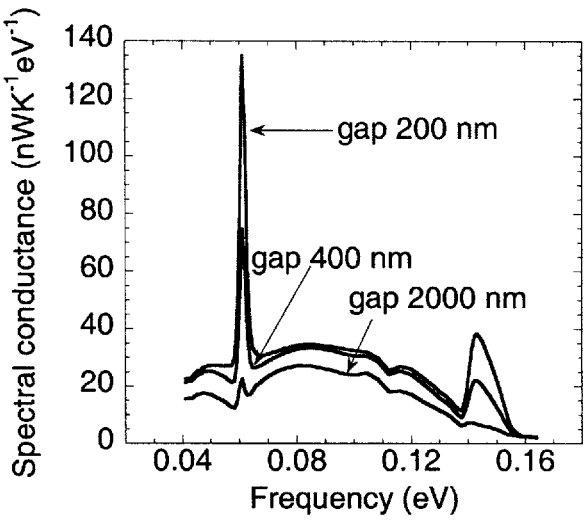

Figure 4-8: Plot of spectral conductance between two silica spheres of 20 μm radii at gaps of 200 nm, 400 nm, and 2000 nm from 0.04 eV to 0.16 eV. Unlike the case of plane-to-plane near-field radiative heat transfer, where the contribution from surface polaritons dominate, the conductance between the two spheres has comparable contributions from the resonant and non-resonant regions.

the far-field contribution.

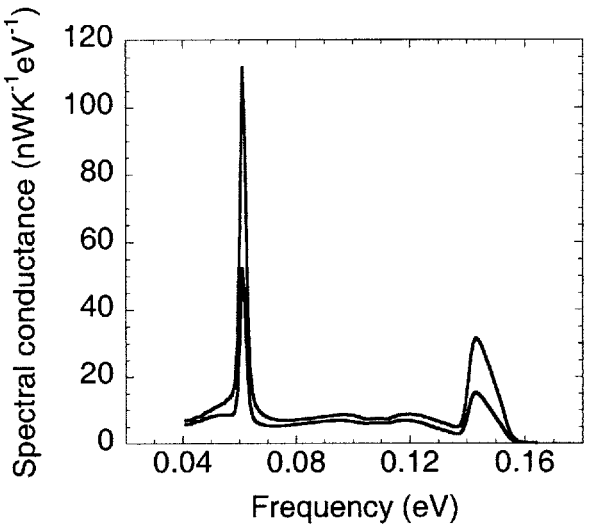

Figure 4-9: The increase in spectral conductance from 2000 nm gap in Fig. 4-8 is shown here for gaps of 200 nm and 400 nm.

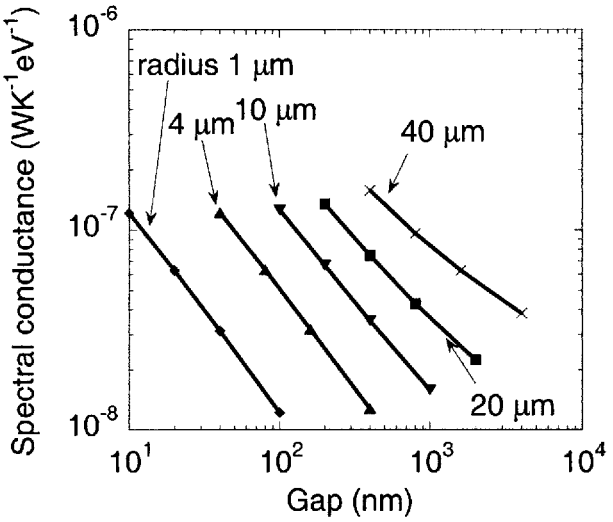

Figure 4-10: Plot of spectral conductance between two spheres of equal radii at 0.061 eV as a function of gap for various radii. For each of the curves, the spectral conductance is computed for the same values of radius/gap. The markers on each curves corresponds to radius/gap values of 100, 50, 25, and 10.

4.5.3 Total conductance

The frequency limits for the calculation of conductance is taken to be 0.041 eV to 0.164 eV. The contribution to conductance from the rest of the frequency spectrum

at 300 K is not significant for spheres of smaller radii. However, it is seen from Fig. 4-8 that frequencies below 0.04 eV contribute to the non-resonant heat transfer. This will not affect the increase in radiative transfer as the gap is decreased because that increase comes predominantly from the regions supporting surface waves. The total conductance for spheres upto radius of 5 μm are plotted against gap in Fig. 4-11. The slope of -6 (approximate) for spheres of radius 20 nm and 40 nm, which can be approximated as point dipoles when the gap between the spheres is much larger than the radius, is in correspondence with the results from the dipole approximation. However, the dipole theory predicts that the conductance should flatten and reach a finite value as the gap decreases to zero, i.e., a slope of zero. What happens in fact is that the near-field effects begin contributing as the gap decreases and the slope in fact decreases from -6 to approximately -1, once again corresponding to the asymptotic theory. However, as the radius increases to 5 μm, the slope decreases further. This decrease is because of increased contribution from non-resonant regions of the spectrum, as seen in Fig. 4-6. For larger values of spheres, the conductance is plotted in Fig. 4-12. On a log-log scale as plotted in Fig. 4-12, the near-field effects are apparent for the spheres of 1 μm and 2 μm. The reason it does not seem so for the spheres of larger diameter is because of the large contribution from the non-resonant parts of the spectrum, as evidenced from the curve corresponding corresponding to the results of classical radiative transfer for the 20 μm sphere. To understand the effects of near-field transfer for larger spheres, the total conductance for 20 μm and 25 μm spheres is plotted in Fig. 4-13. The data points are fit with a curve $G = A_1 x^{-n} + A_2 x + A_3$, where x is the gap, $A_1 x^{-n}$ is the near-field contribution, $A_2 x$ is the contribution due to non-resonant parts of the spectrum (as well as any changes from classical effects due to increase in view factor). We see that the values of the exponent n is 0.5574 for the 20 μm sphere and 0.5035 for the 25 μm sphere. If the asymptotic theory we valid at these values of the gap, one would have expected a value of $n = 1$. It is expected that as the gap decreases, the conductance will approach the form predicted in Eq. 4.1 by the asymptotic theory.

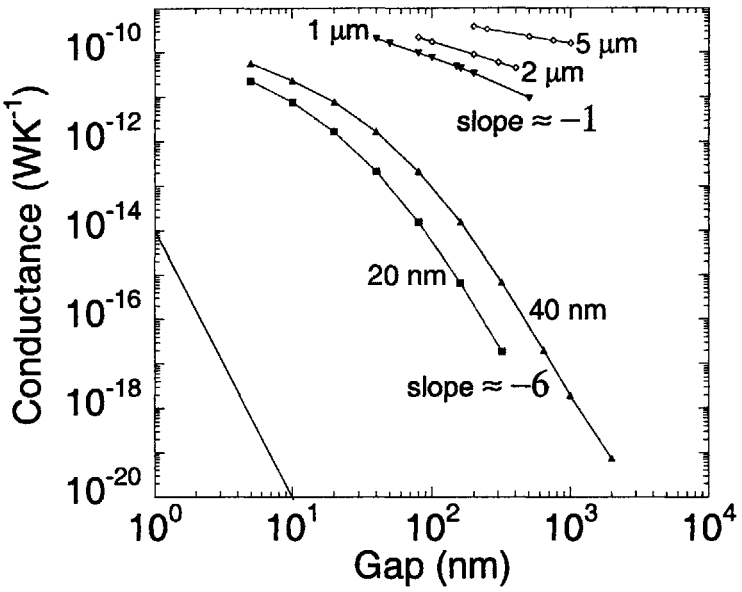

Figure 4-11: Total conductance plotted as a function of gap. The number next to each curve is the corresponding radius of the spheres. For 20 nm and 40 nm spheres, the slope of the conductance vs gap curve is approximately -6 for values of gap larger than the radius of spheres. As the radius of the spheres is increased, the slope gradually changes to approximately -1, corresponding to the asymptotic theory.

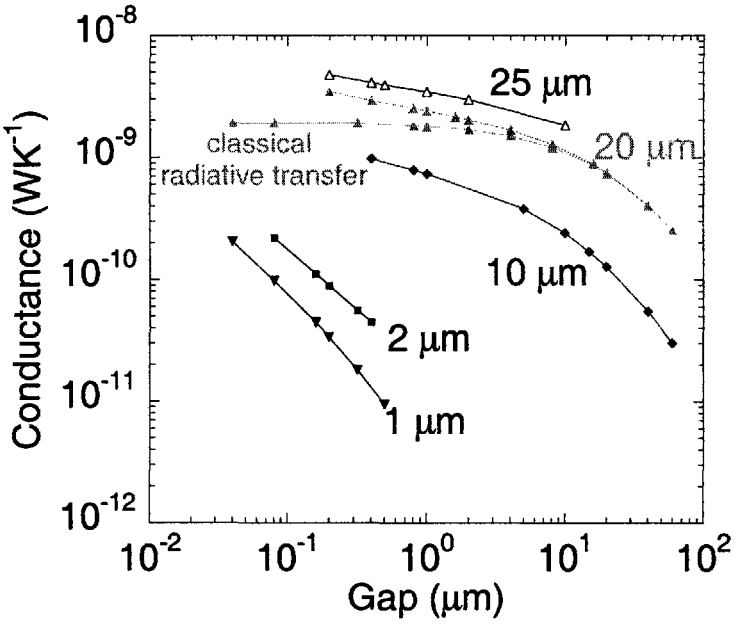

Figure 4-12: Variation of total conductance with gap for various sphere radii.

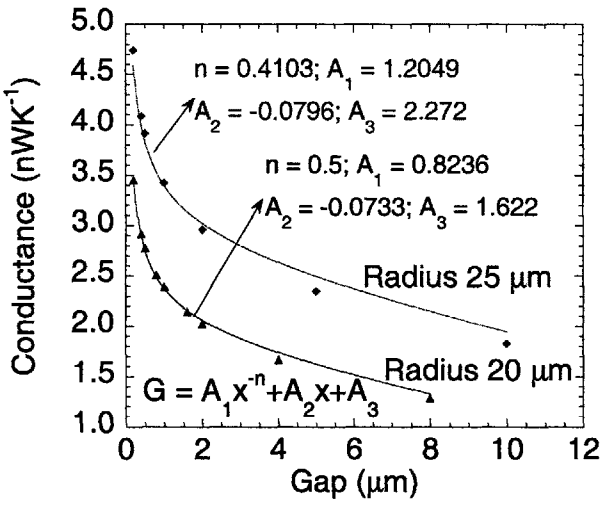

Figure 4-13: Variation of total conductance for spheres of radii 20 μm and 25 μm with gap. The computation has been restricted to a minimum gap of 200 nm because of the stringent numerical requirements of convergence discussed earlier. Notice that the plot is no longer on a log-log scale.

4.6 Regime map for the two-sphere problem

Unlike the two half-space problem discussed in Chapter 3, the two-sphere problem has three length scales - the wavelength in consideration, the radius of the spheres, and the gap between the spheres. Depending on the ratio of the length scales, different approximate theories can be used to predict the conductances. The most obvious one is the case when the radii are large compared to the wavelength and the gap is more than a wavelength. In this case classical radiative transfer can be employed. However, while near-field effects may not be important, interference effects can become important. As the radii of the sphere become comparable or smaller than the wavelength, diffraction effects prevent the usage of classical radiative transfer for even emission from a single sphere. When the radii between the spheres is much smaller than the wavelength, the gaps larger than the diameters of the particles but much smaller than the wavelength, and when the dipole moment of the particles is the dominant contributor to the radiative transfer, the point dipole approximation can be used. However, it should be mentioned that even though the gaps are numerically small,

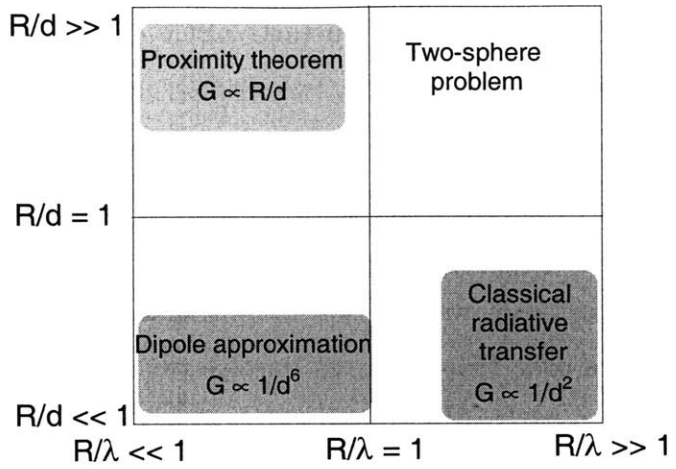

Figure 4-14: Regime map for the two sphere problem. Radius of spheres is R, the gap between them is d, and the wavelength of radiation is λ

this is not a near-field effect in the sense discussed in this thesis. Finally, for spheres with radii not larger than a few microns, the conductance seems to agree with the the proximity approximation when the gaps are much smaller than the radii. These regions in which different theories are applicable can be represented on a regime map with the two axes representing two non-dimensional length scales, as shown in Fig. 4-14.

4.7 Summary

The purpose of solving the two sphere problem is to extend the theoretical and numerical formulations of near-field radiative transfer to configurations of objects which can be tested experimentally. While the two half-space problem is useful to understand the physics of near-field effects, testing its predictions can become extremely challenging, as will be seen in the next chapter. The solution to the two-sphere problem gives us an estimate of the value of radiative conductance one can expect from such an experiment. For microspheres with radii of 25 μm, we expect a radiative conductance between two spheres around 4.5 nWK^{-1} at a gap of 200 nm. From Fig.

4-13, we see that we can expect a conductance of 5.6 nWK^{-1} at a gap of 100 nm. If the experimental configuration is not a two-sphere configuration but a sphere adjacent to a flat plate, the results of this chapter can be used as a guide to estimating the conductance. We expect trends to be similar – that is we expect the increase in conductance to be of the form Ax^{-n}, where x is the gap between the sphere and the flat plate. Most importantly, we expect n to be a number between 0 and 1.

The Mathematica code I have written to solve two sphere problem is included in Appendix B.

Chapter 5

Experimental investigation

5.1 Introduction and outline

In this chapter, the theoretical investigations of Chapter 4 is followed by experimental investigation of a near-field enhancement in a similar configuration. This chapter is arranged as follows: In Section 5.2, the problems associated with existing methods of investigating near-field phenomena are discussed. The principle of the experiment is discussed in Section 5.3. In Section 5.4, the rationale for choosing the bi-material cantilever as the sensor and the experimental setup are described; in section 5.5 the method for obtaining "heat transfer - distance" curves is described and experimental results for conductive heat transfer and radiative heat transfer is presented.

5.2 Previous investigations

Experimental investigations of near field radiative transfer involve meaurement of radiative transfer between two parallel surfaces [19, 21, 22, 100] or between a nanoparticle and a planar surface [101]. Hargreaves measured the enhancement in radiative flux between metallic films of chromium (approximate thickness 100 nm) deposited on optical flats (approximate area 4.8 cm^2) [21] to a gap of 1 μm. Measurements of radiative transfer between copper disks at cryogenic temperatures upto a gap of 50 μm revealed a proximity effect in qualitative agreement with theory [19]. In con-

ducting experiments between macroscopic parallel surfaces, three obstacles have to be overcome:

1. Measuring and maintaing constant gap
2. Measuring, minimizing, and maintaining constant angle (ideally 0^o)
3. Ensuring cleanliness of surfaces

Hargreaves solved the first two problems by measuring the capacitance between the two surfaces (and variants of this technique to measure angle). [21] Capacitance measurements are ineffective if the surfaces are insulators. Presence of dust particles prevented Hargreaves from measuring radiative flux accurately to sub-micron gaps. Xu et al. [22] overcame the third problem by decreasing the area of the surfaces. They measured radiative transfer between a deformed indium surface and a gold surface of area 0.0256 mm^2. By decreasing the area of the surfaces the probability of achieving dust-free surfaces increases, thereby ensuring possibility of achieving smaller gaps. The choice of indium for one of the surfaces is precipated by the fact that it is easy to deform a thin indium needle to conform to the topology of the gold surface, thereby creating parallel surfaces. Though they could attain sub-micron gaps, they did not find any evidence of near-field effects [22]. The problem of dust between the interacting surfaces is one that has been encountered in measurements of forces (van der Waals or Casimir) [102]. Instead of decreasing the size of the surfaces, one of the two planar surfaces is replaced by a curved object. Generally the curved object is a spherical or cylindrical surface, with radius of curvature around 10 cm. A fundamental difference between measuring near-field radiative transfer and forces is the presence of a finite far-field radiation component which increases proportional to the area of the curved surface. The corresponding far-field force is negligible and hence the near-field force can be measured despite using a curved surface of macroscopic radius of curvature.

A different technique to measure the heat transfer has been to replace one of the surfaces by a nanoparticle [101]. The problem of dust is reduced to a minimum

because of the reduced surface area of the nanoparticle. However, measurement of the radiative flux becomes more challenging because of the decreased magnitude. In addition, radiative transfer to other parts of the apparatus to which the nanoparticle is attached can swamp the near-field signal and does not seem to have been taken into consideration in Kittel et al. [101]. Between the two limits of a nanoparticle and a large macroscopic surface is a microsphere. Microspheres have been used extensively to measure van der Waals forces [103] and Casimir forces [84, 85]. It should be possible to measure the heat transfer between a microsphere and a flat substrate. The problem of dust is mitigated compared to the configuration of two flat substrates while the near-field signal is significantly larger than that in the case of the nanoparticle. Another reason that makes a microsphere an attractive option is the fact that no special care needs to be taken to align the sphere to the flat surface. One of the reasons the experiments have been restricted to the case of two flat surfaces or between a nanoparticle and a flat substrate is that the theory to guide the experiments exist only for these cases. The theory presented in the previous chapter partly offsets this problem and extends the fluctuational electrodynamic theory of near-field radiative transfer to configurations more amenable to experimental investigation.

5.3 Principle of experiment

We have seen in the previous chapter that the near-field conductance between two silica spheres of diameter 50 μm is approximately 10^{-8} WK^{-1}. The near-field conductance between a sphere and a flat surface is expected to be of the same magnitude. With a temperature difference of 50 K between the two surfaces, the thermal power to be measured is approximately 500 nW. Not too many sensors are capable of measuring such low thermal heat flux. A scanning thermal microscope tip, such as the XE SThM Nano Thermal Probe (PSIA Inc.) or a thermocouple probe [104] used in a scanning thermal profiler, could be used. The drawback is that the temperature resolution (0.1 ^{o}C) is not enough to measure a flux as small as 500 nW. A similar case can be made for the Wollaston wire probe used to measure the thermal and

thermoelectric properties of nanowires and nanotubes [105]. Another drawback of the Wollaston wire probe (and similar probes) which uses electrical heating of the wire is that any electrical voltage applied to the wire can also induce a force that interferes with the measurement.

Bi-material cantilevers have been used as sensitive thermal sensors, generally to measure infra-red radiation [106–109] or scanning thermal imaging. [110] To measure the deflection of the cantilever, a laser beam in focussed at the tip of the cantilever and the position of the reflected spot is measured using a position sensitive detector. Further discussion of this technique will follow. When they have been used for measuring forces, the defelection of Au/Si_3N_4 cantilevers due to thermal effects is considered to be a minor irritant to be dealt with. In this work it is such a deflection that is to be detected. The deflection of the cantilever due to cooling or heating of the cantilever as the gap between a sphere and a substrate is changed can be measured as a function of the gap yielding a "heat transfer - distance" curve. To maintain a temperature between the sphere and the substrate some method of heat input is required. A convenient solution is provided by the laser beam that is used for detecting the deflection. A part of the laser incident on the cantilever is absorbed by the cantilever and provides the necessary temperature difference between the sphere and the substrate.

5.4 Experimental configuration

A schematic and an image of the experimental apparatus are shown in Fig. 5-1(a) and Fig. 5-1(b). The main components of the apparatus are the laser diode module (LTG, LaserMate Inc., Pomona, CA), a lens system to focus the laser beam, the AFM cantilever and its holder, a substrate mounted on a motion control device (Oriel motor mike), and a position sensing detector (PSD) (duolateral PSD, On-trak Photonics Inc.). A postion sensing amplifier (OT-301, On-Trak Photonics Inc.) is used to convert the output of the PSD into a X and Y output corresponding to the position of the spot on the PSD and a sum output proportional to the laser power incident

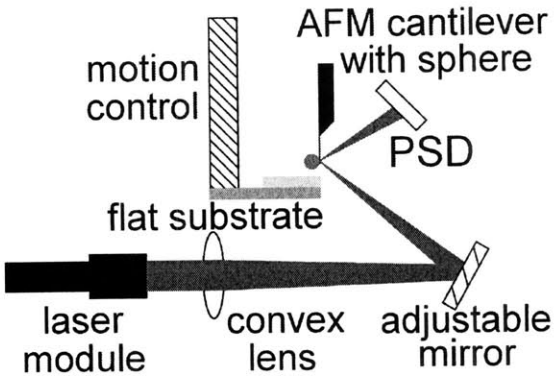

(a) Schematic of experimental apparatus. The beam from a laser diode module is focussed at the tip of an AFM cantilever and the reflected portion is directed onto a PSD.

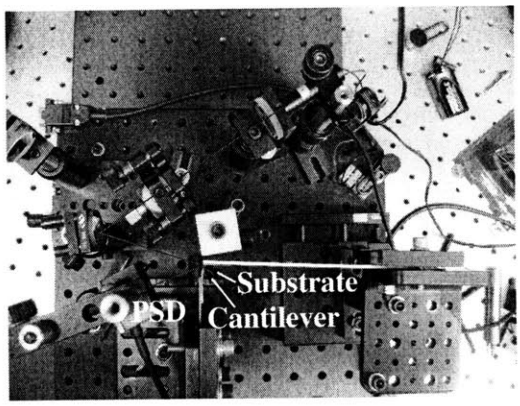

(b) An image of the experimental setup. The red line from the laser diode module to the PSD shows the path of the laser beam.

Figure 5-1: Experimental apparatus to measure heat transfer - distance curves.

on the PSD. All these components are mounted on an standard aluminum optical breadbord ($10'' \times 12''$). To measure the deflection of the cantilever, the PSD X signal is measured using a Keithley 182 nanovoltmeter. The PSD sum signal is measured using a HP33401 multimeter. One way in which this apparatus is different from the AFM is the angle between the cantilever and the substrate. In the AFM, the cantilever is almost parallel to the substrate. The cantilever responds to forces between the sphere and the substrate by bending. Since the cantilever is made of dissimilar materials, it also responds to temperature differences in a similar way. When the cantilever is perpendicular to the substrate, forces on the sphere try to stretch the cantilever as opposed to bending it. The stretching of the cantilever to such forces does not affect the measurement of the deflection due to heat transfer. However, the angle between the cantilever and the substrate is not exactly 90^o. Within the capabilities of alignment in the current experimental setup (see Sec. 5.4.2.2), the angle can be adjusted to $90^o \pm 2^o$. This increases the effective stiffness of the cantilever 28 times compared to stiffness when the cantilever is parallel to the substrate. The response of the cantilever to temperature changes remains the same irrespective of angle between the cantilever and the substrate.

5.4.1 Attaching microspheres to cantilevers

Spherical particles have been attched to AFM cantilevers to study different types of forces. There seems to be no standard method to attach spheres to cantilevers. It is possible to purchase cantilevers with spheres of smaller diameters (0.5 μm to 5 μm) from various vendors of AFM cantilevers. However, in my case I wanted to use cantilevers with larger spheres (50 μm diameter) attached. Attaching such spheres (silica spheres of diameter 50 μm from Corpuscular Inc.) are quite easy and with practice it takes less that 30 minutes to attach a sphere to a cantilever successfully. Figure 5-2 shows the image of the AFM cantilever attached to its holder (Fig. 5-2(a)) and a closeup of the sphere attached to the cantilever (Fig. 5-2(b)). Before attaching the sphere, I attach the AFM cantilever chip to a copper base (C1 in Fig. 5-2) using silver epoxy (epoxy name). I do this to make the handling of the AFM chip easier. The next two steps to attach the sphere to the cantilever are shown in Fig. 5-3. A drop of glue is placed at the edge of a glass substrate as shown in Fig. 5-3(a). By viewing under a microscope (100X magnification), the AFM chip is positioned using a micromanipulator so that the tip touches the drop. A small dab of glue sticks to the tip. A few microspheres are dropped on another glass substrate and some of them are positioned such that they are very close to the edge, as shown in Fig. 5-3. Once the cantilever touches the sphere (as observed through the microscope), I flood the cantilever with UV light for about 20 seconds. It cures the glue sufficiently so that the sphere is now bound to the cantilever. The cantilever is retracted and allowed to cure for another 5 minutes under a UV lamp.

5.4.2 Sources of errors

5.4.2.1 Effect of vibrations

The whole apparatus is placed inside a vacuum chamber during the experiment. In order to reduce the effects of the vibration caused by the mechanical pump and turbo pump, three passive elastomer vibration dampers (Veeco Instruments) are used to separate the apparatus from the rest of the chamber. One way to ensure that the effect

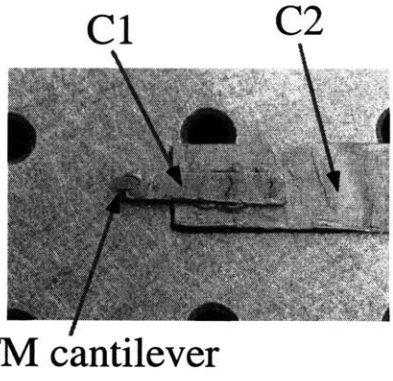

(a) AFM cantilever attached to copper base. The cantilever is attached to base C1 (using silver epoxy) which is later attached to C2 (using the same epoxy). The base C2 is fastened to aluminum breadboard as shown in Fig. 5-1(b)

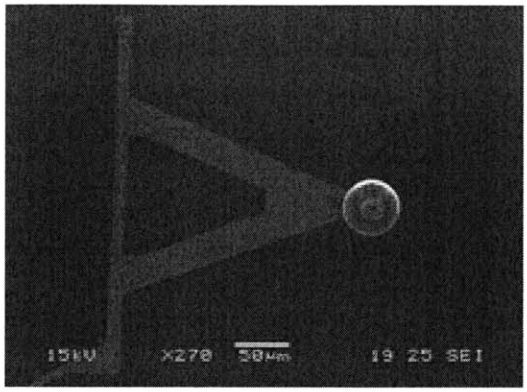

(b) SEM image of silica sphere attached to AFM cantilever.

Figure 5-2: Image of the AFM cantilever holder and a close-up of the cantilever with sphere attached.

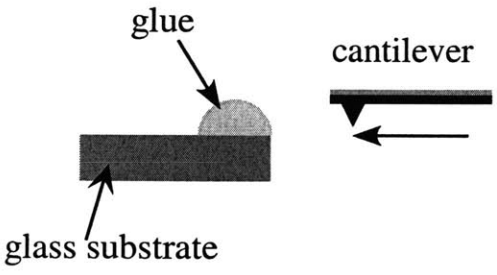

(a) A drop of glue is deposited at the edge of a glass substrate. The cantilever position is adjusted using a micro-manipulator so that the tip just touches the glue. All this is done under a microscope (100X magnification).

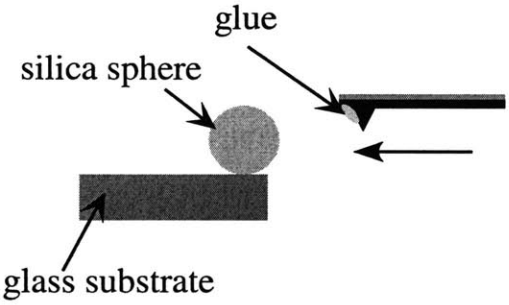

(b) A microsphere is adjusted so that it is right at the edge of a clean glass substrate. The sphere adheres to the glue near the tip.

Figure 5-3: Method of attaching microsphere to cantilever

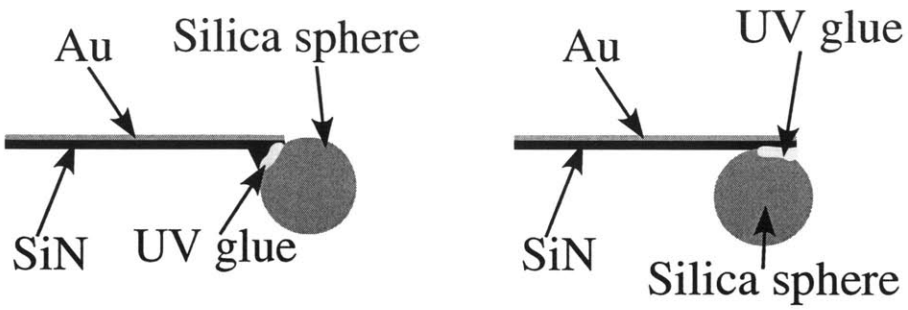

(a) Good attachment.

(b) Bad attachment.

Figure 5-4: Good and bad ways of attaching spheres to cantilevers. The reason for this is discussed in Section 5.4.2

of the mechanical pump and turbomolecular pump is minimized us to measure the noise spectral density of the AFM cantilever. The thermal noise spectrum curves for the cantilever in vacuum, shown in Fig. 5-5, are obtained from the deflection signal of the PSD (PSD X signal) using a lock–in amplifier (SR850, Stanford Research system). The noise spectrum of the cantilever shows the behavior of a damped mass-spring oscillator. By fitting the data to the noise spectrum of a damped harmonic oscillator [111–113], the resonance frequency and the Q-factor can be determined. As shown in Fig. 5-5(a), when the apparatus is well isolated from the vacuum chamber, the noise spectrum curves are "clean" and a consistent value of the resonance frequency and Q factor can be obtained. From six such noise spectrum curves, the resonance frequency was found to be 1.315 $\pm$ 0.0002 kHz. The obtained Q-factor is 316.6 $\pm$ 16.9. While the resonance frequency and Q-factor can be used to understand the forces on the cantilever as the gap between the sphere and the substrate decreases, that is not the purpose of this work.

In contrast to the noise spectrum in Fig. 5-5(a), that for a case when the vibration from the chamber affects the signal is shown in Fig. 5-5(b). The spikes in the noise spectrum are eliminated when the damping is improved. In this case, the culprit was surprisingly three vibration dampers purchased from Radio Shack. On removing the offending dampers, the noise spectrum improved significantly (It was a surprise that adding dampers to the apparatus actually resulted in poorer performance!). This can also be seen from the low frequency noise spectrum, as shown in Fig. 5-6.

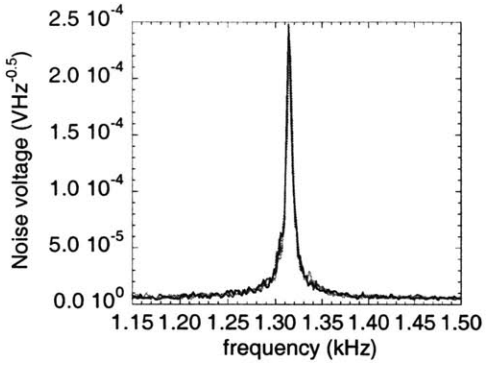

(a) Thermal noise spectrum with good vibration isolation. From a curve fit, the obtained values for the resonance frequency is 1.315 ± 0.0002 kHz.

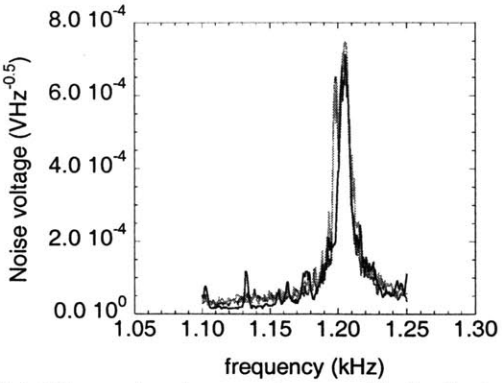

(b) Thermal noise spectrum with bad vibration isolation. The fluctuations in the noise spectrum are because of the rotational motion of the vacuum pump (30 Hz) and its higher harmonics.

Figure 5-5: Thermal noise curves of the cantilever.

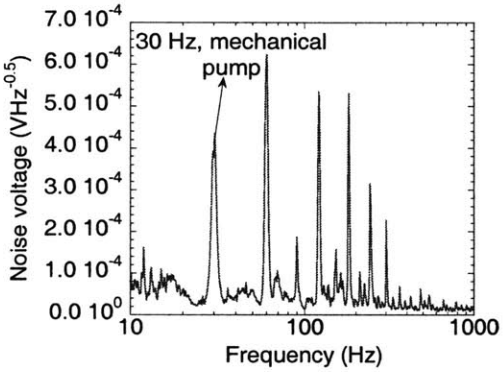

(a) This noise spectrum is the low frequency counterpart of that in Fig. 5-5(b). The peak at 30 Hz is due to the rotation of the mechanical pump. The other peaks are harmonics of the 30 Hz signal.

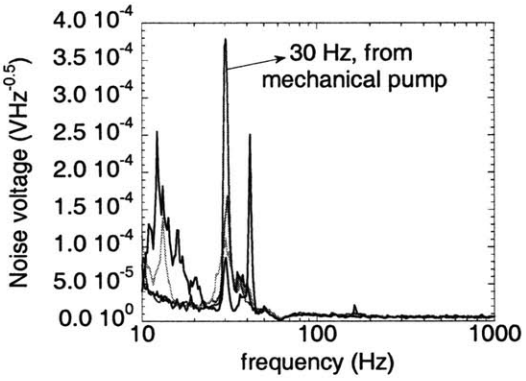

(b) This is the noise spectrum one observes when the offending dampers are removed from the set up (the setup is left with only the three Veeco dampers). Notice the removal of the harmonics of the 30 Hz signal. The main signal at 30 Hz itself remains.

Figure 5-6: Low frequency noise spectrum of the cantilever.

5.4.2.2 Misalignment of cantilever

However, these are not the only sources of error. Shown in Fig. 5-7 is one common source of error. This is due to the position of the cantilever relative to the edge of the substrate. If the cantilever is away from the edge of the substrate, it is likely that as the substrate closes in near the sphere, the edge could intersect a part of

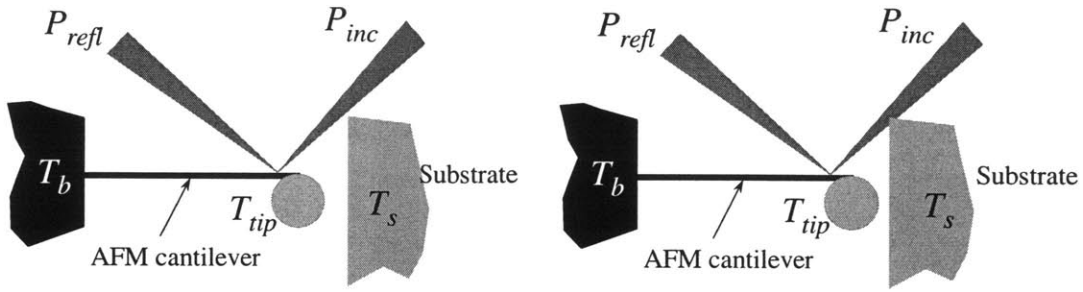

(a) Path of laser beam is obstructed when the gap between the substrate and the sphere is small enough

(b) Path of laser beam is unobstructed when the substrate is sufficiently away from the sphere

Figure 5-7: Restrictions on the positioning of the cantilever and the substrate due to obstruction of the laser beam by part of the substrate

the laser beam, leading to a cooling of the spurious cantilever, as shown in Fig. 5-7. The chances of this error manifesting itself increases if the sphere is attached to the cantilever as shown in Fig. 5-4(b). Another source of error is the angle between the cantilever and the substrate. To ensure that the angle is as close as possible to 90^o, the cantilever and substrate are viewed through a Specwell magnifier and adjusted. A Canon Powershot A95 digital camera is used in conjunction to the Specwell magnifier to take images, as shown in Fig. 5-8, to get an estimate of the angle. A configuration like in Fig. 5-7(b) or Fig. 5-8(b) leads to an error of the form shown in Fig. 5-9, the details of which are discussed in Sec. 5.5.

5.4.2.3 Issue of drift

The bi-material cantilever is a good sensor of choice because of its sensitivity to temperature changes as small as 10^{-4} K. It is precisely this sensitivity that makes the cantilever extremely susceptible to environmental temperature changes as well as any fluctuations in the output of the laser beam. The laser diode module takes approximately 5 hours for the fluctuations in output to decrease and stabilize inside the vacuum chamber. Hence the measurements are all taken at least 5 hours after the turbo-pump is turned on.

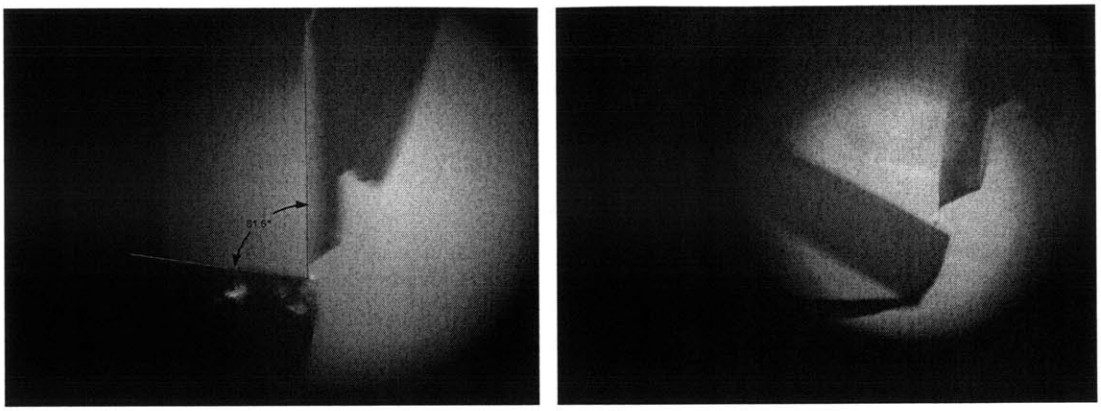

(a) Image of the AFM cantilever aligned almost perpendicularly to the substrate. The cantilever is also positioned such that it is nearly at the edge of the substrate. This ensures that the error described in Fig. 5-7 does not occur in this case.

(b) In this image, the cantilever and the substrate are not aligned perpendicular to each other. In addition the cantilever is positioned away from the edge making it more likely for the error discussed in Fig. 5-7 to occur. In fact, the error does occur and is discussed in Fig. 5-9

Figure 5-8: Images of the AFM cantilever and substrate taken using a hand-held Canon digital camera through a Specwell magnifier mounted on a stand. The magnifier is used to align the cantilever and the substrate.

5.5 Obtaining "heat transfer - distance" curves

Atomic force microscopes have been used since the conception of the AFM to measure the molecular forces between the AFM tip and a substrate or a colloidal particle and a substrate. The cantilever experiences a deflection proportional to the force exerted on it. As the gap between the cantilever and the substrate decreases, the deflection is measured and this gives a measure of the molecular forces once the stiffness of the cantilever is known. The force versus gap curve thus obtained is known as a "force - distance" curve. When bi-material cantilevers are used (Au is used as a reflective coating on one side of the Si_3N_4 cantilever), the cantilever can bend due to forces as well as heat transfer. Since the cantilever is nearly perpendicular to the substrate, it acts as a stiff spring for forces (force have to axially stretch the cantilever) whereas the cantilver is as compliant to heat-transfer. The amount of laser power that is absorbed by the cantilever decreases as the substrate is moved closer to the sphere and manifests as a deflection signal.

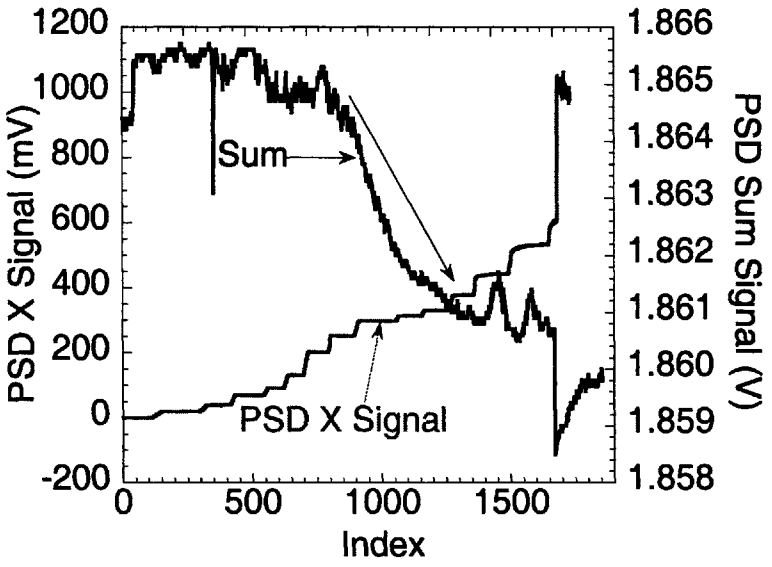

Figure 5-9: A plot of deflection signal (y-axis on left) and PSD sum signal (y-axis on right)corresponding to Fig. 5-7(b) and Fig. 5-8(b). On the x-axis is an index proportional to time. With increasing value of the abscissa the gap is decreasing and the cantilever is cooling, corresponding to increasing deflection or PSD X signal. The PSD sum signal is relatively steady and drops by 3.5 mV as indicated by the black arrow. This happens because the substrate is close enough to the cantilever to obstruct a part of the laser beam from reaching the cantilever. This results in a cooling of the cantilever not related to the cooling due to heat transfer between the sphere and the substrate.

5.5.1 Calibrating the cantilever

To convert the deflection signal to heat absorbed or released from the sphere at the end of the cantilever, a calibration routine is necessary. Fortunately, this can be done without any modification to the apparatus. The power output of the laser diode module can be modified by varying the varying the DC voltage required to power the laser, as shown in Fig. 5-10. By varying the DC voltage to the laser module from 4.0 V to 5.0 V, the power output can be varied from 2.5 mW to 2.75 mW. The variation of laser power with DC voltage is measured using a power meter. This increase in power of the laser causes a heating of the cantilever and hence a change in the PSD X signal. This is also accompanied by an increase in the sum signal because of the increased power incident on the PSD. Two such calibration procedure results are shown in Fig. 5-11 and Fig. 5-12. In Fig. 5-11, the calibration procedure is done

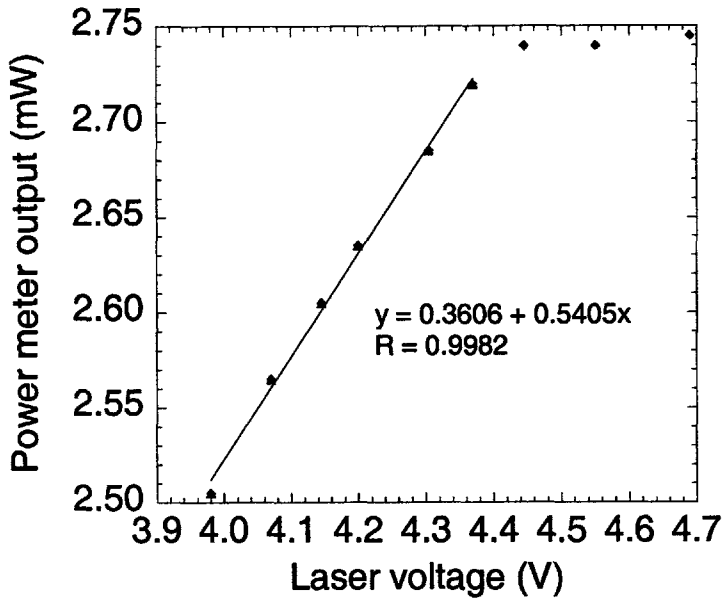

Figure 5-10: Variation of laser power output with power supply voltage. The diode module "turns on" around 3.8 V (data not shown) and varies linearly with voltage in the range between 3.9 V to 4.4 V. Beyond 4.5 V the power output of the module saturates at $\approx$ 2.75 mW.

at atmospheric pressure inside the vacuum chamber. In Fig. 5-12, the calibration is done at 6.6×10^{-3} Pa. When the cantilever is at atmospheric pressure only a part of the absorbed laser power flows through the cantilever and causes a deflection. Natural convection (mainly conduction) from the sphere accounts for rest of the heat loss. When the pressure is as low as 6.6×10^{-3} Pa, the mean free path of air molecules approximately 1 m, much longer than the characteristic lengths affecting heat transfer from the sphere and AFM cantilever (length of the cantilever is 200 μm and diameter of the sphere is 50 μm). Under such conditions, all the laser power absorbed flows through the cantilever and results in a larger deflection signal compared to that when the cantilever is in air at atmospheric pressure.

5.5.1.1 Measuring absorptivity of cantilever

The sum signal from the PSD is an indication of the amount of laser power reflected from the cantilever and incident on the PSD. To determine the relation between the deflection of the cantilever and the power absorbed, the absorptivity of the cantilever

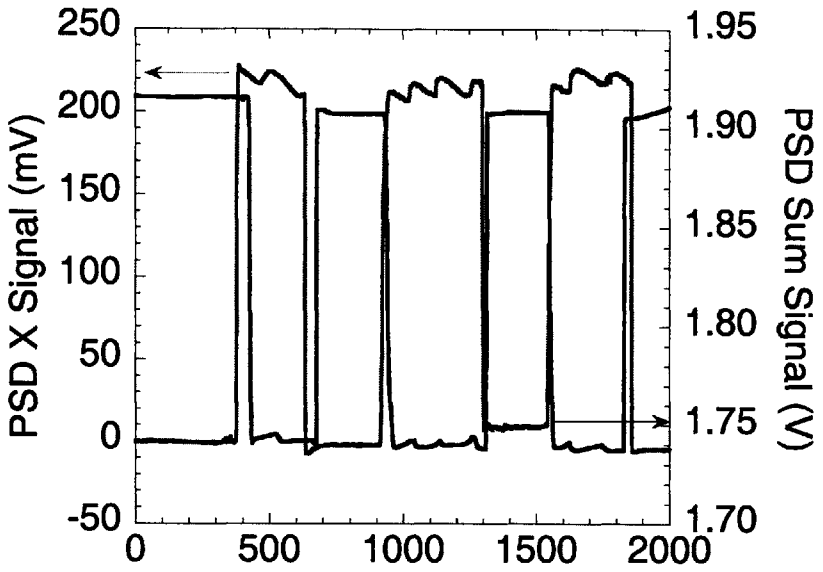

Figure 5-11: Deflection of cantilever in air due to change in incident power. The x-axis is proportional to time elapsed. The deflection signal corresponds to the y-axis to the left. The sum signal corresponds to the y-axis on the right. On changing the power supply voltage from 5.0 V to 3.99 V, the power output of the laser changes from 2.75 mW to about 2.5 mW. This decrease in power results in a cooling of the cantilever as shown by a decrease in the sum signal and a corresponding increase in the deflection signal (increasing deflection signal implies cooling og the cantilever). The shift (in x-axis or time) between the curve corresponding to the delfection signal and the sum signal occurs because of an interval of time between the instant that the datalogger for the sum signal is started and that for the deflection signal is started.

should be known. For a known amount of laser power incident on the cantilever, the absorptivity can be determined by measuring the reflected and scattered light, and using Kirchoff's laws of radiation. The PSD sum signal as measured by the PSD during the experiment is a measure of the reflected power. The main portion of the scattered light is that portion of the incident beam that is slight diffracted by the cantilever but proceeds directly behind the cantilever (as opposed to getting reflected in front of it). This can be estimated by measuring the sum signal with the PSD placed behind the cantilever. The power in the incident beam can be measured by removing the cantilever from the path of the laser so that it is directly incident on PSD screen. The data from one such measurement are shown in Fig. 5-13. The sum signal in the case of reflected signal is 1.911 V, scattered light is 0.306 V, and

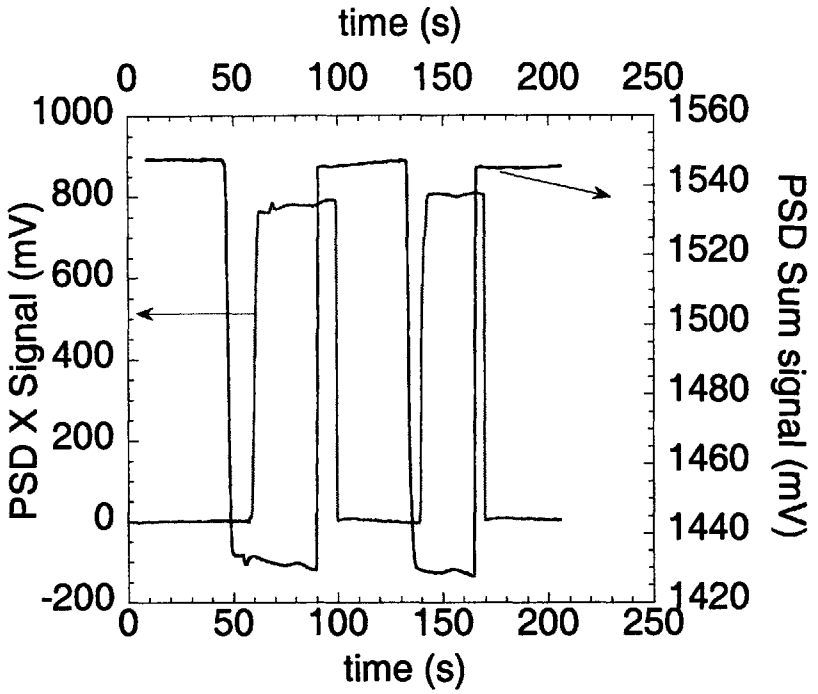

Figure 5-12: A similar curve as in Fig. 5-11 except this is done at 6.6×10^{-3} Pa. The increase in the value for the deflection signal for a similar decrease in sum signal occurs because of the decreased heat transfer from the cantilever and the sphere to the ambient at reduced pressures.

the incident or total is 2.495 V. A significant portion of the scattered light is in fact light that is not directly incident on the cantilever. The cantilever absorption is then proportional to $[2.495 - (0.306 + 1.911)] = 0.278$ V. This results in an absorptivity of approximately 0.11. It should be noted that this is an upper limit for the absorptivity of the cantilever. This is because only a portion of the scattered light (though most of it) is taken into account. In the experiments to be described, it is not the incident (or total) but the reflected light that is measured. The ratio of the absorbed to the reflected signal is given by $0.278/1.911 \approx 0.13$. Finally, it should be mentioned that the DC voltage for the laser diode module is 5.0 V, corresponding to an incident power is approximately 2.75 mW. Hence, a sum signal of 2.495 V corresponds to 2.75 mW or 1.122 mW/V of sum signal.

With the absorptivity of the cantilever known, we can analyze the data in Fig. 5-11 and Fig. 5-12 to calibrate the cantilevers. In Fig. 5-11, the sum signal varies on an average by 0.168 V as the DC voltage to the laser is changed from 5.0 V to 4.0 V. This corresponds to an absorption of $0.13 \times 0.168 \times 1.122$ mW/V $= 24.5\mu$W. At the same

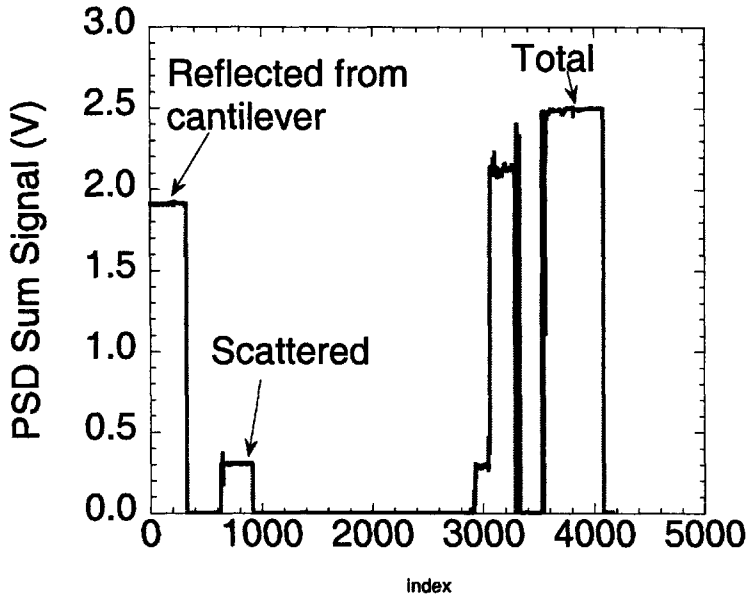

Figure 5-13: PSD sum signal data for measuring the absorptivity of the cantilever.

time, the PSD X signal, corresponding to the deflection of the cantilever, changes by 214.3 mV. This implies that an absorption of 24.5 μW results in a deflection signal of 214.3 mV or a sensitivity of 114.3 μW/V of PSD X signal. A similar analysis of the data from Fig. 5-12 results in a sensitivity of 21.5 μW/V of PSD X signal. This increased sensitivity of the cantilever to heat transfer at the tip is because of the reduced heat losses when the pressure is reduced.

5.5.2 Conductive heat transfer between a sphere and a substrate

The conductive heat transfer between a sphere and a substrate is at least 100 times larger than the heat transfer expected from near-field radiative transfer. Given the problems associated with performing the experiment in vacuum conditions (mainly vibrations) and the coarse nature of the motion control for the substrate, obtaining heat transfer-distance curves for conduction transfer between the sphere and the substrate can be helpful in illustrating the details of the method. Since conduction heat transfer between the sphere and substrate is detectable over larger length scales

(a few multiples of the diameter of the sphere), the coarse nature of the motion control becomes less of an issue. A subset of the data that is plotted in Fig. 5-14 is shown in Table 5.5.2. Each data point is obtained at a given position of the substrate, which can read from a display in the encoder of the Oriel motor mike. At each position, the "PSD X average" and "PSD X stdev" are obtained from the mean and standard deviation of approximately 100 data points. Contact between the sphere and the substrate manifests itself as a large signal in the PSD X signal (as well sum signal). Once the contact point is known, the position of the substrate can be converted to an equivalent gap. The calibration data for these data was shown in Fig. 5-11 and the sensitivity was determined to be 114.3 μW/V. Taking the standard deviation of the PSD X signal ($\approx$ 0.4 mV) as a noise floor for the measurements, we see that we can measure heat-transfers as small as 45.72 nW. In fact, the standard deviation of the measurements can be decreased to less that 0.1 mV by using a slower filter setting in the K182 nanovoltmeter, implying measurement of heat transfer as small as 10 nW. However I have not done so to ensure that the time response of the nanovoltmeter is appropriate for my purpose.

5.5.3 Near-field radiative transfer data

With the vacuum chamber evacuated to approximately 6.6×10^{-3} Pa, the same procedure as described previously to obtain heat-transfer distance curves is repeated. However, there are a few significant differences. The operation of the vacuum pumps during the measurements makes vibration induced noise a greater problem. In addition, the flux is much smaller and that makes the measurement tougher. Near-field effects, as seen from the previous chapter, become noiceable when the gap is approximately 10 μm or less. Given the sensitivity of measurements and the resolution of the motion control stage (100 nm), this allows for only about 6 or 7 data points for each heat transfer-distance curve measurement. The raw data from one of the experiments is shown in Fig. 5-15. Shown in the figure are two curves corresponding to the deflection signal (y axis to the left) and the sum signal (y axis to the right). As time increases along the x-axis, the gap between the sphere and the substrate decreases.

Gap (μm)	PSD X average	PSD X stdev
153	-0.341	0.332
144.4	1.415	0.399
139	4.136	0.325
133.3	7.412	0.311
127.9	10.684	0.347
123.6	13.119	0.350
117.4	17.494	0.334
112.8	20.730	0.294
108.4	23.883	0.271
104.3	27.459	0.346
99.2	32.152	0.354
95.3	35.711	0.502
90.1	40.534	0.309
88	42.786	0.470
84.9	46.033	0.346
79.8	52.307	0.283
75	58.246	0.279
70.5	64.398	0.470
67.4	68.884	0.281
65.1	72.377	0.395
62.5	76.492	0.348
60.1	79.834	0.293
57.6	84.316	0.340
54.9	88.988	0.300
52.3	94.191	0.429
50.1	98.465	0.342

Table 5.1: A subset of the data for a heat transfer-distance curve showing the average values and standard deviation at each value of the gap. All PSD data are given in mV.

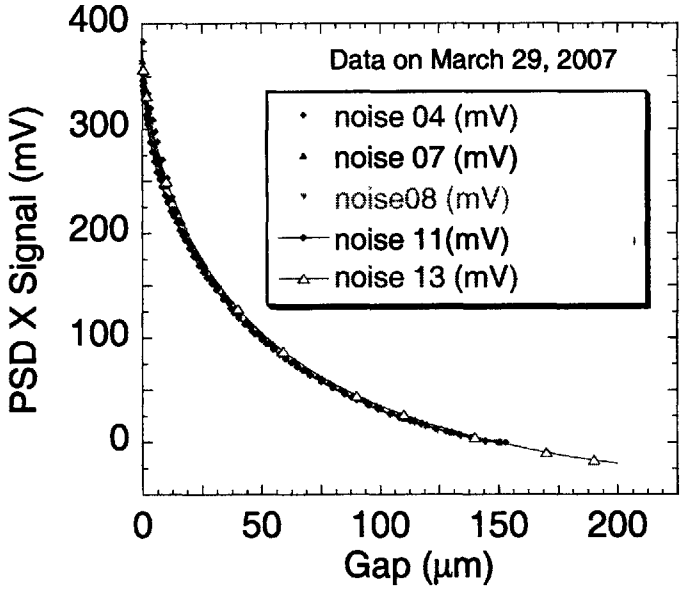

Figure 5-14: Conduction heat transfer between a silica sphere and a silicon substrate as a function of gap. The five curves correspond to five different heat transfer-distance curves

The sum signal curve is noisy but steady and flat even as the gap decreases. This ensures that the signal that is measured is predominantly due to the near-field effect and not due to the spurious effect described in Fig. 5-9. As described in the previous section, the data from multiple heat-transfer distance curves have been averaged and the resulting data is shown in Fig. 5-16. The data corresponding to gaps of less than 2 μm is shown in Fig. 5-17. Shown in the figure is also a curve fit with the function Ax^{-n} as discussed in Chapter 4. From the data, we get a best fit value of $n = 0.5073$ from Fig. 5-16 and $n = 0.4432$ from Fig. 5-17. This is in agreement with the prediction from the numerical results, which predicts an exponent of approximately 0.5 for spheres of radius 25 μm (see Fig. 4-13). From the calibration of the cantilever (Fig. 5-12), we see that a value of 20 mV for the PSD X signal corresponds to 430 nW. Is it possible to estimate the conductance at this value of flux? For that the temperature difference between the sphere and the substrate is necessary. Though the response of the cantilever to power input is known, the response to temperature changes is not know. However, the dimensions of the cantilever, shown in Fig. 5-18 can be used to

Table 5.2: Values of thermal conductivity of thin Si_3N_4 and Au.

Material/Processing	Film thickness (nm)	Thermal conductivity ($Wm^{-1}K^{-1}$)
Si_3N_4/LPCVD	236	2.5 ± 0.1 [115]
Si_3N_4/LPCVD	300	2.4 ± 0.25 [116]
Si_3N_4/PECVD	300	1.8 ± 0.5 [116]
Au/sputtered on quartz	$\approx$ 650 nm	$\approx$ 190 [117]

estimate the conductance of the cantilever. The thickness of the Si_3N_4 layer is 450 nm and that of the Au layer is 70 nm (from vendor data). The thermal conductivity of bulk Si_3N_4 is approximately 30 $Wm^{-1}K^{-1}$ and that of bulk Au is 296 $Wm^{-1}K^{-1}$ [107, 114]. The conductance of each leg is approximately 7 $\times 10^{-6}$ $Wm^{-1}K^{-1}$. From Fig. 5-12, we know that the sum signal is approximately 1.54 V. The absorbed power is then $(1.54/2.485) \times 0.13 \times 2.75$ mW = 221 μW. This implies a temperature difference of approximately 15.75 K. This estimate of temperature difference implies a near-field radiative conductance of 430 nW/15.75 K = 27.3 nWK^{-1}. This value for conductance seems to be larger than what the theory predicts. However, it is well known that the thermal conductivity of thin films can be considerably lower than that of the bulk material. Sample values of the thermal conductivity of thin film Si_3N_4 and Au from literature given in Table 5.2. Assuming the reduced thermal conductivity of Si_3N_4 and Au to be 2.5 $Wm^{-1}K^{-1}$ and 100 $Wm^{-1}K^{-1}$ respectively, the conductance of the cantilever reduces to 3.32 $\times 10^{-6}$ WK^{-1}. With this as the conductance of the cantilever, the temperature difference between the tip and the substrate is 66.6 K, resulting in a conductance of 6.46 nWK^{-1}. This value of the conductance is much closer to what is expected from theory. Using the values of conductivity and dimensions of the cantilever stated above, the near-field radiative conductance from the data in Fig. 5-16 is plotted in Fig. 5-19. A theoretical estimate of the near-field radiative conductance between a sphere and a substrate is also shown in the figure. The method described in Chapter 4 cannot be used to predict the near-field radiative conductance between a sphere and a substrate due to computational restraints. However, the aymptotic theory described in Sec. 4.2 predicts that the near-field radiative conductance between a sphere and a substrate is twice the conductance between two spheres [118]. Due to the lack of a better theory, I have estimated the near-field

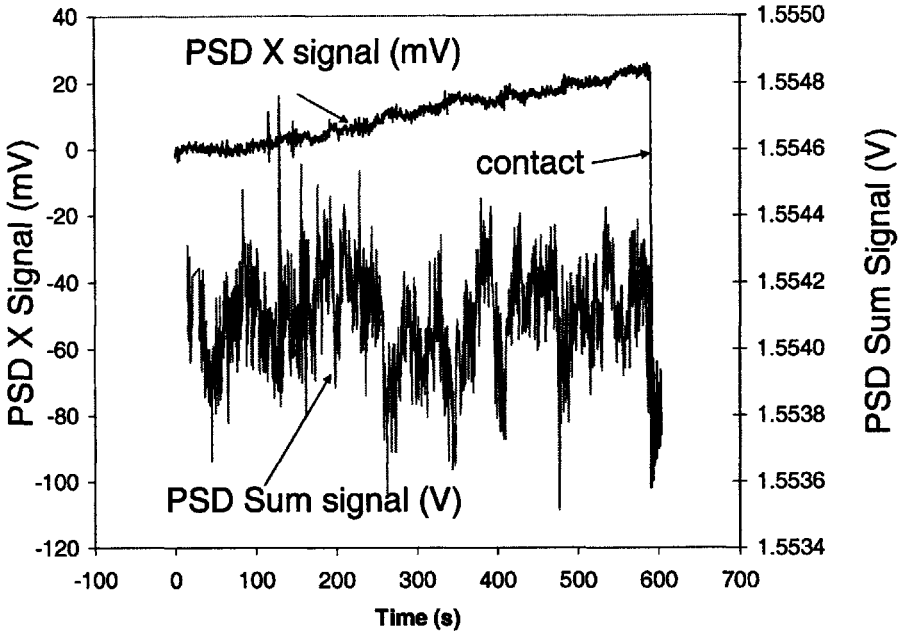

Figure 5-15: Raw data from one experiment to obtain a heat transfer - distance curve

conductance between the sphere and the substrate by multiplying the near-field conductance (only the part of the conductance that varies as $A_1 x^{-n}$) from Fig. 4-13 by 2. It is seen from Fig. 5-19 that the experimental results are in agreement with theory. However, further experimental modifications as suggested in Sec. 5.6 should enable better confirmation of theory with experiments.

5.6 Improving the current experimental apparatus

I list a few methods by which the experiment can be refined. I believe there can be at least a 100 fold decrease in the minimum flux that can be measured. The steps are:

1. Use a better vacuum chamber. Ideally, it should be possible to pump down the chamber and switch off all the pumps and retain the pressure inside the chamber at 10^{-3}Pa. If this is possible, vibration induced noise can be decreased significantly.

2. Use better motion control for the substrate. I did try to use a simple lever

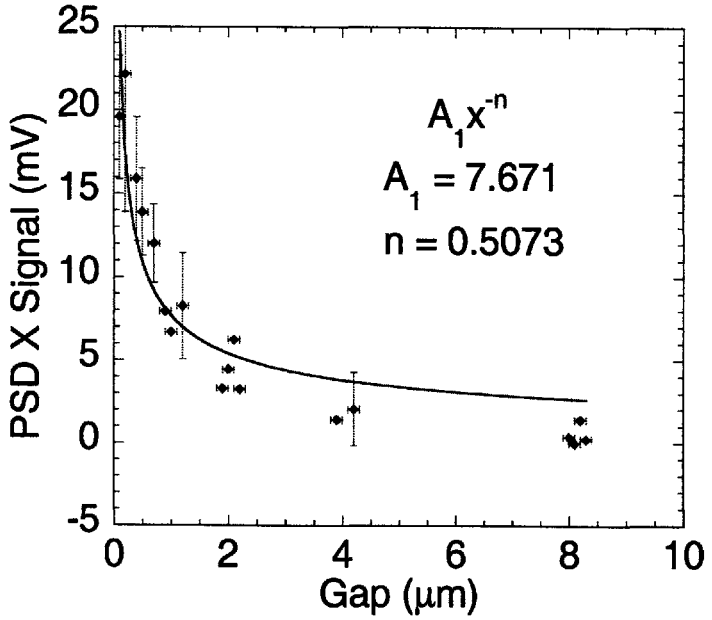

Figure 5-16: Average data from 5 different heat transfer-distance curves

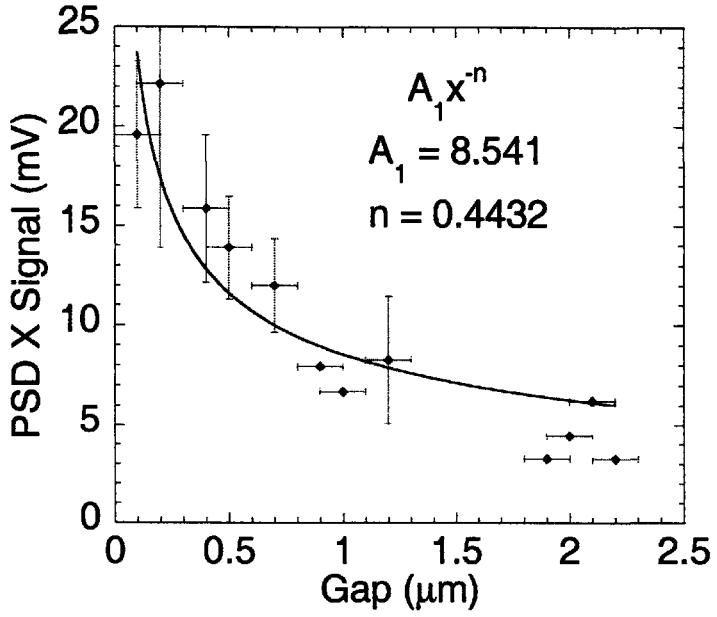

Figure 5-17: The data shown in Fig. 5-16 but truncated to 2 μm gaps.

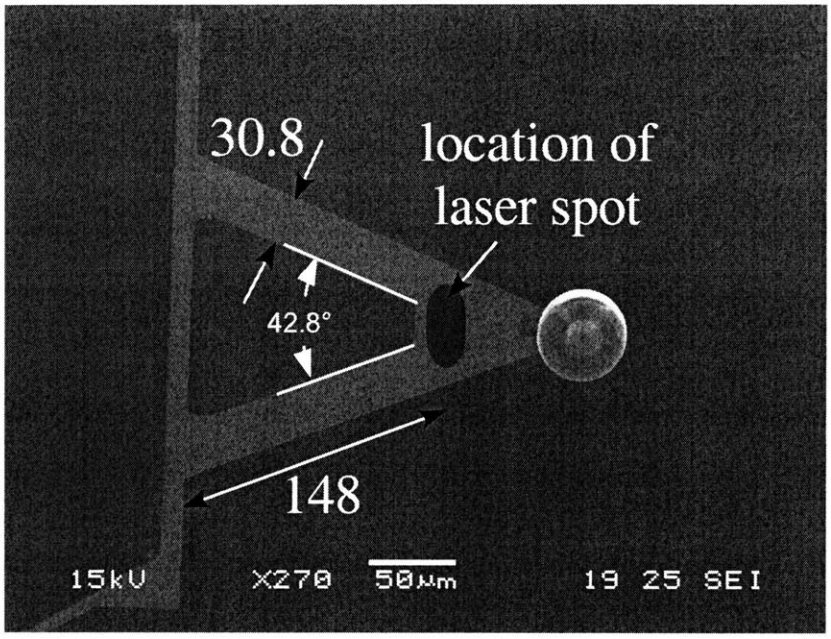

Figure 5-18: Close up view of a bi-material cantilever with dimensions in microns. The location of the laser spot on the cantilever is also shown. This is an approximate location.

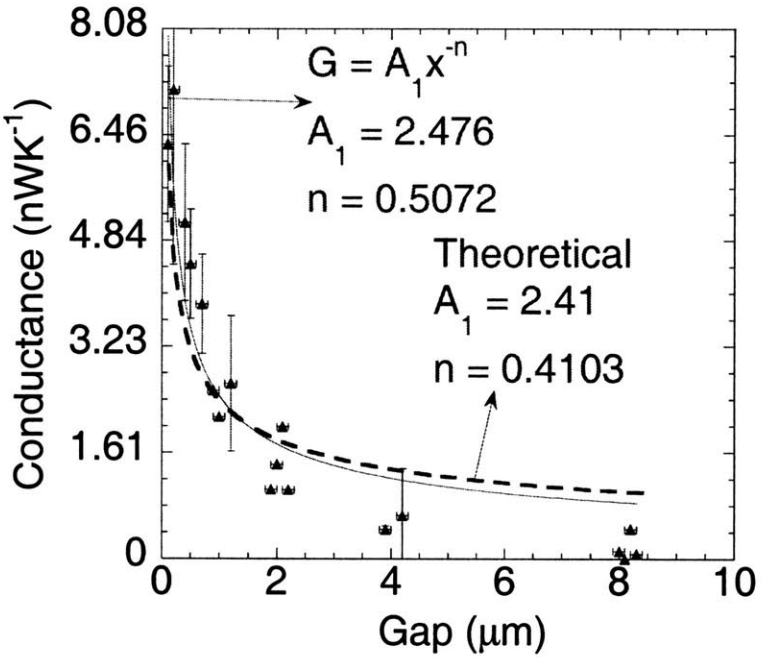

Figure 5-19: Near-field radiative conductance with variation of gap between sphere and substrate. The continuous curve is best fit to the data. The dotted curve is a theoretical estimate of the near-field radiative conductance between a sphere and a substrate.

technique to convert the 100 nm steps of the current stage into a 10 nm steps. Though I was succesful at that, I could not perform a successful experiment with that configuration for radiation experiments. A shielded piezo stack should be a good choice.

3. Alter the apparatus so that the substrate is in a horizontal plane (like the substrate in a conventional AFM). The cantilever is still perpendicular to the substrate but is now vertical. The reason for this is that it become much easier to incorporate an microscope with the whole setup.

4. Better control for adjusting the position of the substrate. Currently everything is done manually, frequently resulting in the destruction of cantilevers (with spheres!).

5. Cleanliness of sphere and substrate. Even though care was taken to clean them as much as possible, there is at least an hour of work in ambient air before the whole apparatus is ready for the experiment. This could lead to contamination of the surface.

5.7 Similarities and differences between "force-distance" and "heat transfer-distance" curves

In the preceding sections, I have discussed some of the similarities and differences between measuring "force - distance" curve using an AFM and measuring "heat transfer-distance" curves using the current apparatus. The force - distance curve in the AFM can be measured in one of two modes - static or dynamic. Static refers to measuring the deflection of cantilever as it approaches a substrate. Dynamic method refers to measurement of shift in the resonance frequency of the cantilever as it approaches a substrate. The dynamic method is possible because the effective spring constant of the cantilever is modified by the non-linear change of force as the gap decreases. The heat transfer - distance curve measured so far corresponds to the static type of mea-

surement. It does not seem there is a corresponding dynamic method for measuring the heat transfer - distance curve. It is possible to modulate the cantilever with a separate pump beam but finally measurement of heat transfer requires measurement of an amplitude, not the shift of the resonance frequency. It will be interesting to see if heat transfer measurements can also have a dynamic method based on shift of a resonance frequency.

Chapter 6

Summary and outlook

6.1 Summary

This work in the area of nanoscale thermal radiation started with an investigation of near-field enhancement due to surface phonon polaritons and its application to thermophotovoltaic energy conversion (Section 3.4, [37]). That was followed by investigating thermal radiation in 1D periodic structures. The phased array technique was used to determine the DGF for an infinite periodic structure (Section 3.5.1, [75]). Based on this work 1D periodic metallo-dielectric structures are proposed as selective emitters that mimic the performance of more complicated 2D or 3D structures (Section 3.5.2, [53]).

Attempts to experimentally validate the near-field enhancement effect using parallel surfaces proved to be unsuccessful due to problems cited in Chapter 5. Replacing one of the surfaces by a sphere simplifies the situation considerably. Generally sub-micron spheres are favored because they can be treated using the dipole approximation. However the radiative conductance with radiative transfer between a sub-micron sphere and a substrate is of the order of 10^{-10} WK^{-1} – at least one order of magnitude smaller that what can be measured easily. Since no rigorous model exists for near-field radiative transfer between two spheres, the two-sphere problem is solved by determining the DGF and subsequently determining the conductance with the help of the fluctuation-dissipation theorem. Though scattering by two spheres

has been discussed extensively in literature, one area that has not been is the near-field interaction between them. Generally, the quantity of interest has been far-field scattering parameters. A new convergence criterion for the two-sphere problem is proposed based on analogy with work in near-field radiation problems between parallel surfaces. This criterion has been verified by subsequent numerical results. A new regime map for the validity of various theories is also proposed.

Even with the extension of the theoretical work to the two-sphere problem, it remains a question as to the best way to test this experimentally. After elimination of other techniques of measurement (scanning thermal microscopy based on Wollaston wire type sensors, scanning thermocouple microscopy), the bi-material sensor was chosen as it is one of the most sensitive temperature sensors. By attaching a sphere to an AFM cantilever, it has been possible to measure heat transfer between a sphere and a substrate to obtain "heat transfer-distance" curves. This is the first time the concept of "heat transfer-distance" curves has been discussed in literature. Using this technique it has been possible to measure near-field radiative transfer vs. gap curves for heat transfer between the sphere and a substrate. The quantitative value and trend obtained are in agreement with theory.

6.2 Possible extentions of this work

Though the formulation of the two-sphere problem is complete, computational restraints impose a limit on the maximum radius to gap ratio that can be investigated. White it is possible to utilize larger computational resouces to solve the problem, it seems like there should be a more elegant way of approaching the the limit of small gaps. This will also be of great use to the experimentalist since it should provide a route for better prediction for near-field interaction between a sphere and a flat plate, the configuration that is closer to that used in the experiment.

Though dispersion forces like Van der Waals and Casimir forces have their origin in fluctuational electrodynamics, just as thermal radiative transfer, the area of measuring molecular forces between objects is a much more mature field of study.

By comparison, the area of near-field thermal radiation is quite young. I hope that the work on the two-sphere problem and the subsequent development of the experimental technique to measure the small radiative transfer involved will go some way in addressing that situation. The experimental apparatus discussed here can be improved in the future to build a device capable of measuring extremely small radiative transfers - much like what the surface force apparatus in measurement of forces [118].

Appendix A

Scalar and vector spherical harmonics

A.1 Spherical Harmonics

Given below are a collection of formulae related to scalar and vector spherical harmonics I found useful when formulating the two-sphere problem. While I have not given references for any of the equations, I found the following references very useful [43, 98, 119, 120].

$$Y_{lm}(\theta,\phi) = \sqrt{\frac{2l+1}{4\pi}\frac{(l-m)!}{(l+m)!}}P_l^m(\cos\theta)e^{im\phi} \tag{A.1}$$

$$\frac{\partial P_l^m}{\partial\theta} = \frac{m\cos\theta}{\sin\theta}P_l^m(\cos\theta) - P_l^{m+1}(\cos\theta) \tag{A.2}$$

$$\frac{\partial Y_{lm}}{\partial\theta} = \frac{m\cos\theta}{\sin\theta}Y_{lm} - \sqrt{(l-m)(l+m+1)}e^{-i\phi}Y_{l,(m+1)} \tag{A.3}$$

$$\Rightarrow \frac{\partial Y_{lm}^*}{\partial\theta} = \frac{m\cos\theta}{\sin\theta}Y_{lm}^* - \sqrt{(l-m)(l+m+1)}e^{i\phi}Y_{l,(m+1)}^* \tag{A.4}$$

$$\Rightarrow \frac{\partial Y_{l,-m}}{\partial\theta} = \frac{m\cos\theta}{\sin\theta}Y_{l,-m} + \sqrt{(l-m)(l+m+1)}e^{i\phi}Y_{l,-(m+1)} \tag{A.5}$$

$$\int_{-1}^{1} dx P_{l_1}^{m}(x) P_{l_2}^{m}(x) dx = \frac{2}{2l+1} \frac{(l+m)!}{(l-m)!} \delta_{l_1 l_2} \tag{A.6}$$

$$\int_{-1}^{1} P_{l}^{m_1}(x) P_{l}^{m_2}(x) \frac{1}{1-x^2} dx = \frac{1}{m} \frac{(l+m)!}{(l-m)!} \delta_{m_1 m_2} \tag{A.7}$$

$$P_{l}^{-m} = (-1)^m \frac{(l-m)!}{(l+m)!} P_{l}^{m} \tag{A.8}$$

$$\frac{im}{\sin\theta} \left(Y_{lm} \frac{\partial Y_{l,-m}}{\partial \theta} + \frac{\partial Y_{lm}}{\partial \theta} Y_{l,-m} \right) = \frac{im}{\sin\theta} \frac{\partial}{\partial \theta} \left(Y_{lm} Y_{l,-m} \right) \tag{A.9}$$

$$\sum_{m=-l}^{l} \frac{im}{\sin\theta} \frac{\partial}{\partial \theta} \left(Y_{lm} Y_{l,-m} \right) = 0 \text{ (the + and - values of m cancel each other)} \tag{A.10}$$

$$\sum_{m=-l}^{l} (-1)^m \left(Y_{lm} Y_{l,-m} \right) = \frac{2l+1}{4\pi} \tag{A.11}$$

$$\frac{1}{l(l+1)} \sum_{m=-l}^{l} (-1)^m \left(\frac{\partial Y_{lm}}{\partial \theta} \frac{\partial Y_{l,-m}}{\partial \theta} + \frac{m^2}{\sin^2\theta} Y_{lm} Y_{l,-m} \right) = \frac{2l+1}{4\pi} \tag{A.12}$$

$$\frac{\partial Y_{\beta m}}{\partial \theta} \frac{\partial Y_{l,-m}}{\partial \theta} + \frac{m^2}{\sin^2\theta} Y_{\beta m} Y_{l,-m} = \frac{\partial Y_{\beta m}}{\partial \theta} \frac{\partial Y_{l,-m}}{\partial \theta} + m^2 \frac{\cos^2\theta}{\sin^2\theta} Y_{\beta m} Y_{l,-m} + m^2 Y_{\beta m} Y_{l,-m} \tag{A.13}$$

$$\frac{\partial Y_{\beta m}}{\partial \theta} \frac{\partial Y_{l,-m}}{\partial \theta} + m^2 \frac{\cos^2\theta}{\sin^2\theta} Y_{\beta m} Y_{l,-m} = \left(\frac{\partial Y_{\beta m}}{\partial \theta} - m \frac{\cos\theta}{\sin\theta} Y_{\beta m} \right) \left(\frac{\partial Y_{l,-m}}{\partial \theta} - m \frac{\cos\theta}{\sin\theta} Y_{l,-m} \right) + m \frac{\cos\theta}{\sin\theta} \left(\frac{\partial Y_{\beta m}}{\partial \theta} Y_{l,-m} + Y_{\beta m} \frac{\partial Y_{l,-m}}{\partial \theta} \right) \tag{A.14}$$

$$\left(\frac{\partial Y_{\beta m}}{\partial\theta} - m\frac{\cos\theta}{\sin\theta}Y_{\beta m}\right) = -\sqrt{(\beta-m)(\beta+m+1)}e^{-i\phi}Y_{\beta,(m+1)} \tag{A.15}$$

$$\left(\frac{\partial Y_{l,-m}}{\partial\theta} - m\frac{\cos\theta}{\sin\theta}Y_{l,-m}\right) = +\sqrt{(l-m)(l+m+1)}e^{i\phi}Y_{l,-(m+1)} \tag{A.16}$$

$$\int d\Omega Y_{\beta,m}(\theta,\phi)\cos\theta Y_{l,-m}(\theta,\phi) =$$
$$= (-1)^m\left[\delta_{\beta,l+1}\sqrt{\frac{(l+m+1)(l-m+1)}{(2l+1)(2l+3)}} + \delta_{\beta,l-1}\sqrt{\frac{(l+m)(l-m)}{(2l-1)(2l+1)}}\right] \tag{A.17}$$

$$\int d\Omega Y_{\beta,m+1}(\theta,\phi)\sin\theta e^{-i\phi}Y_{l,-m}(\theta,\phi) =$$
$$= (-1)^{m+1}\left[\delta_{\beta,l+1}\sqrt{\frac{(l+m+1)(l+m+2)}{(2l+1)(2l+3)}} - \delta_{\beta,l-1}\sqrt{\frac{(l-m)(l-m-1)}{(2l-1)(2l+1)}}\right] \tag{A.18}$$

$$\int d\Omega Y_{\beta,m}(\theta,\phi)\sin\theta e^{i\phi}Y_{l,-(m+1)}(\theta,\phi) =$$
$$= (-1)^{m+1}\left[\delta_{\beta,l+1}\sqrt{\frac{(l-m)(l-m+1)}{(2l+1)(2l+3)}} - \delta_{\beta,l-1}\sqrt{\frac{(l+m+1)(l+m)}{(2l-1)(2l+1)}}\right] \tag{A.19}$$

$$m\frac{\cos\theta}{\sin\theta}\left(\frac{\partial Y_{\beta m}}{\partial\theta}Y_{l,-m} + Y_{\beta m}\frac{\partial Y_{l,-m}}{\partial\theta}\right) = m\cot\theta\frac{\partial}{\partial\theta}\left(Y_{\beta m}Y_{l,-m}\right) \tag{A.20}$$

$$
\begin{aligned}
L_2 &= m\int d\Omega \frac{\cos^2\theta}{\sin\theta}\frac{\partial}{\partial\theta}\left(Y_{\beta m}Y_{l,-m}\right) = m\int d\theta\cos^2\theta\frac{\partial}{\partial\theta}\left(Y_{\beta m}Y_{l,-m}\right) \\
&= 2m\pi\int_0^\pi d\theta\left[\frac{\partial}{\partial\theta}\left(\cos^2\theta Y_{\beta m}Y_{l,-m}\right)+2\sin\theta\cos\theta\left(Y_{\beta m}Y_{l,-m}\right)\right] \\
&= 2m\int d\Omega\cos\theta\left(Y_{\beta m}Y_{l,-m}\right) = 2m\sqrt{\frac{4\pi}{3}}\int d\Omega Y_{1,0}Y_{\beta m}Y_{l,-m} \\
&= (-1)^m 2m\left[\delta_{\beta,l+1}\sqrt{\frac{(l+1)^2-m^2}{(2l+1)(2l+3)}}+\delta_{\beta,l-1}\sqrt{\frac{l^2-m^2}{(2l-1)(2l+1)}}\right]
\end{aligned}
\tag{A.21}
$$

$$
\begin{aligned}
L_1 &= \int d\Omega\cos\theta\left(\frac{\partial Y_{\beta m}}{\partial\theta}-m\frac{\cos\theta}{\sin\theta}Y_{\beta m}\right)\left(\frac{\partial Y_{l,-m}}{\partial\theta}-m\frac{\cos\theta}{\sin\theta}Y_{l,-m}\right) \\
&= -\sqrt{(\beta-m)(\beta+m+1)}\sqrt{(l-m)(l+m+1)}\int d\Omega\cos\theta Y_{\beta,(m+1)}Y_{l,-(m+1)} \\
&= (-1)^m\sqrt{(\beta-m)(\beta+m+1)}\sqrt{(l-m)(l+m+1)}\times \\
&\left[\delta_{\beta,l+1}\sqrt{\frac{(l+m+2)(l-m)}{(2l+1)(2l+3)}}+\delta_{\beta,l-1}\sqrt{\frac{(l+m+1)(l-m-1)}{(2l-1)(2l+1)}}\right] \\
&= (-1)^m\left[\delta_{\beta,l+1}\frac{((l+1)^2-(m+1)^2)\sqrt{(l+1)^2-m^2}}{\sqrt{(2l+1)(2l+3)}}+\delta_{\beta,l-1}\frac{(l^2-(m+1)^2)\sqrt{l^2-m^2}}{\sqrt{(2l-1)(2l+1)}}\right]
\end{aligned}
\tag{A.22}
$$

$$
\begin{aligned}
L_3 &= (-1)^m\int d\Omega m^2\cos\theta Y_{\beta m}Y_{l,-m} \\
&= m^2\left[\delta_{\beta,l+1}\sqrt{\frac{(l+m+1)(l-m+1)}{(2l+1)(2l+3)}}+\delta_{\beta,l-1}\sqrt{\frac{(l+m)(l-m)}{(2l-1)(2l+1)}}\right]
\end{aligned}
\tag{A.23}
$$

$$
L_2+L_3 = (-1)^m[(m+1)^2-1]\left[\delta_{\beta,l+1}\sqrt{\frac{(l+m+1)(l-m+1)}{(2l+1)(2l+3)}}+\delta_{\beta,l-1}\sqrt{\frac{(l+m)(l-m)}{(2l-1)(2l+1)}}\right]
\tag{A.24}
$$

$$L_1 + L_2 + L_3 = \int d\Omega \cos\theta \left(\frac{\partial Y_{\beta m}}{\partial \theta} \frac{\partial Y_{l,-m}}{\partial \theta} + \frac{m^2}{\sin^2\theta} Y_{\beta m} Y_{l,-m} \right)$$
$$= (-1)^m \left[\delta_{\beta,l+1} \frac{((l+1)^2 - 1)\sqrt{(l+1)^2 - m^2}}{\sqrt{(2l+1)(2l+3)}} + \delta_{\beta,l-1} \frac{(l^2-1)\sqrt{l^2-m^2}}{\sqrt{(2l-1)(2l+1)}} \right] \tag{A.25}$$

$$m \int d\Omega \frac{\cos\theta}{\sin\theta} \frac{\partial}{\partial\theta} \left(Y_{\beta m} Y_{l,-m} \right) = m \int d\phi d\theta \left[\frac{\partial}{\partial\theta} \left(\cos\theta Y_{\beta m} Y_{l,-m} \right) + \sin\theta Y_{\beta m} Y_{l,-m} \right]$$
$$= 2\pi m \left[\cos\theta Y_{\beta m} Y_{l,-m} \right] \Big|_0^{2\pi} + m \int d\Omega \left(Y_{\beta m} Y_{l,-m} \right)$$
$$= (-1)^m m \delta_{\beta l} \tag{A.26}$$

$$\frac{m}{\sqrt{l(l+1)\beta(\beta+1)}} \int d\Omega \cos\theta \frac{\partial}{\partial\theta} \left(Y_{\beta m} Y_{l,-m} \right) = (-1)^m \frac{m}{l(l+1)} \delta_{\beta l} \tag{A.27}$$

$$\int d\Omega \sin\theta \frac{\partial Y_{\beta m}}{\partial\theta} Y_{l,-m} =$$
$$= \int d\Omega \sin\theta \left(\frac{m\cos\theta}{\sin\theta} Y_{\beta m} - \sqrt{(\beta - m)(\beta + m + 1)} e^{-i\phi} Y_{\beta,(m+1)} \right) Y_{l,-m}$$
$$= \int d\Omega \left(m\cos\theta Y_{\beta m} - \sqrt{(\beta - m)(\beta + m + 1)} \sin\theta e^{-i\phi} Y_{\beta,(m+1)} \right) Y_{l,-m}$$
$$= (-1)^m \left[\delta_{\beta,l+1} (2m + l + 2) \sqrt{\frac{(l+1)^2 - m^2}{(2l+3)(2l+1)}} + \delta_{\beta,l-1} (2m - l + 1) \sqrt{\frac{l^2 - m^2}{(2l+1)(2l-1)}} \right] \tag{A.28}$$

A.2 Vector spherical harmonics

$$\boldsymbol{V}_{lm}^{(1)} = \hat{r} Y_{lm}(\theta,\phi) \tag{A.29}$$

$$\begin{aligned} \boldsymbol{V}_{lm}^{(2)} &= \frac{\boldsymbol{\nabla}\times\boldsymbol{r}Y_{lm}(\theta,\phi)}{\sqrt{l(l+1)}} = -\frac{\boldsymbol{r}\times\boldsymbol{\nabla}Y_{lm}(\theta,\phi)}{\sqrt{l(l+1)}} \\ &= \frac{1}{\sqrt{l(l+1)}}\left(\hat{\theta}\frac{im}{\sin\theta}Y_{lm} - \hat{\phi}\frac{\partial Y_{lm}}{\partial\theta}\right) \end{aligned} \tag{A.30}$$

$$\begin{aligned} \boldsymbol{V}_{lm}^{(3)} &= \frac{r\boldsymbol{\nabla}Y_{lm}(\theta,\phi)}{\sqrt{l(l+1)}} \\ &= \frac{1}{\sqrt{l(l+1)}}\left(\hat{\phi}\frac{im}{\sin\theta}Y_{lm} + \hat{\theta}\frac{\partial Y_{lm}}{\partial\theta}\right) \end{aligned} \tag{A.31}$$

$$Tr\left(\boldsymbol{V}_{\beta m}^{(2)}\boldsymbol{V}_{l,-m}^{(2)}\right) = \frac{(-1)^m}{\sqrt{\beta(\beta+1)l(l+1)}}\left(\frac{\partial Y_{\beta m}}{\partial\theta}\frac{\partial Y_{l,-m}}{\partial\theta} + \frac{m^2}{\sin^2\theta}Y_{\beta m}Y_{l,-m}\right) \tag{A.32}$$

$$Tr\left(\boldsymbol{V}_{\beta m}^{(3)}\boldsymbol{V}_{l,-m}^{(3)}\right) = \frac{(-1)^m}{\sqrt{\beta(\beta+1)l(l+1)}}\left(\frac{\partial Y_{\beta m}}{\partial\theta}\frac{\partial Y_{l,-m}}{\partial\theta} + \frac{m^2}{\sin^2\theta}Y_{\beta m}Y_{l,-m}\right) \tag{A.33}$$

$$Tr\left(\boldsymbol{V}_{\beta m}^{(2)}\boldsymbol{V}_{l,-m}^{(3)}\right) = \frac{(-1)^m}{\sqrt{\beta(\beta+1)l(l+1)}}\left(\frac{im}{\sin\theta}\right)\frac{\partial}{\partial\theta}\left(Y_{\beta m}Y_{l,-m}\right) \tag{A.34}$$

$$Tr\left(\boldsymbol{V}_{\beta m}^{(3)}\boldsymbol{V}_{l,-m}^{(2)}\right) = -\frac{(-1)^m}{\sqrt{\beta(\beta+1)l(l+1)}}\left(\frac{im}{\sin\theta}\right)\frac{\partial}{\partial\theta}\left(Y_{\beta m}Y_{l,-m}\right) \tag{A.35}$$

$$Tr\left(\boldsymbol{V}_{\beta m}^{(1)}\boldsymbol{V}_{l,-m}^{(1)}\right) = (-1)^m Y_{\beta m}Y_{l,-m} \tag{A.36}$$

$$\left(\boldsymbol{V}_{\beta m}^{(2)}\boldsymbol{V}_{l,-m}^{(1)}\right)_{\hat{\theta}\hat{r}} = \frac{(-1)^m}{\sqrt{\beta(\beta+1)}}\left(\frac{im}{\sin\theta}\right)Y_{\beta m}Y_{l,-m} \tag{A.37}$$

$$\left(\boldsymbol{V}_{\beta m}^{(3)}\boldsymbol{V}_{l,-m}^{(1)}\right)_{\hat{\theta}\hat{r}} = \frac{(-1)^m}{\sqrt{\beta(\beta+1)}}\frac{\partial Y_{\beta m}}{\partial\theta}Y_{l,-m} \tag{A.38}$$

$$\begin{aligned} \int d\Omega\cos\theta Tr\left(\boldsymbol{V}_{\beta m}^{(1)}\boldsymbol{V}_{l,-m}^{(1)}\right) &= \int d\Omega\cos\theta Y_{\beta m}Y_{l,-m} \\ &= (-1)^m\left[\delta_{\beta,l+1}\sqrt{\frac{(l+1)^2-m^2}{(2l+1)(2l+3)}} + \delta_{\beta,l-1}\sqrt{\frac{l^2-m^2}{(2l-1)(2l+1)}}\right] \end{aligned} \tag{A.39}$$

$$\int d\Omega \cos\theta Tr\left(\boldsymbol{V}^{(2)}_{\beta m}\boldsymbol{V}^{(2)}_{l,-m}\right) = \frac{1}{\sqrt{\beta(\beta+1)l(l+1)}}\int d\Omega\cos\theta\left(\frac{\partial Y_{\beta m}}{\partial\theta}\frac{\partial Y_{l,-m}}{\partial\theta}+\frac{m^2}{\sin^2\theta}Y_{\beta m}Y_{l,-m}\right)$$
$$= (-1)^m\left[\delta_{\beta,l+1}\frac{\sqrt{l(l+2)}}{l+1}\sqrt{\frac{(l+1)^2-m^2}{(2l+1)(2l+3)}}+\delta_{\beta,l-1}\frac{\sqrt{l^2-1}}{l}\sqrt{\frac{l^2-m^2}{(2l-1)(2l+1)}}\right]$$
$$= \int d\Omega\cos\theta Tr\left(\boldsymbol{V}^{(3)}_{\beta m}\boldsymbol{V}^{(3)}_{l,-m}\right) \tag{A.40}$$

$$\int d\Omega\cos\theta Tr\left(\boldsymbol{V}^{(2)}_{\beta m}\boldsymbol{V}^{(3)}_{l,-m}\right) = \frac{im}{\sqrt{\beta(\beta+1)l(l+1)}}\int d\Omega\cos\theta\frac{\partial}{\partial\theta}\left(Y_{\beta m}Y_{l,-m}\right)$$
$$= (-1)^m\frac{m}{l(l+1)}\delta_{\beta l} \tag{A.41}$$

$$\int d\Omega\sin\theta\left(\boldsymbol{V}^{(2)}_{\beta m}\boldsymbol{V}^{(1)}_{l,-m}\right)_{\hat{\theta}\hat{r}} = (-1)^m\frac{im}{\sqrt{\beta(\beta+1)}}\int d\Omega Y_{\beta m}Y_{l,-m}$$
$$= (-1)^m\frac{im}{\sqrt{l(l+1)}}\delta_{l\beta} \tag{A.42}$$

$$\int d\Omega\sin\theta\left(\boldsymbol{V}^{(3)}_{\beta m}\boldsymbol{V}^{(1)}_{l,-m}\right)_{\hat{\theta}\hat{r}} =$$
$$= (-1)^m\left[\delta_{\beta,l+1}\frac{(2m+l+2)}{\sqrt{(l+1)(l+2)}}\sqrt{\frac{(l+1)^2-m^2}{(2l+3)(2l+1)}}+\delta_{\beta,l-1}\frac{(2m-l+1)}{\sqrt{l(l-1)}}\sqrt{\frac{l^2-m^2}{(2l+1)(2l-1)}}\right] \tag{A.43}$$

$$\int d\Omega\sin\theta\left(\boldsymbol{V}^{(3)}_{\beta m}\boldsymbol{V}^{(1)}_{l,-m}\right)_{\hat{\theta}\hat{r}} =$$
$$= (-1)^m\left[\delta_{\beta,l+1}\sqrt{\frac{l+2}{l+1}}\sqrt{\frac{(l+1)^2-m^2}{(2l+3)(2l+1)}}-\delta_{\beta,l-1}\sqrt{\frac{l-1}{l}}\sqrt{\frac{l^2-m^2}{(2l+1)(2l-1)}}\right] \tag{A.44}$$

$$\sqrt{l(l+1)}\int d\Omega\sin\theta\left(\boldsymbol{V}^{(3)}_{\beta m}\boldsymbol{V}^{(1)}_{l,-m}\right)_{\hat{\theta}\hat{r}} =$$
$$= (-1)^m\left[\delta_{\beta,l+1}\sqrt{l(l+2)}\sqrt{\frac{(l+1)^2-m^2}{(2l+3)(2l+1)}}-\delta_{\beta,l-1}\sqrt{l^2-1}\sqrt{\frac{l^2-m^2}{(2l+1)(2l-1)}}\right] \tag{A.45}$$

$$\oint_{\Omega} \left(\boldsymbol{V}_{lm}^{(s)}(\theta,\phi) \times \boldsymbol{V}_{pq}^{(s)*}(\theta,\phi) \right) \cdot \hat{\boldsymbol{r}} d\Omega = 0 \tag{A.46}$$

$$\oint_{\Omega} \left(\boldsymbol{V}_{lm}^{(2)}(\theta,\phi) \times \boldsymbol{V}_{pq}^{(3)*}(\theta,\phi) \right) \cdot \hat{\boldsymbol{r}} d\Omega = \delta_{lp}\delta_{mq} \tag{A.47}$$

$$\oint_{\Omega} \left(\boldsymbol{V}_{lm}^{(3)}(\theta,\phi) \times \boldsymbol{V}_{pq}^{(2)*}(\theta,\phi) \right) \cdot \hat{\boldsymbol{r}} d\Omega = -\delta_{lp}\delta_{mq} \tag{A.48}$$

$$\begin{aligned} k_f^2 \epsilon_a'' \int_{V_a} \boldsymbol{M}_{lm}^{(1)}(k_a \boldsymbol{r}_a') \cdot \boldsymbol{M}_{pq}^{(1)*}(k_a \boldsymbol{r}_a') d\boldsymbol{r}' \; &= \\ \delta_{lp}\delta_{mq} a \Im\left(k_a^* a z_l^{(1)}(k_a a) \zeta_l^{(1)*}(k_a a) \right) & \end{aligned} \tag{A.49}$$

$$\begin{aligned} k_f^2 \epsilon_a'' \int_{V_a} \boldsymbol{N}_{lm}^{(1)}(k_a \boldsymbol{r}_a') \cdot \boldsymbol{N}_{pq}^{(1)*}(k_a \boldsymbol{r}_a') d\boldsymbol{r}' \; &= \\ \delta_{lp}\delta_{mq} a \Im\left(k_a^* a z_l^{(1)*}(k_a a) \zeta_l^{(1)}(k_a a) \right) & \end{aligned} \tag{A.50}$$

Appendix B

Mathematica code for the solution to the two-sphere problem

```
<< LinearAlgebra`MatrixManipulation`
ElecCharge = 1.602*10^(-19);
PlanckBy2Pi = 1.0546*10^(-34);
kBoltz = 1.38*10^(-23);
LightVel = 3.0*10^8;
T = 300;

wmin = 0.06; (* minimum frequency in eV*)
wmax = 0.07; (* maximum frequency in eV*)
wlo = 0.12; (*longitudinal optical freq*)
wto = 0.098; (*longitudinal optical freq*)
gam = 5.88*10^(-3); (*damping*)
epsinf = 6.7;

(*w = Table[wmin + (r - 1)*(wmax - wmin)/(Nfreq - 1), {r, 1, Nfreq}];*)
(*dielecfn = epsinf*(wlo^2 - w^2 - I*gam*w)/(wto^2 - w^2 - I*gam*w);
refind = Sqrt[dielecfn];*)
```

```
Nfreq = 100;
Nfreq1 = 45;
Nfreq2 = 45;
resfreq1 = 0.061;
resfreq2 = 0.144;
freqBW = 0.04;
w1 = Table[resfreq1-freqBW/2+(r-1)*freqBW/(Nfreq1-1),{r,1,Nfreq1}];
w3 = Table[resfreq2-freqBW/2+(r-1)*freqBW/(Nfreq2-1),{r,1,Nfreq2}];
w2 = Table[w1[[Nfreq1]]+r*(w3[[1]]-w1[[Nfreq1]])/(Nfreq-Nfreq1-Nfreq2+1),
{r,1,Nfreq-Nfreq1-Nfreq2}];

w = Join[w1,w2,w3];
freqinterval = Table[0,{r,1,Nfreq-1}];
freqinterval = Table[w[[r]],{r,2,Nfreq}]-Table[w[[r]],{r,1,Nfreq-1}];


refinddata = Import["SiliconDioxideAmorphousIRRefInd.dat"];

SpecConductance12 = Table[0, {r, 1, Nfreq}];
SpecConductance21 = Table[0, {r, 1, Nfreq}];

(*a = 25000.0*10^(-9);
 b = 50.0*10^(-9);
 d = 100.0*10^(-9);*)

<<inputfile.txt

d = d + (a + b);

(*w[[1]] = 0.061;*)
```

```
For[s = 1, s < Max[2, Nfreq + 1],
  FreqEv = w[[s]];
  FreqRad = FreqEv*ElecCharge/PlanckBy2Pi;

  freqlist = refinddata[[All,1]];
  freqpos1 = Last[Position[Negative[freqlist-FreqEv],False]][[1]];
  freqpos2 = First[Position[Negative[freqlist-FreqEv],True]][[1]];
  RefIndA \
=((freqlist[[freqpos1]]-FreqEv)*(refinddata[[freqpos2,2]]+I*refinddata[[\
freqpos2,3]])+(-freqlist[[freqpos2]]+FreqEv)*(refinddata[[freqpos1,2]]+I*\
refinddata[[freqpos1,3]]))/(freqlist[[freqpos1]]-freqlist[[freqpos2]]);

  (*RefIndA = 1.0*refind[[s]];
  RefIndB = 1.0*refind[[s]];*)
  RefIndB = RefIndA;
  RefIndVac = 1.0;

  ka = (FreqRad/LightVel)*a;
  kb = (FreqRad/LightVel)*b;
  kd = (FreqRad/LightVel)*d;
  kta = (kBoltz*T/(PlanckBy2Pi*LightVel))*a;

  PowerIndicator = 1;

  conductive = 0;
  Nmax = Ceiling[3*(1 + Abs[kd])/2.0] + delNmax;

  (*Nmax = 200;*)
  Tmatrix = Table[0, {2*Nmax + 3}, {2*Nmax + 3}];
```

```
  PowerMatrix12 =
    ZeroMatrix[Nmax + 1,
      Nmax]; (*This will contail final flux vales. Almost half wilcat 1 be \
empty*)


  PowerMatrix21 = ZeroMatrix[Nmax + 1, Nmax];

  (*Evaluating various Bessel's functions for further calculations.
        Begins here*)
  BesRicJArrayka = Table[0, {n, 1, Nmax + 1}];
  BesRicYArrayka = Table[0, {n, 1, Nmax + 1}];
  BesRicJArraykb = Table[0, {n, 1, Nmax + 1}];
  BesRicYArraykb = Table[0, {n, 1, Nmax + 1}];
  BesRicJArraykAa = Table[0, {n, 1, Nmax + 1}];
  BesRicYArraykAa = Table[0, {n, 1, Nmax + 1}];
  BesRicJArraykBb = Table[0, {n, 1, Nmax + 1}];
  BesRicYArraykBb = Table[0, {n, 1, Nmax + 1}];


  (*For input argument ka. These are all for kfa and kfb.
        Need to compute separate bessel function for the reflection \
\
coefficients*)
  BesselJArrayka = Sqrt[Pi/2.0/ka]*Table[BesselJ[n + 0.5, ka], {n, 0, Nmax}];
  BesselYArrayka = Sqrt[Pi/2.0/ka]*Table[BesselY[n + 0.5, ka], {n, 0, Nmax}];
  BesselHArrayka = BesselJArrayka + I*BesselYArrayka;
  BesRicJArrayka[[Table[n, {n, 2, Nmax + 1}]]] =
    BesselJArrayka[[Table[n, {n, 1, Nmax}]]] -
      Table[n, {n, 1, Nmax}]/ka*BesselJArrayka[[Table[n, {n, 2, Nmax + 1}]]];
```

```
BesRicYArrayka[[Table[n, {n, 2, Nmax + 1}]]] =
  BesselYArrayka[[Table[n, {n, 1, Nmax}]]] -
    Table[n, {n, 1, Nmax}]/ka*BesselYArrayka[[Table[n, {n, 2, Nmax + 1}]]];
BesRicJArrayka[[1]] = Sqrt[Pi/2.0/ka]*BesselJ[-1 + 0.5, ka];
BesRicYArrayka[[1]] = Sqrt[Pi/2.0/ka]*BesselY[-1 + 0.5, ka];
BesRicHArrayka = BesRicJArrayka + I*BesRicYArrayka;

(*For input argument kb*)
BesselJArraykb = Sqrt[Pi/2.0/kb]*Table[BesselJ[n + 0.5, kb], {n, 0, Nmax}];
BesselYArraykb = Sqrt[Pi/2.0/kb]*Table[BesselY[n + 0.5, kb], {n, 0, Nmax}];
BesselHArraykb = BesselJArraykb + I*BesselYArraykb;
BesRicJArraykb[[Table[n, {n, 2, Nmax + 1}]]] =
  BesselJArraykb[[Table[n, {n, 1, Nmax}]]] -
    Table[n, {n, 1, Nmax}]/kb*BesselJArraykb[[Table[n, {n, 2, Nmax + 1}]]];
BesRicYArraykb[[Table[n, {n, 2, Nmax + 1}]]] =
  BesselYArraykb[[Table[n, {n, 1, Nmax}]]] -
    Table[n, {n, 1, Nmax}]/kb*BesselYArraykb[[Table[n, {n, 2, Nmax + 1}]]];
BesRicJArraykb[[1]] = Sqrt[Pi/2.0/kb]*BesselJ[-1 + 0.5, kb];
BesRicYArraykb[[1]] = Sqrt[Pi/2.0/kb]*BesselY[-1 + 0.5, kb];
BesRicHArraykb = BesRicJArraykb + I*BesRicYArraykb;

(*Computing Bessel's functions for complex arguments.*)
BesselJArraykAa =
  Sqrt[Pi/2.0/(ka*RefIndA)]*
    Table[BesselJ[n + 0.5, ka*RefIndA], {n, 0, Nmax}];
BesselYArraykAa =
  Sqrt[Pi/2.0/(ka*RefIndA)]*
    Table[BesselY[n + 0.5, ka*RefIndA], {n, 0, Nmax}];
BesselHArraykAa = BesselJArraykAa + I*BesselYArraykAa;
BesRicJArraykAa[[Table[n, {n, 2, Nmax + 1}]]] =
```

```
  BesselJArraykAa[[Table[n, {n, 1, Nmax}]]] -
    Table[n, {n, 1, Nmax}]/(ka*RefIndA)*
      BesselJArraykAa[[Table[n, {n, 2, Nmax + 1}]]];
BesRicYArraykAa[[Table[n, {n, 2, Nmax + 1}]]] =
  BesselYArraykAa[[Table[n, {n, 1, Nmax}]]] -
    Table[n, {n, 1, Nmax}]/(ka*RefIndA)*
      BesselYArraykAa[[Table[n, {n, 2, Nmax + 1}]]];
BesRicJArraykAa[[1]] =
  Sqrt[Pi/2.0/(ka*RefIndA)]*BesselJ[-1 + 0.5, ka*RefIndA];
BesRicYArraykAa[[1]] =
  Sqrt[Pi/2.0/(ka*RefIndA)]*BesselY[-1 + 0.5, ka*RefIndA];
BesRicHArraykAa = BesRicJArraykAa + I*BesRicYArraykAa;
(*Completed for complex input argument ka*RefIndA*)

(*For input argument complex kb*RefIndB*)
BesselJArraykBb =
  Sqrt[Pi/2.0/(RefIndB*kb)]*
    Table[BesselJ[n + 0.5, RefIndB*kb], {n, 0, Nmax}];
BesselYArraykBb =
  Sqrt[Pi/2.0/(RefIndB*kb)]*
    Table[BesselY[n + 0.5, RefIndB*kb], {n, 0, Nmax}];
BesselHArraykBb = BesselJArraykBb + I*BesselYArraykBb;
BesRicJArraykBb[[Table[n, {n, 2, Nmax + 1}]]] =
  BesselJArraykBb[[Table[n, {n, 1, Nmax}]]] -
    Table[n, {n, 1, Nmax}]/(RefIndB*kb)*
      BesselJArraykBb[[Table[n, {n, 2, Nmax + 1}]]];
BesRicYArraykBb[[Table[n, {n, 2, Nmax + 1}]]] =
  BesselYArraykBb[[Table[n, {n, 1, Nmax}]]] -
    Table[n, {n, 1, Nmax}]/(RefIndB*kb)*
      BesselYArraykBb[[Table[n, {n, 2, Nmax + 1}]]];
```

```
BesRicJArraykBb[[1]] =
  Sqrt[Pi/2.0/(RefIndB*kb)]*BesselJ[-1 + 0.5, (RefIndB*kb)];
BesRicYArraykBb[[1]] =
  Sqrt[Pi/2.0/(RefIndB*kb)]*BesselY[-1 + 0.5, (RefIndB*kb)];
BesRicHArraykBb = BesRicJArraykBb + I*BesRicYArraykBb;
(*Completed for complex input argument kb*RefIndB*)

(*For input argument kd*)
BesselJArraykd =
  Sqrt[Pi/2.0/kd]*Table[BesselJ[n + 0.5, kd], {n, 0, 2*Nmax + 2}];
BesselYArraykd =
  Sqrt[Pi/2.0/kd]*Table[BesselY[n + 0.5, kd], {n, 0, 2*Nmax + 2}];
BesselHArraykd = BesselJArraykd + I*BesselYArraykd;
(*Evaluating various Bessel's functions for further calculations.
      Ends here*)

Refl MNumA = (ka*RefIndA*BesRicJArraykAa/BesselJArraykAa -
      ka*RefIndVac*BesRicJArrayka/BesselJArrayka);
Refl MDenA = (ka*RefIndA*BesRicJArraykAa/BesselJArraykAa -
      ka*RefIndVac*BesRicHArrayka/BesselHArrayka);
Refl MNumB = (kb*RefIndB*BesRicJArraykBb/BesselJArraykBb -
      kb*RefIndVac*BesRicJArraykb/BesselJArraykb);
Refl MDenB = (kb*RefIndB*BesRicJArraykBb/BesselJArraykBb -
      kb*RefIndVac*BesRicHArraykb/BesselHArraykb);

Refl NNumA = (ka*RefIndA*BesselJArraykAa/BesRicJArraykAa -
      ka*RefIndVac*BesselJArrayka/BesRicJArrayka);
Refl NDenA = (ka*RefIndA*BesselJArraykAa/BesRicJArraykAa -
      ka*RefIndVac*BesselHArrayka/BesRicHArrayka);
Refl NNumB = (kb*RefIndB*BesselJArraykBb/BesRicJArraykBb -
```

```
      kb*RefIndVac*BesselJArraykb/BesRicJArraykb);
Refl1NDenB = (kb*RefIndB*BesselJArraykBb/BesRicJArraykBb -
      kb*RefIndVac*BesselHArraykb/BesRicHArraykb);

(**)
RhsMArray = (ka*RefIndA*BesRicJArraykAa*BesselJArrayka -
        ka*RefIndVac*BesRicJArrayka*
          BesselJArraykAa)/((ka*RefIndA*BesRicJArraykAa*BesselHArrayka -
            ka*RefIndVac*BesRicHArrayka*
              BesselJArraykAa)*(BesselJArrayka^2));
(*RhsMArray = (Refl1MNumA/Refl1MDenA)/(BesselJArrayka*BesselHArrayka);*)
(**)
RhsNArray = (ka*RefIndA*BesselJArraykAa*BesRicJArrayka -
        ka*RefIndVac*BesselJArrayka*
          BesRicJArraykAa)/((ka*RefIndA*BesselJArraykAa*BesRicHArrayka -
            ka*RefIndVac*BesselHArrayka*
              BesRicJArraykAa)*(BesRicJArrayka^2));
(*RhsNArray = (Refl1NNumA/Refl1NDenA)/(BesRicJArrayka*BesRicHArrayka);*)

RevRhsMArray = (Refl1MNumB/Refl1MDenB)/(BesselJArraykb*BesselHArraykb);
RevRhsNArray = (Refl1NNumB/Refl1NDenB)/(BesRicJArraykb*BesRicHArraykb);


(*Print["Loop over m begins"];*)

(*Loop over m begins here. For each m, there are m, m + 1, ...,
  Nmax values of l for solutions*)
(*For[m = 0, m < Nmax + 1,*)
For[m = 0, m < Max[5,Nmax + 1],
  (*Calculation of recursion coefficients for translation theorems,
```

```
  for each value of m*)
v = Table[n, {n, m, 2*Nmax}];
anmp = Table[0, {2*Nmax + 3}];
anmp[[Table[
        p, {p, 2 + m,
          2*Nmax + 2}]]] = -Sqrt[(v + m +
            1)*(v - m + 1)/((2*v + 1)*(2*v + 3))];
anmm = Table[0, {2*Nmax + 3}];
anmm[[Table[p, {p, 2 + m, 2*Nmax + 2}]]] =
  Sqrt[(v + m)*(v - m)/((2*v + 1)*(2*v - 1))];
bnmp = Table[0, {2*Nmax + 3}];
bnmp[[Table[p, {p, 2 + m, 2*Nmax + 2}]]] =
  Sqrt[(v + m + 2)*(v + m + 1)/((2*v + 1)*(2*v + 3))];
bnmm = Table[0, {2*Nmax + 3}];
bnmm[[Table[p, {p, 2 + m, 2*Nmax + 2}]]] =
  Sqrt[(v - m)*(v - m - 1)/((2*v + 1)*(2*v - 1))];

(*Calculation of translation matrix for scalar spherical waves.
      The following blue section determines the scalar translation \
\
coefficients for a given value of m and all allowable values of n and nu,
  upto n = nu = Nmax. The If statement is for starting values.*)
q = Table[p, {p, 2 + m, 2*Nmax + 2}] - 2;
If[m == 0,
  Tmatrix[[2 + m, q + 2]] = (-1)^q*Sqrt[2*q + 1]*BesselHArraykd[[q + 1]]
  (*Tmatrix[[2 + m, q + 2]] = (-1)^q*Sqrt[2*q + 1]*
        BesselJArraykd[[q + 1]]*)
  ];

For[n = m, n < 2*Nmax + 1,
```

```
      Tmatrix[[2 + n + 1,
            Table[p, {p, 2 + m,
                2*Nmax +
                  2}]]] = (anmm[[Table[p + 1, {p, 2 + m, 2*Nmax + 2}]]]*
                Tmatrix[[n + 2, Table[p + 1, {p, 2 + m, 2*Nmax + 2}]]] +
              anmp[[Table[p - 1, {p, 2 + m, 2*Nmax + 2}]]]*
                Tmatrix[[n + 2, Table[p - 1, {p, 2 + m, 2*Nmax + 2}]]] -

              anmm[[n + 2]]*
                Tmatrix[[n - 1 + 2, Table[p, {p, 2 + m, 2*Nmax + 2}]]])/
            anmp[[n + 2]];
      n++;
      ];

    (*Tempmatrix takes over the role of Tmatrix since Tmatrix has to be used \
\
for evaluating the coefficients for future values of m.
          The Tmatrix statement 5 lines below is evaluating the translation \
\
coeffs starting values for the next value of m.*)
    TempMatrix = Table[0, {2*Nmax + 3}, {2*Nmax + 3}];
    TempMatrix = Tmatrix;
    Tmatrix = Table[0, {2*Nmax + 3}, {2*Nmax + 3}];
    Tmatrix[[2 + m + 1,
          q + 2]] = (bnmm[[q + 2 + 1]]*TempMatrix[[2 + m, q + 2 + 1]] +
            bnmp[[q + 2 - 1]]*TempMatrix[[2 + m, q + 2 - 1]])/bnmp[[m + 2]];

    (*" scalar addition done for m"; *)(*Timing bracket*)
    (*Print[" scalar addition done for m"];*)
```

```
(*Start point for coefficient matrices - for each m,
  l starts at the greater of m and 1.*)
startpoint = m;
If [m == 0, startpoint = 1];

(*Defining translation matrices. First matrix sizes. TransCoeffs -
    scalar trans matrix for + ve kd. MTransCoeffs - scalar for -
    ve kd. VecTransAMat - Vector M to M + ve kd. VecTransBMat -
    Vector M to N + ve kd. *)
TransCoeffs = ZeroMatrix[Nmax - startpoint + 1];
MTransCoeffs = ZeroMatrix[Nmax - startpoint + 1];

VecTransAMat = ZeroMatrix[Nmax - startpoint + 1];
VecTransBMat = ZeroMatrix[Nmax - startpoint + 1];
MVecTransAMat = ZeroMatrix[Nmax - startpoint + 1];
MVecTransBMat = ZeroMatrix[Nmax - startpoint + 1];

(*TransCoeffs gives the alpha matrix of Chew -
    scalar translation coefficients*)
TransCoeffs =
  SubMatrix[
    TempMatrix, {startpoint + 2, startpoint + 2}, {Nmax - startpoint + 1, \

      Nmax - startpoint + 1}];

(*VecTransAMat - Vector M to M + ve kd. VecTransBMat - Vector M to N +
    ve kd.*)
nutable = Table[nu, {nu, startpoint, Nmax}];
For[n = 1, n < Nmax - startpoint + 2,
  VecTransBMat[[n, nutable - startpoint + 1]]  =
```

```
        TransCoeffs[[n, nutable - startpoint + 1]]/
          Sqrt[(n - 1 + startpoint)*(n +
                  startpoint)*(nutable*(nutable + 1))];
      VecTransAMat[[n, nutable - startpoint + 1]] =
        Sqrt[(nutable + m +
                    1)*(nutable - m +
                      1)/((2*nutable + 3)*(2*nutable + 1))]/(nutable + 1)*
            TempMatrix[[startpoint + 2 + n - 1, 2 + nutable + 1]] +
          Sqrt[(nutable + m)*(nutable - m)/((2*nutable - 1)*(2*nutable + \
1))]/
              nutable*TempMatrix[[startpoint + 2 + n - 1, 2 + nutable - 1]];
      n++;
      ];

    VecTransBMat = I*kd*m*VecTransBMat;
    VecTransAMat = kd*VecTransAMat + TransCoeffs;

    For[n = 1, n < Nmax - startpoint + 2,
      VecTransAMat[[n, nutable - startpoint + 1]] =
        VecTransAMat[[n, nutable - startpoint + 1]]/
          Sqrt[(n - 1 +
                  startpoint)*(n + startpoint)/(nutable*(nutable + 1))];
      n++;
      ];

    TransCoeffs = Transpose[TransCoeffs];
    VecTransBMat = Transpose[VecTransBMat];
    VecTransAMat = Transpose[VecTransAMat];
    (*Print[" vector addition done for m"];*)
    (*Completed computing VecTransAMat and VecTransBMat*)
```

```
    (*Going from traditional translation matrices to those matrices which \
\
have eigenvalues less than 1. This is the true equivalent of the \
translation \
matrix for plane waves.
          This is achieved by appropriate multiplication of bessel's \
\
functions.*)
    (*Right below in blue are eight matrices that multiply appropriate \
\
translation matrices to reduce them to forms more useful for computation.*)

    BessMat11 =  ZeroMatrix[Nmax - startpoint + 1];
    BessMat12 =  ZeroMatrix[Nmax - startpoint + 1];
    BessMat21 =  ZeroMatrix[Nmax - startpoint + 1];
    BessMat22 =  ZeroMatrix[Nmax - startpoint + 1];
    MBessMat11 =  ZeroMatrix[Nmax - startpoint + 1];
    MBessMat12 =  ZeroMatrix[Nmax - startpoint + 1];
    MBessMat21 =  ZeroMatrix[Nmax - startpoint + 1];
    MBessMat22 =  ZeroMatrix[Nmax - startpoint + 1];

    (*To compute translation matrices for the negative direction*)
    DomainArrayN = Table[n, {nu, startpoint, Nmax}, {n, startpoint, Nmax}];
    DomainArrayNu = Table[nu, {nu, startpoint, Nmax}, {n, startpoint, Nmax}];

    MTransCoeffs = TransCoeffs*(-1)^(DomainArrayN + DomainArrayNu);
    MVecTransAMat = VecTransAMat*(-1)^(DomainArrayN + DomainArrayNu);
    MVecTransBMat = -VecTransBMat*(-1)^(DomainArrayN + DomainArrayNu);
```

```
BessMat11 =
  DiagonalMatrix[
      Table[1.0/BesselHArraykb[[r]], {r, startpoint + 1,
          Nmax + 1}]].VecTransAMat.DiagonalMatrix[
      Table[BesselJArrayka[[r]], {r, startpoint + 1, Nmax + 1}]];
BessMat12 =
  DiagonalMatrix[
      Table[1.0/BesselHArraykb[[r]], {r, startpoint + 1,
          Nmax + 1}]].VecTransBMat.DiagonalMatrix[
      Table[BesRicJArrayka[[r]], {r, startpoint + 1, Nmax + 1}]];
BessMat21 =
  DiagonalMatrix[
      Table[1.0/BesRicHArraykb[[r]], {r, startpoint + 1,
          Nmax + 1}]].VecTransBMat.DiagonalMatrix[
      Table[BesselJArrayka[[r]], {r, startpoint + 1, Nmax + 1}]];
BessMat22 =
  DiagonalMatrix[
      Table[1.0/BesRicHArraykb[[r]], {r, startpoint + 1,
          Nmax + 1}]].VecTransAMat.DiagonalMatrix[
      Table[BesRicJArrayka[[r]], {r, startpoint + 1, Nmax + 1}]];


MBessMat11 =
  DiagonalMatrix[
      Table[1.0/BesselHArrayka[[r]], {r, startpoint + 1,
          Nmax + 1}]].MVecTransAMat.DiagonalMatrix[
      Table[BesselJArraykb[[r]], {r, startpoint + 1, Nmax + 1}]];
MBessMat12 =
  DiagonalMatrix[
      Table[1.0/BesselHArrayka[[r]], {r, startpoint + 1,
          Nmax + 1}]].MVecTransBMat.DiagonalMatrix[
```

```
        Table[BesRicJArraykb[[r]], {r, startpoint + 1, Nmax + 1}]];
    MBessMat21 =
      DiagonalMatrix[
        Table[1.0/BesRicHArrayka[[r]], {r, startpoint + 1,
            Nmax + 1}]].MVecTransBMat.DiagonalMatrix[
        Table[BesselJArraykb[[r]], {r, startpoint + 1, Nmax + 1}]];
    MBessMat22 =
      DiagonalMatrix[
        Table[1.0/BesRicHArrayka[[r]], {r, startpoint + 1,
            Nmax + 1}]].MVecTransAMat.DiagonalMatrix[
        Table[BesRicJArraykb[[r]], {r, startpoint + 1, Nmax + 1}]];



    (*Using the eight matrices to convert translation matrices obtained into \
\
final form such that eigenvalues are less than 1 in absolute value.*)
    VecTransMatPlus =
      BlockMatrix[{{BessMat11, BessMat12}, {BessMat21, BessMat22}}];
    VecTransMatMinus =
      BlockMatrix[{{MBessMat11, MBessMat12}, {MBessMat21, MBessMat22}}];

    ReflMArrayA = Table[0, {r, 1, Nmax - startpoint + 1}];
    ReflNArrayA = Table[0, {r, 1, Nmax - startpoint + 1}];
    ReflNArrayB = Table[0, {r, 1, Nmax - startpoint + 1}];
    ReflNArrayB = Table[0, {r, 1, Nmax - startpoint + 1}];

    ReflMArrayA =
      Table[ReflMNumA[[r]]/ReflMDenA[[r]], {r, startpoint + 1, Nmax + 1}];
    ReflNArrayA =
```

```
    Table[ReflNNumA[[r]]/ReflNDenA[[r]], {r, startpoint + 1, Nmax + 1}];
  ReflMArrayB =
    Table[ReflMNumB[[r]]/ReflMDenB[[r]], {r, startpoint + 1, Nmax + 1}];
  ReflNArrayB =
    Table[ReflNNumB[[r]]/ReflNDenB[[r]], {r, startpoint + 1, Nmax + 1}];

  ReflMatA = ZeroMatrix[2*(Nmax - startpoint + 1)];
  ReflMatB = ZeroMatrix[2*(Nmax - startpoint + 1)];

  ReflMatA = DiagonalMatrix[Join[ReflMArrayA, ReflNArrayA]];
  ReflMatB = DiagonalMatrix[Join[ReflMArrayB, ReflNArrayB]];

  (*Print[" VecTransMat done"];*)

  (*temparray21[[Table[
              r + Nmax - startpoint + 1, {r, 1,
                Nmax - startpoint + 1}]]] =;*)

  f12 =
    LinearSolve[
      IdentityMatrix[
          2*(Nmax - startpoint +
                1)] - \
(ReflMatB.VecTransMatPlus).(ReflMatA.VecTransMatMinus)\
];

  f21 =
    LinearSolve[
      IdentityMatrix[
          2*(Nmax - startpoint +
```

```
                    1)] - \
(ReflMatA.VecTransMatPlus).(ReflMatB.VecTransMatMinus)\
];

    CoeffDMMat =
      ZeroMatrix[Nmax - startpoint + 1, 2*(Nmax - startpoint + 1)];
    CoeffDNMat =
      ZeroMatrix[Nmax - startpoint + 1, 2*(Nmax - startpoint + 1)];
    CoeffCMMat =
      ZeroMatrix[Nmax - startpoint + 1, 2*(Nmax - startpoint + 1)];
    CoeffCNMat =
      ZeroMatrix[Nmax - startpoint + 1, 2*(Nmax - startpoint + 1)];
    CoeffDMat = ZeroMatrix[2*(Nmax - startpoint + 1)];
    CoeffCMat = ZeroMatrix[2*(Nmax - startpoint + 1)];

    RhsMat = ZeroMatrix[2*(Nmax - startpoint + 1)];
    RevRhsMat = ZeroMatrix[2*(Nmax - startpoint + 1)];
    RhsMat =
      DiagonalMatrix[
        Join[Table[RhsMArray[[r]], {r, startpoint + 1, Nmax + 1}],
          Table[RhsNArray[[r]], {r, startpoint + 1, Nmax + 1}]]];
    RevRhsMat =
      DiagonalMatrix[
        Join[Table[RevRhsMArray[[r]], {r, startpoint + 1, Nmax + 1}],
          Table[RevRhsNArray[[r]], {r, startpoint + 1, Nmax + 1}]]];

    (*RhsMat = ReflMatA;*)
    CoeffDMat = f12[-(ReflMatB.VecTransMatPlus).RhsMat];
    CoeffCMat = f21[-(ReflMatA.VecTransMatMinus).RevRhsMat];
```

```
CoeffDMMat =
  SubMatrix[
    CoeffDMat, {1, 1}, {Nmax - startpoint + 1,
      2*(Nmax - startpoint + 1)}];
CoeffDNMat =
  SubMatrix[
    CoeffDMat, {(Nmax - startpoint + 1) + 1, 1}, {Nmax - startpoint + 1,
      2*(Nmax - startpoint + 1)}];
CoeffCMMat =
  SubMatrix[
    CoeffCMat, {1, 1}, {Nmax - startpoint + 1,
      2*(Nmax - startpoint + 1)}];
CoeffCNMat =
  SubMatrix[
    CoeffCMat, {(Nmax - startpoint + 1) + 1, 1}, {Nmax - startpoint + 1,
      2*(Nmax - startpoint + 1)}];

(*For[r = 1, r < Nmax - startpoint + 1,

      CoeffDMat[[All, r]] =
        CoeffDMat[[All, r]]/BesselJArrayka[[r + startpoint]];

      CoeffDMat[[All, r + Nmax - startpoint + 1]] =
        CoeffDMat[[All, r + Nmax - startpoint + 1]]/
          BesRicJArrayka[[r + startpoint]];
      r++;
      ];*)

DMM =
  SubMatrix[
```

```
    CoeffDMMat, {1, 1}, {Nmax - startpoint + 1, Nmax - startpoint + 1}];
DMN =
  SubMatrix[
    CoeffDNMat, {1, 1}, {Nmax - startpoint + 1, Nmax - startpoint + 1}];
DNM =
  SubMatrix[
    CoeffDMMat, {1, Nmax - startpoint + 1 + 1}, {Nmax - startpoint + 1,
      Nmax - startpoint + 1}];
DNN =
  SubMatrix[
    CoeffDNMat, {1, Nmax - startpoint + 1 + 1}, {Nmax - startpoint + 1,
      Nmax - startpoint + 1}];

CMM =
  SubMatrix[
    CoeffCMMat, {1, 1}, {Nmax - startpoint + 1, Nmax - startpoint + 1}];
CMN =
  SubMatrix[
    CoeffCNMat, {1, 1}, {Nmax - startpoint + 1, Nmax - startpoint + 1}];
CNM =
  SubMatrix[
    CoeffCMMat, {1, Nmax - startpoint + 1 + 1}, {Nmax - startpoint + 1,
      Nmax - startpoint + 1}];
CNN =
  SubMatrix[
    CoeffCNMat, {1, Nmax - startpoint + 1 + 1}, {Nmax - startpoint + 1,
      Nmax - startpoint + 1}];

(*CoeffCMMat =
    SubMatrix[
```

```
        CoeffCMat, {1, 1}, {Nmax - startpoint + 1,
          2*(Nmax - startpoint + 1)}];
      CoeffCNMat =
        SubMatrix[
          CoeffCMat, {(Nmax - startpoint + 1) + 1, 1}, {Nmax - startpoint + \
1,
           2*(Nmax - startpoint + 1)}];*)

    temparray1 = Table[0, {r, 1, 2*(Nmax - startpoint + 1)}];
    temparray2 = Table[0, {r, 1, 2*(Nmax - startpoint + 1)}];

    For [u = 1, u < 2*(Nmax - startpoint + 1) + 1,
      temparray1[[u]] =
        Total[Table[
            Im[1.0/ReflMNumB[[r]]]*(Abs[
                CoeffDMMat[[r - startpoint, u]]])^2, {r, startpoint + \
1,
              Nmax + 1}] -
          Table[Im[
              1.0/ReflNNumB[[r]]]*(Abs[
                CoeffDNMat[[r - startpoint, u]]])^2, {r, startpoint + \
1,
              Nmax + 1}]];
      u++;
      ];

    (*Solving for coefficients C and D*)
    temparray12 = Table[0, {r, 1, 2*(Nmax - startpoint + 1)}];
    temparray21 = Table[0, {r, 1, 2*(Nmax - startpoint + 1)}];
```

```
temparray12[[Table[r, {r, 1, Nmax - startpoint + 1}]]] = (-I/ka);
temparray12[[Table[
        r + Nmax - startpoint + 1, {r, 1, Nmax - startpoint + 1}]]] = (I/
      ka);


q = Table[r, {r, startpoint, Nmax}];
PowerMatrix12[[m + 1, q]] =
  Im[1.0/ReflMNumA[[q + 1]]]*temparray1[[q - startpoint + 1]] -
    Im[1.0/ReflNNumA[[q + 1]]]*
      temparray1[[q - startpoint + 1 + (Nmax - startpoint + 1)]];

PowerMatrix12 [[m + 1, q]] = (1.0/(ka*kb))*(2.0/Pi)*
    PowerMatrix12[[m + 1, q]];

If[m > 0,
  PowerMatrix12[[m + 1, q]] = 2*PowerMatrix12[[m + 1, q]];
  (*PowerMatrix21[[m + 1, q]] = 2*PowerMatrix21[[m + 1, q]];*)
  ];

For [l = startpoint, l < Nmax + 1,
  If[PowerMatrix12[[m + 1, l]] < 0, PowerIndicator = 0];
  If[PowerMatrix21[[m + 1, l]] < 0, PowerIndicator = 0];
  l++;
  ];

(*Print[m];*)
```

```
  (*PutAppend[
  SequenceForm[m, " ",
    FortranForm[Total[PowerMatrix12[[m+1,All]]]]],
  StringJoin["Nmax", ToString[Ceiling[Nmax-3*(1 + Abs[kd])/2.0]], "kd",
     ToString[Ceiling[(d-a-b)*10^(10)]], "Aka",
    ToString[Ceiling[a*10^9]], "nmkb", ToString[Ceiling[b*10^9]],
    "nmNmaxAnalmfile.txt"]];*)

  If[Total[PowerMatrix12[[m+1,All]]] < 5.0*10^(-3)*Total[PowerMatrix12[[1,All]]

  (*For [l=1,l<Nmax+1,
   PutAppend[SequenceForm[l, " ", FortranForm[PowerMatrix12[[m+1,l]]*(kBoltz*E
  StringJoin["Nmax", ToString[Ceiling[Nmax-3*(1 + Abs[kd])/2.0]], "kd",
     ToString[Ceiling[(d-a-b)*10^(10)]], "Aka",
    ToString[Ceiling[a*10^9]], "nmkb", ToString[Ceiling[b*10^9]], "nmNmaxAnall
  l++;
  ];  *)

  m++;
  ];

SpecConductance12[[s]] = (ka/kta)^2*Exp[-ka/kta]/(1 - Exp[-ka/kta])^2*
    Total[Total[PowerMatrix12]];
SpecConductance21[[s]] = (ka/kta)^2*Exp[-ka/kta]/(1 - Exp[-ka/kta])^2*
    Total[Total[PowerMatrix21]];

Print["Frequency ", s, " done"];
PutAppend[
  SequenceForm[FreqEv, " ",
    FortranForm[SpecConductance12[[s]]*(kBoltz*ElecCharge/PlanckBy2Pi)]],
```

```
    StringJoin["Nmax", ToString[Ceiling[Nmax-3*(1 + Abs[kd])/2.0]], "kd",
       ToString[Ceiling[(d-a-b)*10^(10)]], "Aka",
      ToString[Ceiling[a*10^9]], "nmkb", ToString[Ceiling[b*10^9]],
      "nm.txt"]];
  Print[FortranForm[SpecConductance12[[s]]*(kBoltz*ElecCharge/PlanckBy2Pi)]];
  s++;
  ]
SpecConductance12 = SpecConductance12*(kBoltz*ElecCharge/PlanckBy2Pi);
SpecConductance21 = SpecConductance21*(kBoltz*ElecCharge/PlanckBy2Pi);

(*TotalConductance12 = (wmax - wmin)/(Nfreq - 1)*(Total[SpecConductance12] -
0.5*(SpecConductance12[[1]] + SpecConductance12[[Nfreq]]));*)

TotalConductance12 = Total[(Table[SpecConductance12[[r]],{r,1,Nfreq-1}]+
        Table[SpecConductance12[[r]],{r,2,Nfreq}])/2*freqinterval];

TotalConductance21 = (wmax - wmin)/(Nfreq - 1)*(Total[SpecConductance21] -
         0.5*(SpecConductance21[[1]] + SpecConductance21[[Nfreq]]));


Print[PowerIndicator];
PutAppend[
    SequenceForm["d = ", d*10^6, "; a = ", a*10^6, "; b = ", b*10^6,
      " ; Nmax = ", Ceiling[Nmax-3*(1 + Abs[kd])/2.0], " ; Power = ", \
FortranForm[TotalConductance12]], "specconductance.txt"];

Exit[]
```

Bibliography

[1] A. M. Ampère. *Mathématique Des Phénomenes Électro-Dynamiques, Uniquement Déduite de Lexpérience.* A. Blanchard, Paris, 1958.

[2] W. D. Niven, editor. *The Scientific Papers of James Clerk Maxwell*, volume 1. Dover Publications, New York, 1952.

[3] G. Kirchhoff. On the motion of electricity in wires. *Philos. Mag.*, 13:393–412, 1857.

[4] von W. Weber and R. Kohlrausch. Ueber die elektricitätsmenge, welche bei galvanischen strömen durch den querschnitt der kette fliesst. *Ann. Phys.*, 99:10–25, 1956.

[5] K. S. Mendelson. The story of *c*. *Am. J. Phys.*, 74:995–997, 2006 (and references in this work).

[6] R. C. Dougal. The centenary of the fourth-power law. *Phys. Educ.*, 14:234–238, 1979.

[7] M. Planck. *The Theory of Heat Radiation.* Dover Publications, New York, 1991.

[8] H. B. Callen and T. A. Welton. Irreversibility and generalized noise. *Phys. Rev.*, 83:34–40, 1951.

[9] S. M. Rytov. *Theory of Electric Fluctuations and Thermal Radiation.* Air Force Cambridge Research Center, Bedford, MA, 1959.

[10] *On the Theory of Electromagnetic Wave Diffraction by an Aperture in an Infinite Plane Conducting Screen*, New York, N. Y., 1951. Academic Press.

[11] C. T. Tai. *Dyadic Green Functions in Electromagnetic Theory.* IEEE Press, Piscataway, NJ, 1993.

[12] C.T. Tai. Some essential formulas in dyadic analysis and their applications. *Radio Sci. (USA)*, 22:1283 –1288, 1987.

[13] A. D. Yaghjian. Electric dyadic green's functions in the source region. *Proc. IEEE*, 68:248–263, 1980.

[14] R. E. Collin. *Field Theory of Guided Waves.* IEEE Press, Piscataway, NJ, 1990.

[15] L. Tsang, J. A. Kong, and K. H. Ding. *Scattering of Electromagnetic Waves.* Wiley, 2000.

[16] E. G. Cravalho, C. L. Tien, and R. P. Caren. Effect of small spacings on radiative transfer between two dielectrics. *J. Heat Trans. - T. ASME*, 89:351–358, 1967.

[17] G.A. Domoto and C.L. Tien. Thick film analysis of radiative transfer between parallel metallic surfaces. *J. Heat Trans. - T. ASME*, 92:399–404, 1970.

[18] R.F. Boehm and C.L. Tien. Small spacing analysis of radiation transfer between parallel metallic surfaces. *J. Heat Trans. - T. ASME*, 92:405–411, 1970.

[19] G.A. Domoto, R.F. Boehm, and C.L. Tien. Experimental investigation of radiative transfer between metallic surfaces at cryogenic temperatures. *J. Heat Trans. - T. ASME*, 92:412–417, 1970.

[20] D. Polder and M. Van Hove. Theory of radiative heat transfer between closely spaced bodies. *Phys. Rev. B*, 4(10):3303–3314, Nov 1971.

[21] C.M. Hargreaves. Radiative transfer between closely spaced bodies. *Philips Research Reports and Supplement*, 5:1–80, 1973.

[22] J.-B. Xu, K. Lauger, R. Moller, K. Dransfeld, and I. H. Wilson. Heat transfer between two metallic surfaces at small distances. *J. Appl. Phys.*, 76:7209–7216, 1994.

[23] W. Müller-Hirsch, A. Kraft, M. T. Hirsch, J. Parisi, and A. Kittel. Heat transfer in ultrahigh vacuum scanning thermal microscopy. *J. Vac. Sci. Technol., A*, 17:1205–1210, 1999.

[24] A. Kittel, W. Muller-Hirsch, J. Parisi, S. Biehs, D. Reddig, and M. Holthaus. Near-field heat transfer in a scanning thermal microscope. *Phys. Rev. Lett.*, 95:224301, 2005.

[25] R. S. DiMatteo, P. Greiff, S. L. Finberg, K.A. Young-Waithe, H. K. H. Choy, M. M. Masaki, and C. G. Fonstad. *Appl. Phys. Lett.*, 79:1894–1896, 2001.

[26] R. Carminati and J.-J. Greffet. Near-field effects in spatial coherence of thermal sources. *Phys. Rev. Lett.*, 82:1660, 1999.

[27] A. V. Shchegrov, K. Joulain, R. Carminati, and J.-J. Greffet. *Phys. Rev. Lett.*, 85:1548, 2000.

[28] J.-P. Mulet, K. Joulain, R. Carminati, and J.-J. Greffet. Nanoscale radiative heat transfer between a small particle and a plane surface. *Appl. Phys. Lett.*, 78:2931–2933, 2001.

[29] J-P. Mulet, K. Joulain, R. Carminati, and J-J. Greffet. Enhanced radiative transfer at nanometric distances. *Microscale Thermophys. Eng.*, 6:209–222, 2002.

[30] C. Henkel, K. Joulain, R. Carminati, and J.-J. Greffet. *Opt. Commun.*, 186:57, 2000.

[31] F. Marquier, K. Joulain, J.P. Mulet, R. Carminati, and J.J. Greffet. Engineering infrared emission properties of silicon in the near field and the far field. *Opt. Commun.*, 237:379 – 388, 2004.

[32] G. Domingues, S. Volz, K. Joulain, and J.-J. Greffet. Heat transfer between two nanoparticles through near field interaction. *Phys. Rev. Lett.*, 94(8):085901, 2005.

[33] A. I. Volokitin and B. N. J. Persson. Radiative heat transfer between nanostructures. *Phys. Rev. B*, 63:205404, 2001.

[34] M. D. Whale. *A fluctuational electrodynamic analysis of microscale radiative transfer and the design of microscale thermophotovoltaic devices.* PhD thesis, MIT, 1997.

[35] J. L. Pan, H. K. H. Choy, and C. G. Fonstad. Very large radiative transfer over small distances from a black body for thermophotovoltaic applications. *IEEE Trans. Electron Devices*, 47:241–249, 2000.

[36] S. Basu, Y.-B. Chen, and Z. M. Zhang. Microscale radiation in thermophotovoltaic devices - a review. *Int. J. Energ. Res.*, 31:689–716, 2007.

[37] A. Narayanaswamy and G. Chen. Surface modes for near field thermophotovoltaics. *Appl. Phys. Lett.*, 82(20):3544–3546, 2003.

[38] G. Bimonte. A theory of electromagnetic fluctuations for metallic surfaces and van der waals interactions between metallic bodies. *Phys. Rev. Lett.*, 96:160401, 2006.

[39] A.A. Rukhadze and V.P. Silin. Linear electromagnetic phenomena in a plasma. *Usp. Fiz. Nauk*, 76:79 – 108, 1962.

[40] V.P. Silin. Contribution to the theory of electromagnetic fluctuations in a plasma. *Zhurnal Eksperimental'noi i Teoreticheskoi Fiziki*, 41:969 – 976, 1961.

[41] V. M. Agranovic and V. L. Ginzburg. *Crystal Optics with Spatial Dispersion and Excitons.* Wiley, London, 1984.

[42] J. Weber. Fluctuation dissipation theorem. *Phys. Rev.*, 101(6):1620–1626, 1956.

[43] J. D. Jackson. *Classical Electrodynamics.* John Wiley, New York, 1998.

[44] J. A. Kong. *Electromagnetic Wave Theory.* EMW, 2000.

[45] W. C. Chew. *Waves and Fields in Inhomogeneous Media.* IEEE Press, Piscataway, NJ, 1995.

[46] S. M. Rytov, Yu. A. Kravtsov, and V. I. Tatarski. *Principles of Statistical Radiophysics*, volume 3. Springer-Verlag, 1987.

[47] H. S. Carlslaw and J. C. Jaeger. *Conduction of Heat in Solids.* Oxford University Press, London, 1959.

[48] N. Ozisik. *Boundary Value Problems of Heat Conduction.* Dover Publications, New York, 2002.

[49] P. M. Morse and H. Feshbach. *Methods of Theoretical Physics*, volume 1. McGraw-Hill, New York, 1953.

[50] L. D. Landau and E. M. Lifshitz. *Statistical Physics.* Addison-Wesley, 1969.

[51] V.L. Ginzberg, A.A. Rukhadze, and V.P. Silin. The electrodynamics of crystals and the theory of excitons. *J. Phys. Chem. Solids*, 23:85 – 97, 1962.

[52] A.A. Rukhadze and V.P. Silin. Electrodynamics of media with spatial dispersion. *Usp. Fiz. Nauk*, 74:223 – 267, 1961.

[53] A. Narayanaswamy and G. Chen. Thermal emission control with one-dimensional metallodielectric photonic crystals. *Phys. Rev. B*, 70:125101, 2004.

[54] O. S. Heavens. *Optical Properties of Thin Solid Films.* Dover Publications, 1991.

[55] A. Narayanaswamy and G. Chen. *Annual Review of Heat Transfer*, volume 14, chapter Direct Computation of Thermal Emission from Nanostructures, pages 169–195. Begell House, 2005.

[56] S. Chandrasekhar. *Radiative Transfer.* Dover publications, New York, 1960.

[57] M. Modest. *Radiative Heat Transfer.* Academic press, 2003.

[58] R. Siegel and J. Howell. *Thermal Radiation Heat Transfer.* Taylor and Francis, 2001.

[59] R. P. Caren. Thermal radiation between closely spaced metal surfaces at low temperatures due to traveling and quasi-stationary components of the radiation field. *Int. J. Heat Mass Transfer*, 17:755–764, 1974.

[60] L. D. Landau, E. M. Lifshitz, and L. P. Pitaevskii. *Electrodynamics of Continuous Media.* Pergamon Press, 1984.

[61] D. W. Pohl, W. Denk, and M. Lanz. Optical stethoscopy: Image recording with resolution $\lambda/20$. *Appl. Phys. Lett.*, 44:651–653, 1984.

[62] U. Durig, D. W. Pohl, and F. Rohner. Near-field optical-scanning microscopy. *J. Appl. Phys.*, 59:3318–3327, 1986.

[63] M. Fleischmann, P. J. Hendra, and A. J. McQuillan. Raman spectra of pyridine adsorbed at a silver electrode. *Chem. Phys. Lett.*, 26:163–166, 1974.

[64] T. W. Ebbesen, H. J. Lezec, H. F. Ghaemi, T. Thio, and P. A. Wolff. Extraordinary optical transmission through sub-wavelength hole arrays. *Nature*, 391:667–669, 1998.

[65] D. L. Mills and E. Burnstein. Polaritons: The electromagnetic modes of media. *Rep. Prog. Phys.*, 37:817–926, 1974.

[66] P. Y. Yu and M. Cardona. *Fundamentals of Semiconductors.* Springer-Verlag, 1999.

[67] W. G. Spitzer, D. Kleinman, and J. Walsh. Infrared properties of hexagonal silicon carbide. *Phys. Rev.*, 113:127, 1959.

[68] M. I. Eremets, M. Gauthier, A. Polian, J. C. Chervin, J. M. Besson, G. A. Dubitskii, and Ye. Ye. Semenova. Optical properties of cubic boron nitride. *Phys. Rev. B*, 52:8854, 1995.

[69] R. Geick, C. H. Perry, and G. Rupprecht. Normal modes in hexagonal boron nitride. *Phys. Rev.*, 146:543, 1966.

[70] O. Madelung, editor. *Non-Tetrahedrally Bonded Binary Compounds II*, volume III/17g of *Landolt-Bornstein*, page 36. 1984.

[71] P. F. Baldasaro, J. E. Raynolds, G. W. Charache, D. M. DePoy, C. T. Ballinger, and J. M. Borrego. Thermodynamic analysis of thermophotovoltaic efficiency and power density tradeoffs. *J. Appl. Phys.*, 89:3319, 2001.

[72] M. Laroche, R. Carminati, and J.-J. Greffet. Near-field thermophotovoltaic energy conversion. *Journal of Applied Physics*, 100:063704, 2006.

[73] C. J. Fu and Z. M. Zhang. Nanoscale radiation heat transfer for silicon at different doping levels. *Int. J. Heat Mass Trans.*, 49:1703–1718, 2006.

[74] C. Caloz, A. K. Skrivervik, and F. E. Gardiol. An efficient method to determine green's functions of a two-dimensional photonic crystal excited by a line source - the phased-array method. *IEEE Trans. Microwave Theory and Tech.*, 50:1380–1391, 2002.

[75] A. Narayanaswamy and G. Chen. Thermal radiation in 1d photonic crystals. *J. Quant. Spectrosc. Radiat. Transfer*, 93:175–183, 2005.

[76] A. Gombert. An overview of TPV emitter technologies. In T. J. Coutts, G. Guazzoni, and J. Luther, editors, *Thermophotovoltaic Generation of Electricity: Fifth Conference on Thermophotovoltaic Generation of Electricity*, volume 653, pages 123–131. AIP, 2003.

[77] A. Heinzel, V. Boerner, A. Gombert, B. Blasi, V. Wittwer, and J. Luther. Radiation filters and emitters for the NIR based on periodically structured metal surfaces. *J. Mod. Opt.*, 47:2399–2419, 2000.

[78] M. U. Pralle, N. Moelders, M. P. McNeal, I. Puscasu, A. C. Greenwald, J. T. Daly, E. A. Johnson, T. George, D. S. Choi, I. El-Kady, and R. Biswas. Photonic crystal enhanced narrow-band infrared emitters. *Appl. Phys. Lett.*, 81:4685–4687, 2002.

[79] S. Y. Lin, J. Moreno, and J. G. Fleming. Three-dimensional photonic-crystal emitter for thermal photovoltaic power generation. *Appl. Phys. Lett.*, 83:380–382, 2003.

[80] E. Palik. *Handbook of Optical Constants of Solids,*. Academic Press, 1985.

[81] M Gadenne, V Podolskiy, P Gadenne, P Sheng, and VM Shalaev. Plasmon-enhanced absorption by optical phonons in metal-dielectric composites. *Europhys. Lett.*, 53:364–370, 2001.

[82] S.-Y. Lin, J. G. Fleming, E. Chow, J. Bur, K. K. Choi, and A. Goldberg. Enhancement and suppression of thermal emission by a three-dimensional photonic crystal. *Phys. Rev. B*, 62:R2243–R2226, 2000.

[83] S. K. Lamoreaux. Demonstration of the casimir force in the 0.6 to $6\mu m$ range. *Phys. Rev. Lett.*, 78(1):5–8, Jan 1997.

[84] U. Mohideen and A. Roy. A precision measurement of the casimir force between 0.1 to $0.9\mu m$. *Phys. Rev. Lett.*, 81:4549–4552, 1998.

[85] A. Roy, C.Y. Lin, and U. Mohideen. Improved precision measurement of the casimir force. *Phys. Rev. D*, 60:111101–05, 1999.

[86] J.-P. Mulet, K. Joulain, R. Carminati, and J.-J. Greffet. Nanoscale radiative heat transfer between a small particle and a plane surface. *Appl. Phys. Lett.*, 78:2931–2933, 2001.

[87] H. Gies and K. Klingmuller. Casimir effect for curved geometries: Proximity-force-approximation validity limits. *Phys. Rev. Lett.*, 96:220401, 2006.

[88] J.H. Bruning and Y.T. Lo. Multiple scattering by spheres. Technical Report Antenna Laboratory Report No. 69-5, University of Illinois, Urbana, Illinois, 1969.

[89] J. H. Bruning and Y. T. Lo. Multiple scattering of EM waves by spheres, part. *IEEE Trans. Antennas Propag.*, AP-19:378–390, 1971.

[90] J. H. Bruning and Y. T. Lo. Multiple scattering of EM waves by spheres, part II - numerical and experimental results. *IEEE Trans. Antennas Propag.*, AP-19:391–400, 1971.

[91] B. Friedman and J. Russek. Addition theorems for spherical waves. *Q. of Appl. Math.*, 12:13–23, 1954.

[92] S. Stein. Addition theorems for spherical wave functions. *Q. of Appl. Math.*, 19(1):15 – 24, 1961.

[93] O.R. Cruzan. Translational addition theorems for spherical vector wave functions. *Q. of Appl. Math.*, 20(1):33 – 40, 1962.

[94] W. C. Chew. Recurrence relations for three-dimensional scalar addition theorem. *J. of Electromagnet. Wave*, 6:133–142, 1992.

[95] W. C. Chew. Efficient ways to compute the vector addition theorem. *J. of Electromagnet. Wave*, 7:651–665, 1993.

[96] K. Joulain, J.-P. Mulet, F. Marquier, R. Carminati, and J.-J. Greffet. Surface electromagnetic waves thermally excited: Radiative heat transfer, coherence properties and casimir forces revisited in the near field. *Surf. Sci. Rep.*, 57:59 – 112, 2005.

[97] W.C. Chew. Derivation of the vector addition theorem. *Microwave and Optical Technology Letters*, 3:256 – 260, 1990.

[98] K. T. Kim. *Symmetry Relations of the Translation Coefficients of the Spherical Scalar and Vector Multipole Fields*, volume 48 of *Progress In Electromagnetic Research*, chapter 3, pages 45–66. EMW Publishing, 2004.

[99] N. A. Gumerov and R. Duraiswami. Computation of scattering from n spheres using multipole reexpansion. *J. Acoust. Soc. Am.*, 112(6):2688 – 2701, 2002.

[100] C.M. Hargreaves. Anomalous radiative transfer between closely-spaced bodies. *Phys. Lett. A*, 30a:491 – 2, 1969.

[101] A. Kittel, W. Muller-Hirsch, J. Parisi, S. Biehs, D. Reddig, and M. Holthaus. Near-field heat transfer in a scanning thermal microscope. *Phys. Rev. Lett.*, 95(22):224301, 2005.

[102] B. V. Derjaguin, I. I. Abrikosova, and E. M. Lifshitz. Direct measurement of molecular attraction between solids separated by a narrow gap. *Quarterly Reviews*, 10:295–329, 1965.

[103] I. Larson, C. J. Drummond, D. Y. C. Chan, and F. Grieser. Direct force measurements between silica and alumina. *Langmuir*, 13:2109–2112, 1997.

[104] C. C. Williams and H. K. Wickramasinghe. Scanning thermal profiler. *Appl. Phys. Lett.*, 49:1587–1589, 1986.

[105] C. Dames. *Thermal Properties of Nanowires and Nanotubes: Modeling and Experiments.* PhD thesis, MIT, 2006.

[106] J. R. Barnes, R. J. Stephenson, C. N. Woodburn, S. J. O'Shea, M. E. Welland, T. Rayment, J. K. Gimzewski, and Ch. Gerber. A femtojoule calorimeter using micromechanical sensors. *Rev. Sci. Instrum.*, 65:3793–3798, 1994.

[107] J. Lai, T. Perazzo, Z. Shi, and A. Majumdar. Optimization and performance of high-resolution micro-optomechanical thermal sensors. *Sens. Actuators, A*, 58:113–119, 1997.

[108] J. Varesi, J. Lai, T. Perazzo, Z. Shi, and A. Majumdar. Photothermal measurements at picowatt resolution using uncooled micro-optomechanical sensors. *Appl. Phys. Lett.*, 71:306–308, 1997.

[109] P. G. Datskos, N. V. Lavrik, and S. Rajic. Performancs of uncooled microcantilever thermal detectors. *Rev. Sci. Instrum.*, 75:1134–1148, 2004.

[110] O. Nakabeppu, M. Chandrachood, Y. Wu, J. Lai, and A. Majumdar. Scanning thermal imaging microscope using composite cantilever probes. *Appl. Phys. Lett.*, 66:694–696, 1995.

[111] J. L. Hutter and J. Bechhoefer. Calibration of atomic-force microscope tips. *Rev. Sci. Instrum.*, 64:1868–1873, 1993.

[112] H J. Butt and M. Jaschke. Calculation of thermal noise in atomic force microscopy. *Nanotechnology*, 6:1–7, 1995.

[113] N A Burnham, X Chen, C S Hodges, G A Matei, E J Thoreson, C J Roberts, M C Davies, and S J B Tendler. Comparison of calibration methods for atomic-force microscopy cantilevers. *Nanotechnology*, 14:1–6, 2003.

[114] J. H. Lienhard IV and J. H. Lienhard V. *A Heat Transfer Textbook.* Phlogiston Press, Cambridge, Massachusetts, 2002.

[115] D. Song. *Phonon Heat Conduction in Nano and Micro-Porous Thin Films.* PhD thesis, University of California, Los Angeles, 2003.

[116] N. Sabate, T. J. Santander, I. Gracia, L. Fonseca, E. Figueras, E. Cabruja, and C. Cane. Characterization of thermal conductivity in thin film multilayered membranes. *Thin Solid Films*, 484:328–333, 2005.

[117] G. Langer, J. Hartmann, and M. Reichling. Thermal conductivity of thin metallic films measured by photothermal profile analysis. *Rev. Sci. Instrum.*, 68:1510–1513, 1996.

[118] J. N. Israelachvili and D. Tabor. The measurement of van der waals dispersion forces in the range 1.5 to 130 nm. *Proc. R. Soc. London, Ser. A*, 331:19–38, 1972.

[119] E. Merzbacher. *Quantum Mechanics.* Wiley, 1997.

[120] M. Abramowitz and I. Stegun. *Handbook of Mathematical Functions: With Formulas, Graphs, and Mathematical Tables.* Dover Publications, New York, 1965.